In-line monitoring of three-roll mill dispersion processes for functional carbon nanocomposites

Vom Promotionsausschuss der
Technischen Universität Hamburg

zur Erlangung des akademischen Grades

Doktor-Ingenieurin (Dr.-Ing.)

genehmigte Dissertation

von
Valea Kim Wisniewski
aus Hamburg

2024

Vorsitzender des Prüfungsausschusses:	Prof. Dr. habil. Michael Morlock (Technische Universität Hamburg)
Gutachter:	Prof. Dr.-Ing. habil. Bodo Fiedler (Technische Universität Hamburg) Prof. Clemens A. Dransfeld (Delft University of Technology)
Tag der mündlichen Prüfung:	09.01.2024

Technisch-Wissenschaftliche Schriftenreihe

Herausgeber:
Prof. Dr.-Ing. habil. Bodo Fiedler

Anschrift:
Technische Universität Hamburg
Institut für Kunststoffe und Verbundwerkstoffe
Denickestraße 15
21073 Hamburg

Band 45:
In-line monitoring of three-roll mill dispersion processes
for functional carbon nanocomposites
DOI: https://doi.org/10.15480/882.9148

Valea Kim Wisniewski
https://orcid.org/0000-0002-1546-0398

1. Auflage
Hamburg 2024

ISSN 2625-6029

Bibliographische Information der Deutschen Nationalbibliothek: Die deutsche Nationalbibliothek verzeichnet diese Publikation in der Deutschen Nationalbibliothek; detaillierte Informationen sind im Internet über dnb.de abrufbar.

Polymer Composites

TUHH

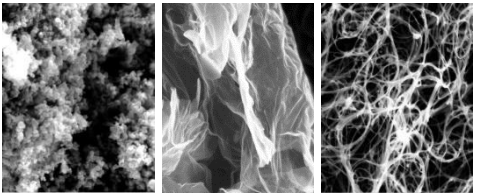

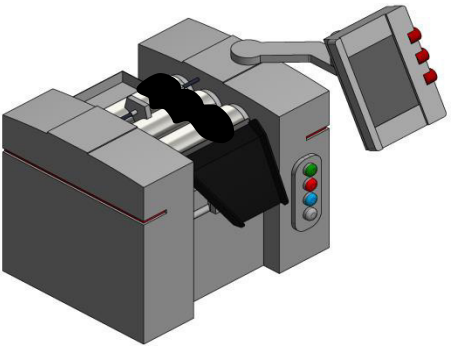

In-line Monitoring of Three-Roll Mill Dispersion Processes for Functional Carbon Nanocomposites

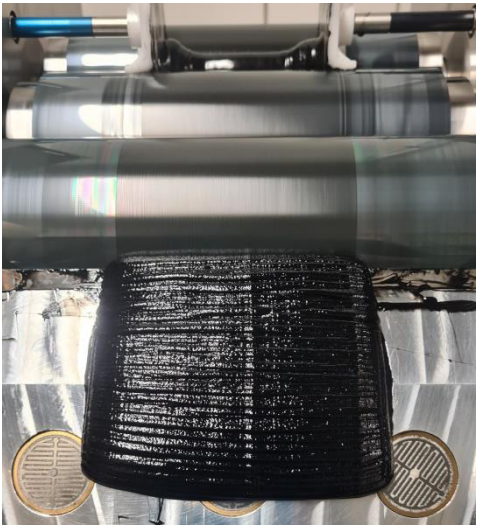

Valea Kim Wisniewski

2024

Kurzfassung

Verschiedene Forschungsfragen bezüglich des Herstellungsprozesses von Nano-Verbundwerkstoffen mit Kohlenstoffnanopartikeln und polymeren Harzen werden in dieser Dissertation beantwortet. Ausgangspunkt ist die in-line Überwachung des Dispersionsprozesses mittels Dreiwalzwerk von Harzsystemen gefüllt mit verschiedenen Füllgehalten und Partikelmorphologien. Die Linienkraft gibt dabei die rheo-mechanische Materialantwort durch ihren zeitlichen Verlauf während der Verarbeitung, sodass Prozessstabilität und Dispersionszustand beurteilt werden können. Der Einfluss von Harzviskosität, Partikelmorphologie, Temperatur und Maschinenparametern wird diskutiert, um ein umfassendes Verständnis des Dreiwalzwerkprozesses und der Optimierungspotentiale hinsichtlich Qualität, Durchlaufzeiten und Fördervolumen zu vermitteln.

In-line Impedanzmessungen wurden erstmalig auf dem Abnehmer des Dreiwalzwerkes integriert, um die Prozessqualität bewerten zu können. Die unterschiedlichen leitfähigen Kohlenstoff-Nanodispersionen können dadurch anhand ihrer Impedanzsignale unterschieden werden. Die Signalform resultiert dabei aus den Fließ- und Benetzungseigenschaften des verarbeiteten Materials auf der Elektrode und der Leitfähigkeit des Materials. Der neue Messaufbau wurde off-line und in-line mit variiertem Füllgehalt und Partikeltyp validiert.

Die Verarbeitung von Kohlenstoffnanopartikel-haltigen Zwischenprodukten eröffnete die Frage, ob eine permanentmagnetische Manipulation des Partikelnetzwerks möglich ist. Nur Kohlenstoffnanoröhrchen mit metallischem Katalysator-Restanteil haben als Agglomerate in niedrig-viskosen Medien eine Antwort auf schwache Magnetfelder gezeigt. Die Bewegung ist in Gradientenfeldern möglich, eine Ausrichtung in homogenen Feldern nur bedingt. Die Stabilität von Nano-Dispersionen über Zeit und gegen magnetische Manipulation wurde gezeigt. Außerdem wurden die Grenzen einer Übertragung in Epoxidharz-Verbunde diskutiert.

In der Produktionskette als letztes wird der Nano-Verbundwerkstoff betrachtet und die Anwendung als Temperatursensor erörtert. Dabei konnte mit einwandi-

gen Kohlenstoffnanoröhrchen modifiziertes Epoxidharz mit geringem Füllstoffgehalt als zyklisch belastbarer Sensor mit negativem Widerstands-Temperatur (NTC) Koeffizienten identifiziert werden. Die Einsatztemperatur umfasst dabei β- und Glas-Übergang der Matrix. Darüber hinaus wurden Elsatizitätsmodul und Widerstand für den Niedrigtemperaturbereich zwischen $-100\,^{\circ}\mathrm{C}$ und $170\,^{\circ}\mathrm{C}$ für unterschiedliche Typen von Kohlenstoffnanoröhrchen im Hinblick auf ihr Anwendungspotential diskutiert.

Abstract

The production process for carbon nanocomposites from the dispersion of particles and resin to particle network manipulation and final manufacturing of nanocomposites features interesting research topics addressed with this work. This thesis gives insight into in-line monitoring of three-roll mill dispersion processes of polymer resins filled with carbon nanoparticles of different morphology and various filler content. Line forces as a rheo-mechanical characteristic give insight into the process stability and state of dispersion by observing the line force development and separation phenomena. The influence of resin viscosity, particle morphology, processing temperature or machine settings is discussed to give a comprehensive understanding of the dispersion process and its optimization potential regarding product quality, processing time and production volume.

In-line impedance measurement can be integrated into a three-roll mill apron by choosing a flat interdigitated electrode to assess the quality of a process without interfering with the dispersion. Different conductive carbon resin dispersions can be distinguished based on their in-line signals in absolute impedance value and signal form. The signal form is resulting from flow and wetting behavior of the electrode and the overall conductivity of the dispersion. The integrated impedance measurement was validated in off-line and in-line measurements for a wide set of carbon filler morphology and filler content.

Working with carbon nano-intermediates yields the question of whether their particle network structure can be manipulated by permanent magnetic fields. From all tested particles only carbon nanotubes have a response to low permanent magnetic fields in their agglomerated state due to metal catalyst residuals incorporated within the tubes. Re-location of particles in magnetic gradient fields is possible in low-viscous media. Particle dispersion has been proven to be stable over time and resistant to permanent magnetic manipulation. This thesis gives insight into the limitations of a transfer to epoxy resin composites.

Finally, the application of carbon nanocomposites as temperature sensors is investigated. Low filler content SWCNT composites show reversible negative tem-

perature coefficients of resistance (NTC) temperature sensing behavior spanning both β- and glass transition temperature of the matrix. Data for low-temperature elastic modulus and resistivity between $-100\,^{\circ}\mathrm{C}$ and $170\,^{\circ}\mathrm{C}$ of three different CNT types are discussed with regard to their application potential.

Contents

List of Characters and Abbreviations

Greek Characters

Character	Unit	Description
γ	N/m	Interfacial tension
δ	rad	Phase shift
ε	F/m	Dielectric permittivity
η	−	Aspect ratio
κ	S/m	Electric surface conductivity
ρ	Ω m	Specific electric resistance
σ	S	Electrical conductivity
Φ	V m	Electric flux
ϕ	−	Volume fraction
φ	rad	Phase shift
χ	−	Magnetic susceptibility
ω	rad/s	Angular frequency

Indices

Index	Description
0	Initial Value
C	Coulomb
c	Critical
L	Lorentz
max	Maximum Value
mean	Mean Value
min	Minimum Value
t	Tunneling Current

Latin Characters

Character	Unit	Description
A	m^2	Area
AB	m	Working width
$\vec{B}$	T	Magnetic field
C	F	Electrical capacitance
d	m	Diameter or distance
E	N/m^2	Elastic modulus
$\vec{E}$	V/m	Electric field
E	J, eV	Energy
F	N	Force
G	N/m^2	Shear Modulus
G	S	Electric conductivity
$\vec{H}$	T	Auxiliary magnetic field
h	µm	Gap spacing
I	A	Current
L, l	m	Length
LF	N/mm	Line force
$\vec{M}$	A/m	Magnetization
m	kg	Mass
N	–	Number
n	rpm	Rotational speed
p	–	Percolation threshold
Q	C	Charge
R	Ω	Electrical resistance
r	m	Radius or distance
s	m	Tunneling distance
T	°C	Temperature
t	s	Time
U	V	Voltage
V	m^3	Volume
v	m/s	Velocity
W	J	Work within a potential
Y	S	Electric admittance
Z	Ω	Electric impedance

Abbreviations

Abbr.	Description
AC	Alternating Current
AHEW	Amine Hydrogen Equivalent Weight
BET	Brunauer–Emmett–Teller Method for Nitrogen Physisorption
CAD	Computer Aided Design
CB	Carbon Black
CFT	Charge Flow Transistor
CNP	Carbon Nanoparticle
CNT	Carbon Nanotube
CTE	Coefficient of Thermal Expansion
CVD	Chemical Vapour Deposition
DC	Direct Current
DGEBA	Diglycedyl-ether of Bisphenol A
DMTA	Dynamic Mechanical Temperature Analysis
DSC	Differential Scanning Calorimetry
DWCNT	Double-Wall Carbon Nanotube
EEW	Epoxy Equivalent Weight
FLG	Few-Layer Graphene
GNP	Graphene Nano-Platelet
IPC	Institute of Polymers and Composites
MOSFET	Metal Oxide Semiconductor Field-Effect Transistor
MWCNT	Multi-Wall Carbon Nanotube
NDT	Non-Descructive Testing
NTC	Negative Temperature Coefficient Thermistors
OCT	Optical Coherence Tomography
PTC	Positive Temperature Coefficient Thermistors
SEM	Scanning Electron Microscopy
SSA	Specific Surface Area
SWCNT	Single-Wall Carbon Nanotube
T75	Tuball 75 SWCNT
T99	Tuball 99 SWCNT
TEM	Tunneling Electron Microscopy
TRM	Three-Roll Mill
TUHH	Hamburg University of Technology
UP	Unsaturated Polyester Resin
UPT75	UP based Masterbatch with 1 wt% Tuball 75 SWCNT

1 Introduction

The three research fields presented within this dissertation are derived from a production line of functional carbon nanocomposites via three-roll milling (TRM). From neat resin and carbon nanoparticle characterization, dispersion technology and process monitoring to particle manipulation and application of the nanocomposite as a temperature sensor various topics are discussed.

1.1 Structure and Objective of this Thesis

The production of nano-carbon reinforced polymer resins is of great interest for coating applications or nano-enabled fiber reinforced composites. The process optimization requires in-depth understanding of the dispersion process. An in-line monitoring method helps by documenting the processing conditions and dispersion progress. Within this thesis, three main chapters answer open questions in the field of three-roll mill dispersion processes and nanocomposites. A graphical abstract of the topics of this thesis can be found in Figure 1.1.

As a theoretical base for this research, a brief overview of carbon nanoparticle (CNP) based dispersions and composites is given. A focus will be on understanding dispersion characterization with electric fields and the interaction of CNP and magnetic fields for network manipulation in Chapter 2. Further, temperature-dependent electrical and mechanical properties are reviewed in relevant fields. After giving the relevant scientific and technological background information, applied methods and materials of interest are presented in chapter 3. Sample preparation and characterization methods with used parameters are given.

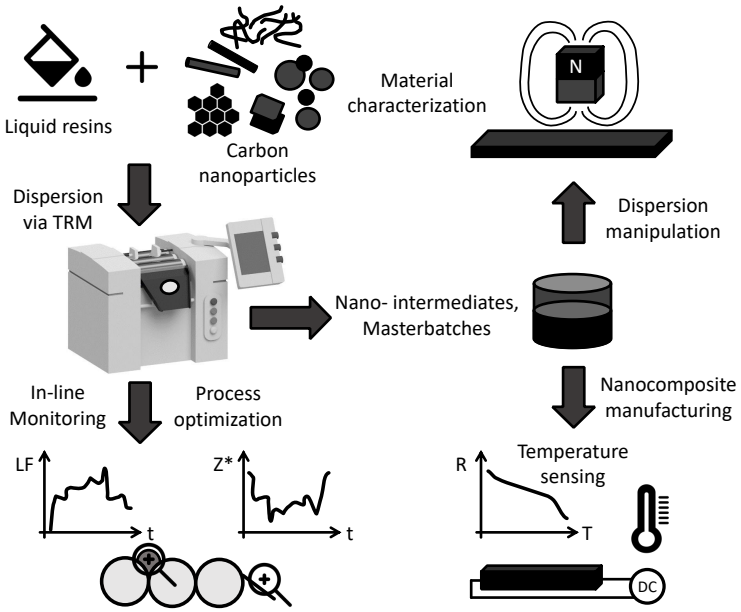

Figure 1.1: Graphical Abstract of the workflow and concept of this thesis

The in-line measurement of electric impedance is the aim of the first research topic to extend previously gained knowledge on off-line measurements [1, 2]. The previous off-line characterization techniques have been followed up on as a prework to this thesis and their potential or limitations will be summarized briefly in Chapter 3 to reasonably choose the method to implement in-line. A theoretical review on electrode design will give background on how the implementation of impedance measurement as an in-line method will differ from off-line measurements in cylinder electrodes. The prototypical integration of a measuring device into the three-roll mill and validation on a wide set of CNP resin dispersions will be given in Chapter 4. The influence factors on line force signals and impedance value over processing time are investigated.

Chapter 5 shifts the attention to the formed dispersions of fully incorporated carbon nanoparticle networks within polymer resins. For masterbatches and nano-intermediates temperature-dependent rheological behavior is described. The possibility to influence certain carbon nano-intermediates by permanent magnetic fields is discussed. Publications on magnetic manipulation of CNP disper-

sions are reviewed in Chapter 2.3.2 to understand previous approaches. Within this thesis, the observation of magnetic attraction of unmodified carbon nanotubes (CNT) in low-viscous media led to a set of experiments trying to create network-manipulated composites. Chapter 5 reflects on the limitations of this approach and discusses the influence of inhomogeneous and homogeneous fields on CNP dispersions.

Chapter 6 moves to a final application of fully cross-linked carbon nanoparticle reinforced epoxy composites as temperature sensors. Electrical resistance is presented for low temperatures down to $-100\,^{\circ}\mathrm{C}$ as well as their elastic mechanical response. This thesis expands the known behavior of carbon black and multi-wall carbon nanotube composites to the temperature-dependent electrical response of single-wall carbon nanotube composites. The objective is to find a suitable particle type and filler content to build reliable temperature sensors that can withstand a broad range of temperatures for cyclic thermal loading.

In the final Chapter 7 all conclusions are summarized to answer the research questions of each chapter and give an outlook on application fields for the results gained and the research areas that are worth investigating with the outcome of this thesis. Additional data supporting the results discussed within the respective chapters can be found in Appendices A, B and C.

2 Theoretical and Scientific Background

In the following chapter, all relevant scientific as well as technological background information is presented. From physics principles and material properties to production technology and application ideas a sufficient introduction to this thesis' research field is given.

2.1 Electric and Magnetic Fields

Fields interact with charged particles. Coulomb forces $\vec{F}_C$ act on stationary particles with charge Q in an electric field $\vec{E}$. Lorentz forces $\vec{F}_L$ act perpendicular to the trajectory of a moving particle with a certain velocity $\vec{v}$ in a magnetic field $\vec{B}$. [3] Since electric fields are used to characterize nanocomposites within this thesis and magnetic fields are used for manipulation, both fields are presented in the following sections.

2.1.1 Electric Fields

The Coulomb force $\vec{F}_C$ affecting a charge Q within an electric field $\vec{E}$ can be described by equation 2.1 [3–5].

$$\vec{F}_C = Q \cdot \vec{E} \tag{2.1}$$

The vectors of the field with parallel direction of the acting Coulomb forces form the electric field around a charge. [3] If a certain plane within this field is taken and the electric flux Φ has to be calculated, the direction with respect to the plane surface and field intensity based on all adherent charges determine the resulting flux to

$$\Phi = \int \vec{E} \cdot d\vec{A}. \tag{2.2}$$

Furthermore, the law of Gauss-Ostrogradski, short Gauss' law, is part of the Maxwell equations [3–5] and defines the electric flux through a closed surface around a charge Q as

$$\Phi = \frac{1}{\varepsilon_0} \cdot Q \tag{2.3}$$

with the vacuum permittivity $\varepsilon_0 = 8.854187812813 \cdot 10^{-12}\mathrm{F/m}$. [3–5] For a point charge and a surrounding spherical surface area with radius r, on which the field vectors stand perpendicular, the electric field derives from Equation 2.2 to

$$E = \frac{Q}{4\pi\varepsilon_0 r^2}. \tag{2.4}$$

Coulomb's law [3–5] for the force between two charges Q, Q' with distance r therefore can be deducted with consideration of Eq. 2.1 to

$$F_C = \frac{Q \cdot Q'}{4\pi\varepsilon_0 r^2} \tag{2.5}$$

For a plate capacitor consisting of two plates with surface area A with charges $+Q, -Q$ and a distance between plates of d the electric field is

$$E = \frac{Q}{\varepsilon_0 \cdot A} \quad .[3\text{–}5] \tag{2.6}$$

Since a capacitor in electric circuits is always charged by an applied voltage, the definition of an electric potential for an electric field has to be explained. For this the work for moving a charge Q within the electric field E from point $\vec{r}_1$ to point $\vec{r}_2$ can be considered and separated to define the voltage $U_{1,2}$ [3–5]:

$$W_{1,2} = -\int_{\vec{r}_1}^{\vec{r}_2} \vec{F} \cdot \mathrm{d}\vec{r} = -Q \int_{\vec{r}_1}^{\vec{r}_2} \vec{E} \cdot \mathrm{d}\vec{r} = Q \cdot U_{1,2} \tag{2.7}$$

With the voltage integral charge voltage and geometry of the plate capacitor can be connected [3–5]:

$$U_{cap} = -\int_0^d \vec{E} \cdot \mathrm{d}\vec{r} = E \cdot d = \frac{Q}{\varepsilon_0 \cdot A} \cdot d$$

A change of media between the plates from vacuum to a different dielectric changes the electric permittivity by a factor ε_r, the relative permittivity. [3–5] The capacitance C is defined as the capability to store electric charges

$$C = \frac{Q}{U} = \varepsilon_0 \cdot \varepsilon_r \cdot \frac{A}{d} \tag{2.8}$$

For multiple stacked media within a capacitor, the individual capacities 1 and 2 are added in parallel or serial circuits [3]:

$$C_{\text{parallel}} = C_1 + C_2 = \frac{1}{2} \cdot \varepsilon_0 \cdot (\varepsilon_{r,1} + \varepsilon_{r,2}) \cdot \frac{A}{d} \tag{2.9}$$

$$C_{\text{series}} = (\frac{1}{C_1} + \frac{1}{C_2})^{-1} = \frac{2 \cdot \varepsilon_{r,1} \cdot \varepsilon_{r,2}}{(\varepsilon_{r,1} + \varepsilon_{r,2})} \cdot \varepsilon_0 \cdot \frac{A}{d} \tag{2.10}$$

For particle-filled polymer resins or nanocomposites, the measurement of the capacitance thus can reveal changes in properties during chemical reactions, changes in particle agglomeration [1, 6] or structural damage [7–9]. In addition to a material's capacitive response to the applied electric field, the resistive behavior of a conductive pathway has to be considered.

To define an alternating current (AC) voltage the time-variant voltage $U(t)$ is written as

$$U(t) = U_0 \cdot \sin(\omega t) \tag{2.11}$$

with the amplitude U_0, angular frequency ω and time t [3, 5]. The resulting current is

$$I(t) = I_0 \cdot \sin(\omega t + \varphi) \tag{2.12}$$

with amplitude I_0, ω and t as for the applied voltage and φ is the phase difference between voltage and current. The phase angle φ is 0° for purely resistive systems and for purely capacitive behavior $\varphi = -90°$. [3, 5] The complex impedance of a system is

$$Z^* = \frac{U(t)}{I(t)} = \frac{U_0 \cdot \sin(\omega t)}{I_0 \cdot \sin(\omega t + \varphi)} = Z_0 \cdot \exp(i\varphi) = Z_0 \cdot (\cos(\varphi) + i \sin(\varphi)) = Z' + iZ'' \tag{2.13}$$

The complex impedance Z^* can thus be depicted as a complex number with real part Z' and imaginary part Z'' with phase angle φ. [10] The phase angle can be measured in addition to the absolute complex impedance Z^* [3, 5]:

$$|Z^*| = \sqrt{(Z'^2 + Z''^2)} \tag{2.14}$$

To monitor a dispersion production process, different electrode designs can be considered. The plate capacitor or cylinder electrode with parallel field lines between both electrodes is the simplest electrode geometry, mathematically described by equation 2.8. The set-up is suitable for lab measurements to characterize samples off-line (compare section 3.3.2). However, to integrate an electrode in a production line to measure within the material flow, flat electrode designs have to be considered. [10]

In the late 1970s Senturia et al. [11–14] reported on the development of a novel charge-flow transistor similar to conventional metal oxide semiconductor field-effect transistors (MOSFETs) consisting of flat metallic interdigitated electrode fingers. A depiction can be found in Figure 2.1.

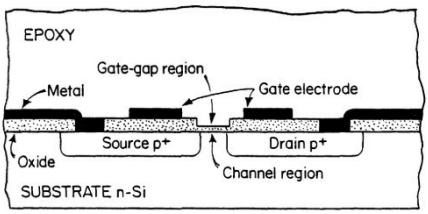

Figure 2.1: Charge-flow transistor, from Senturia [13, 14]

The MOSFET device was used as a humidity or gas detector by choosing a sensitive polymer to fill the gaps between the metal electrode fingers [11, 12]. The technology could further be applied to monitor the curing reaction of polymer resins by measuring the dielectric permittivity or dielectric loss factors [13, 14]. The electric admittance Y can be calculated by considering conductance G, measuring frequency ω and capacitance C [11–14]:

$$Y = G + i\omega C. \tag{2.15}$$

The conductance has to account for the total number of inter-electrode gaps N, W the length of electrode fingers, inter-electrode spacing L, oxide layer thickness t, respective conductivity σ of all sensor constituents and surface conductivity κ [11–14]:

$$G = \frac{4\sqrt{2} \cdot N \cdot W}{\pi^2} \cdot \left[\sigma_{\text{resin}} + \sigma_{\text{substrate}} + \frac{\pi t}{L} \cdot \sigma_{\text{ox}} + \frac{\pi}{L} \cdot (\kappa_{\text{ox}} + \kappa_{\text{substrate}})\right] \tag{2.16}$$

The capacitance is defined by respective dielectric permittivity ε

$$C = \frac{4\sqrt{2} \cdot N \cdot W}{\pi^2} \cdot \left[\varepsilon_{\text{resin}} + \varepsilon_{\text{substrate}} + \frac{\pi t}{L} \cdot \varepsilon_{\text{ox}}\right] \tag{2.17}$$

Sheppard, Senturia et al. [15] continued to develop this measuring technique to monitor resin curing processes. The mathematical description of the capacitance of flatter interdigitated electrodes can be found in [16–18]. Several further application cases can be found. Endres and Drost [19] optimized their electrode design for gas detection and suggested the smallest possible gap spacing between the electrode fingers to detect the changes in relative permittivity of the polymer. This follows from describing each inter-electrode space as a plate capacitor (compare equation 2.8), since the electrodes have a non-neglectable thickness. Interdigitated electrodes have been further used for moisture detection and double layer measurements in transformer insulations [20], vapor sensing [17] or

non-destructive material characterization [21]. A summary is given by Mamishev et al. [22]. A transfer to every material system with changing dielectric properties is possible.

The penetration depth of the electric field for measuring the material above the electrode is limited by the permittivity of the medium and the skin effect. Simulations and experimental measurements show about a third of the electrode distance for the penetration depth. [20, 21, 23, 24] The field penetration depth is crucial since relevant material volumes have to be included for monitoring a dispersion process, but external influences of the machine or workers around the production line have to be excluded. Multi-wavelength dielectrometry [20–24] combines several penetration depths into one sensor by spacing the interdigitated electrodes respectively as shown in Figure 2.2.

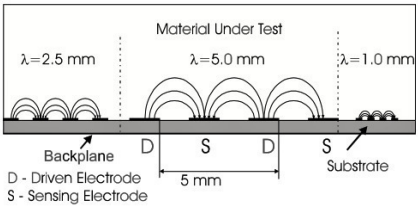

Figure 2.2: Multi-wavelength penetration depths, from Mamishev [21]

Electromagnetic shielding further influences the penetration depth of the electric field. Literature reports on the effectiveness of electromagnetic shielding of CNT composites. Influence factors, in addition to sample thickness and filler content, are the particle aspect ratio and metallic catalyst residuals. [25, 26]

In Chapter 4.2 the selection and design process of the integrated electrode will be presented. The penetration depth of the electric field is measured experimentally and shielding effects are considered in discussions of in-line monitoring signals in section 4.2.2.

2.1.2 Magnetic Fields

The Lorentz force $\vec{F}_L$ on a charge Q moving with velocity $\vec{v}$ within a magnetic field $\vec{B}$ is defined as their vector-product because the force acts perpendicular to the trajectory

$$\vec{F}_L = Q \cdot \vec{v} \times \vec{B} \tag{2.18}$$

The magnetic field has the unit Tesla $\mathrm{T} = \mathrm{Vs/m^2}$.

A current I within a conducting plate of thickness d running perpendicular to a magnetic field B is affected by the Lorentz force, so that a permanent charge can be detected perpendicular to the current's direction by the displaced charges. This effect is called Hall effect and can be used to detect magnetic fields by measuring the Hall voltage

$$U_H = -A_H \cdot \frac{I \cdot B}{d} = -\frac{1}{e \cdot n} \frac{I \cdot B}{d} \tag{2.19}$$

and includes the Hall factor A_H, which is the inverse of the product of elementary charge e and the number of conducting electrons n within the Hall sensor that have to compensate the Lorentz force by building the transversal electric field. Therefore, a high number of mobile electrons like in metals reduces the resulting Hall voltage. Thus, mostly semiconductors are used in Hall sensors for measuring magnetic fields. [3, 27]

The magnetic field within or outside a magnetic material differs by the material magnetization M. With the vacuum magnetic permeability $\mu_0 = 4\pi$ Vs/Am and the auxiliary magnetic field H the field inside a magnetic material is defined as

$$\vec{B} = \mu_0 \cdot (\vec{H} + \vec{M}) \tag{2.20}$$

whereas $\vec{B} = \mu_0 \cdot \vec{H}$ outside of the material. The volume magnetic susceptibility χ connects M and H as

$$\vec{M} = \chi \cdot \vec{H} \tag{2.21}$$

and thus defines the relative magnetic permeability of a material μ_r

$$\vec{B} = \mu_0 \cdot (1 + \chi) \cdot \vec{H} = \mu_0 \cdot \mu_r \cdot \vec{H}. \tag{2.22}$$

This proportionality is only valid for certain types of magnetic materials which leads to the differentiation of magnetic behavior [3, 5, 27]:

- Diamagnetism: In diamagnetic materials magnetic moments and magnetization are induced in the opposite direction when an external magnetic field is applied. They have no internal magnetic moments without an applied field. The susceptibility of diamagnetic materials is $\chi < 0$ and the permeability $\mu_r < 1$. Although most materials are diamagnetic, the behavior can be superimposed by other forms of magnetism which are stronger. To observe diamagnetic behavior, the atoms of a material have to have full orbitals and their spins combine to zero like Au, Cu, H_2 and N_2.

- Paramagnetism: In paramagnetic materials there are existing magnetic moments without an applied external magnetic field. This can be the result of unpaired spin or orbital moments of their electrons. The magnetic moments get orientated with the external field direction so that $\chi > 1$. The susceptibility is temperature T dependent according to Curie's law:

$$\chi = \frac{C}{T} = \mu_0 \cdot n \cdot \frac{\mu^2}{3 \cdot k_B \cdot T} \tag{2.23}$$

  C is the material specific Curie constant, n the number of atoms in the material and k_B Boltzmanns's constant. Examples are Pt, Al or O_2.

- Ferromagnetism: The strongest magnetic response of a material can be observed in metals with half-filled inner orbital shells, where parallel electron spins lead to strong intrinsic magnetic moments. Ferromagnetic materials have so-called Weiss domains, which are characterized by parallel oriented magnetization. Initially, the neighboring Weiss domains within a material can be randomly oriented. After applying an external magnetic field or quenching the material under a certain temperature, the Weiss domains orientate in the same direction. Magnetic moments are parallel afterward and a permanent magnetization remains in the material after taking the externally applied field away. Examples are Fe, Ni or Co. The magnetic order of a ferromagnet is destroyed above its Curie temperature T_C and the susceptibility follows with the Curie factor C to

$$\chi = \frac{C}{T - T_C} \tag{2.24}$$

  Antiferromagnets like MnO, FeO or NiO have Weiss domains in two dominating anti-parallel directions which cancel out the total magnetization after being fully oriented. Ferrimagnets have two anti-parallel domain types as well, but one direction is significantly stronger than the other resulting in a measurable total magnetization. Examples are $MeOFe_2O_3$ with different metals Me as Fe, Ni, Co or Cu.

The magnetic properties of certain carbon nano-particles are described in the subsequent section 2.2, the network manipulation of CNP within dispersions is reviewed in section 2.3.2.

2.2 Carbon-based Nanoparticles (CNP)

CNP are of broad interest due to their potential in modification of polymers for electric or thermal conductivity, mechanical performance or through-thickness

modification of fiber-reinforced composites [28, 29]. The morphology of carbon nanoparticles varies from globular or spheroidal carbon dots, fullerenes and carbon black to planar graphite and few-layer graphene to carbon nano-horns and rod-shaped multi- and single-walled carbon nanotubes. [30, 31] The particle aspect ratio is defined by their length L to diameter D ratio

$$\eta = \frac{L}{D}. \tag{2.25}$$

Globular particles have a low aspect ratio of around 1 because their diameter and length are almost identical. Rods and tubes have a low diameter compared to their length, which computes a high aspect ratio. The modification of insulating polymer matrices with conductive particles aims to form a percolated network, where the electrical conductivity of a nanocomposite changes from insulating to conductive. [28, 29, 32, 33] A simple description of this network can be given by a matrix 'lattice', wherein each cell can either be empty or occupied by a particle. The critical particle content p_c, when a conductive path spanning the whole matrix is formed is affected by the aspect ratio of the particles according to statistical percolation theory for rigid, rod-shaped particles [32, 33]:

$$p_c = \frac{1}{\eta}. \tag{2.26}$$

Electrical conductivity σ_c follows the percolation curve with low conductivity below the critical particle content p_c. The transition to higher conductivity with increased filler content is given by a constant factor c and a particle geometry exponent t [33].

$$\sigma_c = c(p - p_c)^t \tag{2.27}$$

Of course, the simple statistic distribution approach does not include dynamic percolation phenomena such as interactive forces and fluid motion. Furthermore, the geometric alterations of particles and contribution to the network have to be considered in more detail [33–37]. For example, Zare et al. [38] introduced a model for the electrical conductivity of CNT in polymers considering the interfacial tension of polymer and filler γ_{pf}, the percentage of CNT forming the network f, effective volume fraction ϕ_{eff}, the conductivity with respect to the waviness of the CNT σ_{fw}, the CNT diameter d and a tunneling parameter z

$$\sigma = \frac{0.1 \cdot \gamma_{pf} \cdot f \cdot \phi_{eff} \cdot \sigma_{fw}}{(d/z)^3} \tag{2.28}$$

Within this thesis, three different morphologies of CNP are investigated with regard to their processing in polymer resin, magnetic and thermo-electric properties:

Globular carbon black (CB) is produced mainly by incomplete combustion of carbon-containing matter or thermal decomposition of hydrocarbons and has its main application field in fillers for rubber products like tires [39, 40]. CBs are of globular shape with few micrometers in diameter with paracrystalline layered walls, which have low-order graphene crystallinity but are not strictly structured like fullerenes. Due to the missing higher order of crystallinity, layers and neighboring shells of carbon black particles exhibit larger spaces for intercalation and a higher specific surface area than common soot. Depending on synthesis and treatment graphitic areas can be increased leading to faces of parallel crystal orientation. Agglomerates can bundle differently depending on size distribution and surfaces. [40–42] The morphology and resulting properties are highly dependent on the synthesis process and post-treatment. The electric conductivity of carbon blacks is the superposition of graphitic conduction in continuous graphite layers, electron tunneling between layers and dielectric breakdown [43–45]. The magnetic properties are described by diamagnetic or paramagnetic behavior and are influenced by its crystallinity and oxygen attached to surface defects, since unpaired electrons and holes contribute primarily to magnetic spin [39, 40, 46].

Few-layer graphene (FLG) has van-der-Waals force stacked layers of hexagonal carbon lattices and is synthesized to exhibit large lateral surface areas. The perfect single-layer graphene was proven to exhibit extraordinary electric conductivity due to its delocalized π-electrons, high thermal conductivity as well as high tensile strength and elastic modulus while being a highly stretchable crystal. These extraordinary properties favor application in a variety of fields. [30, 47–54] In commercially available few-layer graphene for nanocomposite applications the crystal lattice is not perfect due to lattice defects or additional functional groups attached to edges. The electric conductivity thus depends on sheet orientation, since in-plane electron transport within the carbon lattice is nearly unhindered within the delocalized π-electron system and between layers the behavior is that of an insulator. Since lattices in FLG are distorted or connected the anisotropy of conductivity being limited to the graphitic plane can be diminished enabling electron transport between layers. [47, 48, 55–57] The magnetic properties of FLG vary by layer count, defects and attached functional groups or particles [58, 59] since they influence their electron structure. Strong magnetic responses can be observed on the nano-scale due to induced spin orientation or edge effects [60–65]. However, an FLG powder used for nanocomposite reinforcement has many overlapping effects canceling the magnetic moments out on a bulk-scale. [47, 48]

Carbon nanotubes (CNT) are rolled graphene sheets with closed ends. Single-wall carbon nanotubes (SWCNT) have only one layer whereas multi-wall carbon nanotubes (MWCNT) consist of several concentric tubes. The graphitic lattice determines the chirality of a CNT by giving the circumference vector of the rolled tube with respect to the unrolled hexagonal lattice. [66–75] Armchair and zig-zag tubes are rolled only in one of the lattice vector directions whereas all mixed directions are forming so-called chiral CNT. The chirality determines the size of the unit cell, Brillouin zone and electron transport along the tubes [67, 70–72, 75, 76]. Subsequently, metallic or semiconducting behavior of individual tubes can be distinguished. CNT with metallic character are defined by the difference of the chirality factors of the tube being integer multiples of three - $n_1 - n_2 = z \cdot 3$ with $z = 1, 2, 3, ...$, this is for example true for armchair tubes. Zig-zag tubes and all other chiral tubes are semiconducting [77–79]. Commercially available CNT powders include a variety of different tubes including defects and impurities depending on synthesis as well as post-treatment [69–72]. Besides reinforcing composites with CNT to improve electrical and thermal conductivity, mechanical enhancement is of great interest, too. High Young's and shear moduli as well as crack bridging and deflection effects make CNT suitable for mechanical reinforcements [69–73, 80–82]. The magnetic properties of CNT are depending on chirality [69, 73, 83, 84], defects or vacancies [64, 69, 82], catalyst residues [69, 82] or functionalization [80, 85–89]. Intrinsically, the magnetic response caused by spin-orbit interactions are weak and mostly diamagnetic [69, 84, 90] but calculations show different magnetic susceptibility along and perpendicular to the tube axis [84, 90, 91]. This property promises the ability to be aligned in strong magnetic fields. Edge effects can be achieved by vacancies or line defects within the carbon lattice [69, 92]. Induced magnetism by magnetic substrates can be observed [93–95] for individual tubes. The magnetic manipulation of CNT dispersions will be discussed in section 2.3.2.

2.3 Resin-based CNP Dispersions

Within this thesis, the different carbon nanoparticles are always considered within resin dispersions or cured nanocomposites, so the fundamentals of dispersion forces, processing technology and characterization methods have to be considered. Dispersions are solid particles mixed in a liquid phase and are also called colloid [96–101]. The interparticle forces of colloidal particles within a dispersion and intermolecular forces between particles and polymer matrix determine the stability of a dispersion. Due to the small scale of the carbon nanoparticles,

surface forces play an important role besides volume forces. The constituents and manufacturing process can influence the balance between attractive and repulsive forces of a dispersion. Attracting forces are Coulomb and van-der-Waals forces, interfacial forces or influences from chemical and physical absorption - all of them lead to clustering or agglomeration of particles. Repulsive forces include Born repulsion, hydration repulsion, entropic repulsion or electrostatic repulsion, these stabilize a dispersion. [96, 99, 102]

2.3.1 Dispersion Technologies

The dispersion technologies used to process carbon nano-intermediates are usually centrifugal mixing [103, 104], dissolvers [103], ultrasonic bath or tip sonication [103–107] and calendaring [103, 104, 108] or three-roll milling [2, 107, 109–113]. Comparisons and reviews of different processes can be found in literature [28, 102, 104, 114, 115]. Using high shear rates of an optimized three-roll mill process is the most efficient method to disperse medium- to high-viscous systems with high filler content [2, 104, 110, 112, 114]. Since this thesis is also the continuation of several open research questions from the Institute of Polymers and Composites, the publications [1, 2, 116, 117] have to be considered to choose initial process parameters and filler content.

Monitoring a dispersion process is crucial to tailor processing parameters to an optimum. Applying different off-line characterization methods has been proven to give valuable insight into dispersion processes. Electrical measurements and rheological characterization show the most valuable insight into the dispersion progress [1, 2, 116–123]. A summary of monitoring methods tested in pre-experiments for this thesis can be found in section 3.3.2 following.

2.3.2 CNP Network Manipulation with Magnetic Fields

The previously discussed dispersion state mostly aims to create a uniform particle network with separation down to nano-scale. This enables lowest filler contents to achieve electrical or thermal conductivity. However, the manipulation of such well dispersed state finds attention in literature to create anisotropy for a favored discharge direction or directional mechanical enhancement. The alignment or re-arrangement of CNP by AC electric fields has been explored in various studies [124–128] and is not going to be the focus of this literature review. Magnetic flocculation [129] or medical magnetic targeting [130] are research fields,

that are also not the direct interest of this thesis. Here, an overview on the magnetic manipulation of mostly CNT dispersions to form anisotropic nanocomposites is given. After calculating the magnetic properties of CNT based on their unique band structure in the 90s and early 2000s [64, 83, 84, 91], several studies emerged utilizing the magnetic properties in nanocomposites. They have to be distinguished in modified CNT manipulation, wherein CNT are functionalized with magnetic nanoparticles, and studies with as-synthesized CNT.

Leonhardt et al. [85] started with functionalized CNT by annealing MWCNT from a ferrocene-injection CVD process in 2005. 40 % magnetic α-Fe with mostly graphite remains after this procedure and results in highest possible magnetic moments per square millimeter. This approach maximized the magnetic response by compromising the CNT geometry and graphitic lattice completely. In 2011, Buluy et al. [131] used α-Fe filled MWCNT, retaining their morphology, in nematic liquid crystals pentyl-cyanobiphenyl (5CB) to demonstrate their response to weak magnetic fields (5 mT). The CNTs form elongated aggregates parallel to the liquid crystal director under applied magnetic fields due to magnetic and van-der-Waals interaction. Transitioning to the isotropic phase, the CNTs form smaller non-orientated aggregates again. Kim et al. [86] modified MWCNT with maghemite γ-Fe_2O_3 nanoparticles in a sol-gel process. An epoxy resin composite (PR2032 resin, PH3660 curing agent) was cured under applied 0.3 T magnetic field for 1 h at room temperature and 1 h at 60 °C. The alignment and network formation of modified MWCNT was shown by SEM micrographs as well as increased electrical conductivity in field direction. Ma et al. [88] presented a large-scale one-pot synthesis method for magnetic iron CNT, which are able to retract arsenic from water by magnetic separation in 2012. The CNT are the carrier for demanded iron oxides for removal while offering sufficient surface area as an adsorbant. In 2016 Ariu et al. [89] demonstrated the positioning of Ni-plated and COOH- functionalized MWCNT within a low viscosity epoxy resin (PRIME^{TM} 20LV by Gurit) by exposing it to a direct current (DC) magnetic field of 0.5 T for 200 min gel time. The agglomeration of MWCNT under the edges of a magnet could be observed due to the stronger magnetic flux there caused by the magnetic edge effect. Images and computer tomography scans of the samples prove localization of the MWCNT, however, claimed alignment can not be seen by supplied graphics. Yavari et al. [132] were able to align Fe_3O_4 modified CNTs parallel to the applied magnetic field forming aggregated chains in a ferrofluid in 2019. Trivedi et al. [133] aligned pristine and diazotization Ni-functionalized CNT in a static magnetic field, creating a particle network distributed on bulk-scale but locally aligned parallel to the field. The synergistic

effect of Co-based catalysts and alumina powder for chemical vapor deposition (CVD) synthesis of CNT was observed by Zoladz et al. [87] in 2020. In contrast to pure Al_2O_3 the incorporation of only 10 % CNT led to a significant increase of saturation magnetization by 2500 %.

Without additional functionalization, Yonemura et al. [134] used a superconducting magnet to horizontally align SWCNT in a MEHPPV composite and validated the alignment by AFM micrographs in 2008. 2009, Jang et al. [135] found polyethyleneimine to be a suitable medium to form stable (1 year) ultrasonicated dispersions of MWCNT. Moreover, well-separated CNT showed an orientation of their tube axis with applied strong magnetic field of 12 T due to their difference in magnetic susceptibility parallel and perpendicular to the tube axis. Shorter, straight tubes were aligned more than longer undulated tubes. Tsuda et al. [136] explored the alignment and micro-patterning of annealed MWCNTs in solvents, silicone and ceramic composites. Superconducting magnets were used to generate 5, 10 and 12 T fields and patterned 200 µm-thick aluminum and iron layers are used to locally modulate the magnetic flux and localize CNTs on that scale in stripes.

Lipert et al. [137] investigated the influence of residual catalysts within CNT on their magnetic properties in 2010. They found significant differences between type and amount of ferromagnetic and diamagnetic catalysts and proposed a characterization method for residual catalysts based on their findings. It was also found, that high-temperature annealing of CNTs with non-magnetic catalysts can reveal the diamagnetic behavior expected for pure carbon structures by literature [69, 83, 84, 90]. In the same year, Mahfuz et al. have shown [138] a significant increase in tensile strength and elastic modulus for CNT-modified SC-15 epoxy nanocomposites which were cured under an extremely strong electromagnetic field of 28 T.

A work from 2015 has a similar approach as the magnetic manipulation of this thesis presented in Chapter 5. Ma et al. [139] used the residual Ni catalysts of Chengdu Organic Chemicals Co. Ltd MWCNT with 90 % purity to manufacture fracture toughness enhanced epoxy (Araldite-F, Aradur-HY951) nanocomposites by stirring and ultrasonication mixing. Permanent magnetic alignment of the CNTs was achieved by curing under a 0.4 T field. SENB tests showed increased fracture toughness by 51 % for 3 wt% CNTs aligned perpendicular to the crack propagation direction by forcing plastic shear deformation of the matrix as a toughening mechanism.

2.4 Temperature-Dependent Behavior of Epoxy Resins and CNP Nanocomposites

For Chapter 6 of this thesis the thermo-mechanic and temperature-dependent electric properties of epoxy resins and CNP nanocomposites are relevant. Diglycedyl-ether of Bisphenol A (DGEBA) epoxy resins cross-linked by amine curing agents are investigated. Epoxy resins are defined by their functional epoxy groups (R-CH-O-CH_2), can have variable molecular weight and thus exhibit different cross-linking densities and resulting properties. Epoxy resins offer low shrinkage during curing, good chemical resistance and can be tailored to have suitable mechanical or electrical properties in adhesives or fiber reinforced composites. [140–142]

Around 1960 Kaelble [143], May and Weir [144] and Kline [145] presented the dynamic mechanical thermal analysis (DMTA) of important DGEBA epoxy resins. The complex elastic modulus E^* can be divided into a storage modulus E' of the elastic and reversible material response and the loss modulus E'', which characterizes the dissipating part when a material undergoes cyclic mechanical loading. E^* is defined as the ratio between applied time-dependent stress and resulting strain of a material.

$$E^* = E' + iE'' \tag{2.29}$$

where the loss factor $tan(\delta)$ is defined as

$$tan(\delta) = \frac{E''}{E'}. \tag{2.30}$$

An example graph from Kline [145] can be found in Figure 2.3 for Epon 828 epoxy resin cured with m-phenylenediamine. The elastic modulus decreases with increasing temperature, with several steps of stronger changes. The loss factor (here called 'internal friction') indicates these more significant changes in behavior by four peaks over the temperature range. The first peak is the so-called β-transition at low temperatures around $-33\,^\circ$C. Variations in post-curing of the epoxy revealed a dependence of this peak on treatment at elevated temperatures after initial curing at room temperature. With increasing post-curing time at $60\,^\circ$C the β-transition peak decreases to a minimum. This behavior is ascribed to the cross-linking density which increases during post-curing. The second smaller peak in loss factor is attributed to cure time as well a filler content of a non-reactive additive. Most prominent is the glass transition T_g around $175\,^\circ$C, where the polymer softens significantly. It is in congruence with observations in [143,

144, 146–148] and attributed to torsional or rotational motions of the molecules between cross-links. After the glass transition, the behavior is described as rubber-like before the degradation sets in. [145]

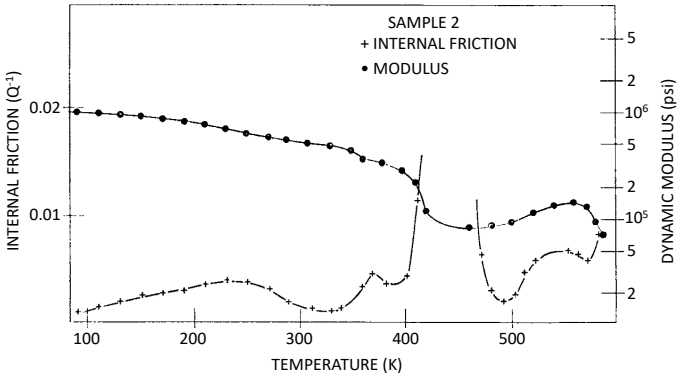

Figure 2.3: Elastic modulus and tan(δ) over temperature, from Kline [145]

May and Weir [144] report on cyclic loading over a large temperature range between $-70\,^{\circ}\mathrm{C}$ and $200\,^{\circ}\mathrm{C}$. Two major changes in the elastic modulus and respective peaks in the tan(δ) graph can be observed for the DGEBA epoxy cured with metaphenylene diamine [144]. In Figure 2.4 two influence factors are compared by analyzing the respective loss factors tan(δ) over temperature. On the left side, the influence of the substituents on the central carbon bridge can be seen as a shift for the so-called glass transition temperature T_g between 120–160 °C. The glass transition is correlated with the rotation around single bonds. The larger the attached group at the central carbon bridge, the more a rotation is hindered and thus needs more thermal energy to soften at elevated temperatures.

On the right in Figure 2.4 the molecular weight of the epoxy resin is altered. The comparison resin is crystalline with shorter chains, leading to a higher cross-linking density. The intensity of the lower transition temperature is higher, the glass transition temperature is shifted to higher temperatures. This correlation between molecular weight of the resin, cross-linking density and T_g is agreed upon in literature [146–149]. Further experiments with different curing agents aimed to alter the diglycidyl ether portion of the molecule because its structure attributes to the β-transition at low temperatures around $-60\,^{\circ}\mathrm{C}$.

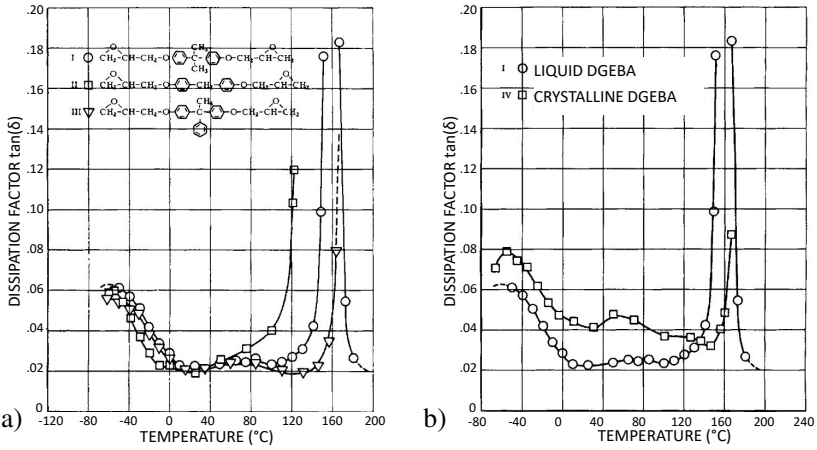

Figure 2.4: a) tan(δ) over temperature for different substituents on the central carbon bridge, b) tan(δ) over temperature for varied resin purity, from May and Weir [144]

Since the curing state of epoxy resins is important in understanding their thermomechanical properties, another characterization method and its advances shall be introduced: Differential scanning calorimetry (DSC) is a thermal analysis method that quantifies the heat capacity of a material against a reference. [150–152] Endothermic processes such as melting or phase transitions can be distinguished from exothermic signals like curing reactions or crystallization. [150] For amorphous epoxy resins, the glass transition is visible as an endothermic step. [150, 153, 154]

Hardis et al. [154] show the exothermic peak of the residual curing reactions that are possible, when an epoxy sample is not fully cross-linked. In Figure 2.5 the curing time is set to various times before measuring the DSC signal between $-50\,^{\circ}\mathrm{C}$ and $270\,^{\circ}\mathrm{C}$. It can be seen that after a sufficient curing time of 120 min the exothermic curing reaction is diminished and only the endothermic glass transition step appears in the signal. It can also be seen, that the glass transition temperature is shifted to higher temperatures with increasing curing state [150, 154, 155].

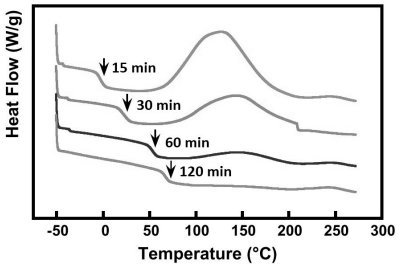

Figure 2.5: DSC curves for partially cured samples at 80 °C for various times, from Hardis et al. [154]

Since polymer network structure, cross-linking density and molecule orientation can all influence the polymer's mobility, all of these factors can impact the glass transition. Fava [155] and Kreiblich et al. [156] both reported on annealing effects on the DSC signal around glass transition. Annealing an epoxy resin at temperatures close to glass transition [156] or slowly cooling down crossing T_g [155] can introduce a higher degree of order in the glassy state. These short-range oriented molecule segments require more energy to move again by thermal excitation. Therefore, an endothermic peak can be observed close to T_g in annealed samples as shown in Figure 2.6 (axes in the publications are inverted). With increasing annealing time the endothermic peak is more pronounced.

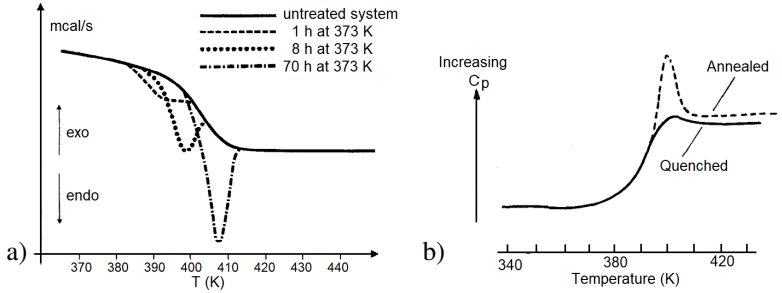

Figure 2.6: DSC curves for annealed epoxy in comparison to quenched or annealed state from a) Kreiblich et al. [156] and b) Fava [155]

The addition of CNP as solid filler particles to the epoxy resin increases the elastic modulus since the modulus of carbon nanostructures is higher than that of pure epoxy resin. [2, 106, 157] The influence of filler particles on glass transition

temperature T_g is reported to be indifferent in literature. Comparative studies of a wide range of particles and filler contents in [2] show low impact of CNP fillers except for expanded and functionalized graphene, which decreased T_g by up to 10 K according to DMTA measurements. Barrau et al. [157] observed a slight depression of T_g in DSC measurements for CNT filled epoxy resin. Observations account this decrease to be proportional to the excluded volume by the particles as well as the high aspect ratio of CNTs on nano-scale. At the percolation threshold, it is argued that the fully formed continuous particle network disrupts the polymer matrix maximally and thus gives highest mobility to separated polymer chains.

Lastly, the thermo-electric properties of CNP nanocomposites are reviewed in this chapter to understand temperature-dependent conductivity changes in particle reinforced polymers. This is interesting since conventional temperature sensors can be replaced by integrated sensors to create new types of functional composites. [158–160] The contributions to a CNP composite's electrical resistance with a non-conductive epoxy matrix are

- Electrical resistance of the matrix (minimally decreasing with increasing temperature)
- Interfacial resistance between matrix and CNP
- Intrinsic electrical resistance of CNP (dependent on metallic or semi-conducting behavior of the particles)
- Contact resistance of touching CNP (influenced by thermal vibration and thermal expansion of surrounding matrix)
- Tunnel resistance of CNP

The development of resistivity over temperature can show a positive temperature coefficient of resistance (PTC) [161–168] or negative temperature coefficients (NTC) [162, 169–180]. The temperature coefficient α of resistivity is therefore describing the resistance ρ over temperature T with initial specific resistance ρ_0 as:

$$\rho = \rho_0 \cdot (1 + \alpha \cdot (T - T_0)) \tag{2.31}$$

Insulators like most polymer matrices have high resistivity since their conductive energy band is not filled and the energy gap is large. Resistance only decreases slightly with increasing temperature, since the band gap is too large to be overcome by thermal activation. Semi-conductors show NTC behavior because the increased thermal energy increases the number of available charge carriers n in

the conductive energy band. The band gap with energy E_g is small enough to be overcome by thermal energy [3–5, 27]:

$$n \propto \exp(\frac{-E_g}{2 \cdot k \cdot T}) \tag{2.32}$$

Metals or metallic conductors have electrons in the conductive band above their energy gap and thus are conductive. With increasing temperature, the resistance increases linearly above a certain temperature. This is due to the collision of electrons and nuclei within the material which happens at higher rates with increasing temperature, this then decreases electron mobility which is the main charge transport mechanism in metals. [3–5, 27] For the conductivity of metals the following equation describes the conductivity:

$$\sigma_{\text{metal}} = \frac{n \cdot e^2 \tau}{2 \cdot m_e} \tag{2.33}$$

with n the number of electrons, e electron charge, τ collision time and the electron mass m_e.

Simmons described the tunnel current between two conductive electrodes separated by a thin insulating film in 1963 [181–183].

$$I = \frac{e^2}{s \cdot h^2} \cdot \sqrt{m \cdot (\varphi_1 + \varphi_2)} \cdot V \cdot \exp\left[\sqrt{-\frac{4\pi \cdot s}{h} \cdot \sqrt{m} \cdot \sqrt{(\varphi_1 + \varphi_2)}}\right] \tag{2.34}$$

with the electron charge e, Planck's constant h, the thickness of the insulating film s, applied voltage V and the barrier height φ_1, φ_2 at the two electrodes and the insulating film. This relation reduces to a linear dependence on V for low voltage between the electrodes. [181–183]

For thin metallic films made of small particles separated by insulating gaps the tunneling resistance ρ was described by Sheng et al. [184, 185] to depend on thermal fluctuations of the charges being able to jump the gaps. Carmona et al. [186] further described this behavior to be

$$\rho = \rho_1 \cdot \exp(\frac{T_2}{T^\alpha}) \tag{2.35}$$

with material constants ρ_1, T_2 and the exponent α, which is reported to be dependent on the particle distance [184–186].

Zhang et al. [187] refined Simmons equations to their fluctuation-induced tunneling (FIT) model for the tunnel resistance between two particles:

$$R_t = \frac{V}{d^2 J} = \frac{8\pi \cdot h \cdot s}{3 \cdot d^2 \cdot \gamma \cdot e^2} \cdot \exp(s \cdot \frac{4\pi}{h} \cdot \sqrt{2 \cdot m \cdot \phi}) \tag{2.36}$$

Ruschau et al. [188] described the resistance of a particle network consisting of M particles based on number of conducting pathways N including tunnel junctions with resistance R_t and particle resistance R_p:

$$R = \frac{(M-1)\cdot R_t + M \cdot R_p}{N} \approx \frac{M \cdot (R_t + R_p)}{N} \tag{2.37}$$

For most systems, this model is simplified by a tunnel resistance much larger than the particle resistance, so that the total resistance can be attributed to the aforementioned tunnel resistance

$$R = \frac{M}{N} \cdot \left[\frac{8\pi \cdot h \cdot s}{3 \cdot d^2 \cdot \gamma \cdot e^2} \exp(s \cdot \frac{4\pi}{h}\sqrt{2m\phi})\right] \tag{2.38}$$

The FIT-model based on tunnel resistance and thermally activated charge transfer at tunnel junctions was discussed frequently in literature [170, 174, 184–186, 189] and applied to material systems at the Institute of Polymers and Composites [172, 190]:

$$\sigma = \sigma_0 \cdot \exp\left[\frac{-T_1}{T+T_0}\right] = \sigma_0 \cdot \exp\left[\frac{-\frac{sA{\varepsilon_0}^2}{8\pi k}}{T + \frac{2\frac{sA{\varepsilon_0}^2}{8\pi k}}{s\pi\sqrt{2m\varphi/h^2}}}\right] \tag{2.39}$$

with $\varepsilon_0 = 4\varphi/es$. σ_0 is a temperature-independent material constant, T_1 relates to the activation energy required for fluctuation-induced tunneling and T_0 is the lower critical temperature. s is the particle separation distance, A the contact area, e electron charge, m electron mass, h Planck's constant, k Boltzmann constant and φ the potential barrier height at the tunneling junction. Since all proposed models simplify the particle network, neglect interface resistances or have to simplify conduction mechanisms, the transfer of model to experimental data is always difficult and fitting parameters may not always represent reasonable physical variables. An expansion by mesoscopic tunneling in nano-restrictions has been introduced by Xie and Sheng [191] to ascribe more realistic parameter values, although the mathematical description is fairly similar to FIT model.

A continuum model to describe the electrical conductivity of CNT nanocomposites was developed by Wang et al. [37]. An effective medium made from CNT and polymer with perfect interfaces is modified with a small interface layer and tunneling resistivity. Matos et al. [36] modeled CNT in a polymer matrix as 1D beams with hollow cylindrical cross-sections to reduce computing costs of a 3D model and came to good agreement between both methods. A finite element considering the tunnel current between two neighboring CNT was implemented in Abaqus based on Simmons equation [181]. Percolation behavior

as well as strain sensing ability of CNT composites could be modelled fitting available experimental data. [36]

Because most of the introduced models and parameters describe charge transfer mechanisms on nano-level that can not be proven by the measurements utilized within this thesis and the FIT model showed a fairly accurate description of the temperature-dependent behavior, the data presented in Chapter 6 will be analyzed with regard to FIT model and semiconductivity. To have a broad overview on found material behavior, this literature review ends with a comparative selection of reported CNP nanocomposite sensors and their characteristics.

For globular carbon black Medalia [43], Voet [192] and Aminabhavi [45] reviewed the temperature dependent resistive behavior. Agglomerate size, tunneling distance, contact resistance and morphology of the carbon black all influence the resistive behavior [43, 189]. The makromolecule structure of the polymer dictates the arrangement of particles or aggregates within the matrix. Crystalline structures undergo order and volume changes when melting. Interparticle distances are increased while melting and therefore direct contact conductivity and tunneling current decrease. Amorphous polymers allow Brownian movement of particles as well as more vibrations in the polymer matrix resulting in a more even distribution of particles and thus increased average particle distances [45, 192]. Balberg [35] also described the correlation between increasing volume of the polymer for increasing temperature and thus decreased over all volume content of carbon black in the nanocomposite to be the main factor in PTC behavior. The consideration of tunnel resistance influenced by thermal thermal fluctuation in dependence of applied electric field was described for globular carbon in PVC by Sheng et al. [184, 185].

With high aspect ratio CNT exhibit different properties depending on their morphology. For CNT the intertwined junctions between individual tubes have been considered by Fuhrer et al. [193] to distinguish metallic and semiconducting contact pairings. Simsek et al. [170] compared the behavior of DWCNT and MWCNT and found the main temperature-dependent charge transport mechanism to be following FIT behavior. The network morphology has been linked to the DWCNT tendency to agglomerate and thus offering fewer conductive pathways and thus lower overall conductivity. The temperature-dependent volume change and thus increase in tunnel gap distances has to be considered, especially above the glass transition temperature, where thermal expansion is more significant [194, 195]. The opposite behavior can be observed in CNT-filled hydrogels, which shrink with increasing temperature and thus show decreasing

resistivity [171]. Di Bartolomeo et al. [162] reported on the thermo-sensing behavior of MWCNT-films that exhibit comparable response time, long-term stability and monotonic dependence to platinum thermistors. The resistance decreases linearly with increasing temperature. Most systems are characterized for DC measurements. However, Li et al. [163] use the AC impedance of MWCNT/ PVDF composites to show PTC and NTC behavior in certain temperature regions. This is caused by melting of the crystalline PVDF phases, which occurs above the phase transition temperature. Without the crystalline polymer structure that increases the particle distance with increasing temperature in the lower region, the filler particles can form conductive pathways more easily in the melted state. [163]

With epoxy resin Neitzert et al. [173, 174] found a low-cost NTC temperature sensor by incorporating 0.5 wt% MWCNT. Oskouyi et al [167] used the experimental results from [174] to study the influence factors of filler loading, tunneling barrier height and filler resistivity. In their numerical study with CNT and graphene nano-platelet (GNP) composites, the latter show a more pronounced decrease in resistivity for elevated temperatures. Similar behavior is observed by Bahrami et al. [175] with MWCNT in conductive PPy matrix. The increasing conductivity of the composite with increasing temperature is mostly attributed to increased charge carrier concentration within the semiconducting material at elevated temperatures.

De La Vega et al. [164, 165] emphasized the filler content-dependent increase in resistance over temperature in MWCNT and CB epoxy nanocomposites. Lower filler content show a significantly higher PTC than with lower filler content since the volume changes of the polymer affect a sparser particle network more severely. Alamusi et al. [196] add to this observation by exploring the influence of filler content on the CTE, which is higher for low filler content. Njuguna [166, 176] elaborated on the influence of order and thermal history of MWCNT nanocomposites. The observed PTC could be attributed to thermal expansion of the matrix. Peaks in resistivity around the glass transition temperature are related to thermal relaxation peaks as observed in DSC measurements. Thin films with 2–3 wt% randomly dispersed MWCNT have been found to be a good temperature sensor. [166, 176] Obitayo et al. [177] report this behavior of NTC up to a certain temperature followed by PTC too in their review on MWCNT piezo-resistive strain sensors. Shen et al. [178] differentiated between intrinsic resistance change of filler particles in response to temperature changes and resistance changes introduced by volume changes of the epoxy matrix. For CB and

MWCNT NTC is shown with decreasing resistance for increasing temperature. The strong PTC influence in carbon black systems is attributed to the volume change of the matrix. Sanli [180] investigated DC resistance and AC impedance over temperatures below the glass transition of epoxy MWCNT films. Whereas resistance changes are following NTC behavior due to thermal expansion of the matrix the AC impedance response changes for elevated temperatures at higher frequencies and can exhibit PTC behavior due to dominating capacitive effects of the CNT network within the matrix.

The application of CNT nanocomposites as temperature sensors is discussed in the review of Monea et al. [179] emphasizing on the potential and lack of available experimental data for low-temperature ranges or cryogenic applications. A uniform dispersion and targeted manipulation of the CNT network is reported to be crucial to exploit the promising properties of CNTs temperature-dependent behavior. [179]

To conclude, the network structure of the CNP fillers has to be considered in discussing the results presented in chapter 6. The DC resistive response will be interpreted with regard to gained knowledge from the comprehensive literature review.

3 Materials and Methods

3.1 Carbon Nanoparticles

Within this thesis, CNP of different morphology have been used to determine the influence of shape, specific surface area or rheological behavior. As spherical particles carbon black Printex L [197] by Orion Engineered Carbon, USA, was selected. It is recommended for conductive coating applications in liquid or powder-based coating systems. Mostly planar few-layer graphene AVAN2 [198], supplied by Avanzare Innovacion Tecnologica S.L., Spain, was chosen to investigate the effect of incorporating planar particles of high aspect ratio which can find use in electromagnetic shielding or surface enhancement of coatings. Since carbon nanotubes are of high interest to reinforce polymer matrices with low filler content for conductive applications two different types of CNT have been investigated. Multi-walled carbon nanotubes NC7000 [199, 200] by Nanocyl S.A., Belgium, are available on large scale for different application fields like coatings, fiber-reinforced composites or modification of material in additive manufacturing. Lastly, single-wall carbon nanotubes Tuball [201, 202], OCSiAl, Russia, have been chosen due to their high aspect ratio and thus minimal filler content in conductive polymer composite applications. Different purity of 75 % and 99 % SWCNT in the powder allow to distinguish the SWCNTs response with regard to metal catalyst residues. Characterization of most particles via TEM for counting agglomerate size, stacked layers or bundle sizes and BET to determine the specific surface area (SSA) has been done in a previous thesis by H. Voormann [2] and can be referenced accordingly.

In Figure 3.1 SEM images of all particles addressed within this thesis can be seen at 75k magnification to distinguish their morphology. The first row depicts carbon black and few-layer graphene, the lower row all CNT types.

Carbon black Printex L shows spherical shape with diameter of 20-40 nm. From the SEM image, the agglomeration of particles on meso- and macro-scale can be observed. The specific surface area of Printex L was measured to be $125\,\mathrm{m^2/g}$ [2]. Carbon black agglomerates can be dispersed easily, the narrow size distribution

allows use not only as a nano-filler in rubber or polymer products but also as color pigments in inks. The second depicted CNP in the upper row is AVAN2 few-layer graphene. From SEM images the lateral size of particles is difficult to determine between 2 µm for strongly fragmented pieces and up to 70 µm. Also, the defect-caused crinkles in the graphene planes are visible, as well as stacks of layers due to the van-der-Waals forces between neighboring sheets. The SSA has been determined to be $128\,m^2/g$, the number of layers stacked together is 10 ± 2 according to [2]. The exfoliation of graphene layers requires either chemical assistance or high shear forces. FLG is prone to reagglomerate when the dispersion is not stabilized by sufficient particle separation.

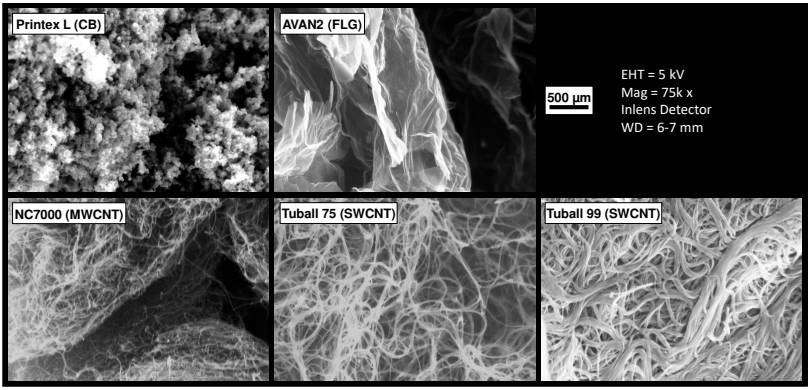

Figure 3.1: SEM images of all CNP investigated

For CNTs, the magnification of SEM with up to 150k does not give a sufficient resolution to distinguish individual tubes. Therefore, the images in Figure 3.1 show bundles of multiple CNTs. NC7000 are multi-walled CNT showing a highly entangled network of tubes on a meso-scale. On macro-scale the MWCNTs are in a form of a fine powder. Specific surface area was measured to be $321\,m^2/g$, the diameter could be measured to be $12\,nm \pm 3\,nm$ and bundles consist of about 10 tubes each. Bundles are then forming the powders agglomerates of several micrometers in diameter. According to the data sheet [199], the length of NC7000 tubes is about 1 µm. In comparison to spherical or planar CNP the tubes are more difficult to separate in a dispersion process. The single-wall CNT Tuball 75 and Tuball 99 are even longer tubes according to the data sheet with up to 5 µm [201]. SSA are low compared to literature with $605\,m^2/g$ measured in [2]. But looking at the SEM images, large bundles of parallel oriented tubes up

to thicknesses of several hundred micrometers can be seen, which decreases the available surface area. Whereas a singular tube has a diameter of about 1.5 nm, there are a minimum of 15 tubes in even the smallest bundles, but on a meso-scale several hundred of these bundles are aligned to larger strands of CNTs. The high aspect ratio and tight entanglement of the tubes shows on macro-scale, as the material is more like small cotton flakes than a powder. Flakes of several millimeters in diameter easily stick together making a dispersion process prone to re-agglomeration and compaction of dry particle bundles.

3.2 Polymer Resins

Since the institute's field of interest lies in duromer composites, frequently used epoxy resins are chosen for experiments. EPON 828, by Hexion Inc., Columbus (OH), USA, is a standard bisphenol A-diglycedyl-ether (DGEBA) based epoxy resin, commonly used in industry as the base of epoxy formulations. Its epoxy equivalent weight (EEW) is 184-190 g/eq and the epoxy group content is 5260-5420 mmol/kg. The derivation EPON 828LVEL, Hexion Inc., Columbus (OH), USA, is a product developed for infusion and exhibits lower viscosity than 828 and has reduced hydrolyzable chlorine content to secure use in electrical applications. Its EEW is 182-187 g/eq and epoxy group content 5340-5500 mmol/kg. Within the experimental time of this thesis, Hexion canceled the supply of 828 resin, so only 828LVEL was available. Another epoxy resin often used in recent projects is EPON RIMR 135, Hexion Inc., Columbus (OH), USA, a low-viscosity infusion resin developed for rotor-blade manufacturing. It is a DGEBA-epoxy modified with several reactive diluents to decrease its viscosity. RIMR135 EEW is 166-185 g/eq and the epoxy group content is 5400-6000 mmol/kg.

Curing agent Hexion RIMH137, Hexion Inc., Columbus (OH), USA, is used. Its amine value is 400-600 mgKOH/g, the amine hydrogen equivalent weight AHEW is about 52 g/eq. Mixing of resin and curing agent was done with a stoichiometric ratio according to EEW and AHEW.

In the research project SCALE - Nano2Industry the base resin to produce a 1 wt% Tuball 75 masterbatch was an unsaturated polyester-/ vinyl-ester resin base mixture by BÜFA Composite Systems, Rastede, Germany. The masterbatch to be produced within the project is thus called UPT75. Exact constituents of the base resin underlie an NDA, since the formulation of resin, rheology and dispersion additives is part of BÜFAs distributed products.

3.3 Three-Roll Milling (TRM)

Due to highest possible shear amplitudes and shear rates three-roll milling is a suitable method to process particle-filled resin systems. [64, 104] Dispersions of high quality can be manufactured efficiently and reproducible with various particle types, matrix systems and filler content. A dispersion process is characterized by the rotational speed of the rollers n_i, gap spacing h, working gap width AB between the side guards and temperature T set by a cooling fluid running through the rollers. Following schematic Figure 3.2 shows the principle of dispersion on a TRM. Material is fed into the back gap 1, the feeding gap, between the rollers with the lowest rotational velocity. To generate the high shear amplitudes between rollers, the velocities are set by a fixed gear ratio of 3:1. The material is sheared a second time in gap 2, the dispersion gap before it is removed from the front roll by the apron blade.

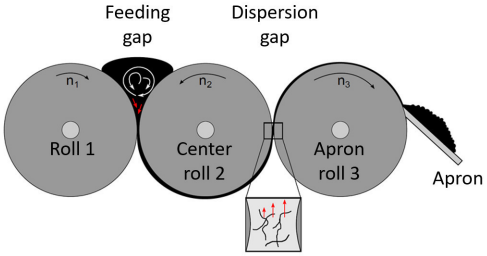

Figure 3.2: Schematic depiction of dispersion on a TRM

The standard processing conditions are seven steps with gap spacing and roller speed as listed below in table 3.1 at a set temperature of 20 °C. The ratio between feeding gap spacing and second gap is always about 3:1 following the fixed gear ratio. The rotational speed of the apron roll on an 80E *Plus*$^+$ TRM is set to 450 rpm and has been adapted to have comparable shear rates to the larger TRM 120E-250, which is run in a standard process at the same gap spacing but rotational speed of 300 rpm. [203]

3.3.1 Machines

Within this thesis, two different TRM models of EXAKT Advanced Technologies GmbH, Norderstedt, Germany, have been utilized for dispersion processes. The medium-sized TRM 120E-250 is depicted in Figure 3.3 a). The stainless

Table 3.1: Standard dispersion process on a 80E *Plus*$^+$ TRM [203]

Step	Gap 1 (µm)	Gap 2 (µm)	n_1 (rpm)	n_2 (rpm)	n_3 (rpm)
1	120	40	450	150	50
2	40	13	450	150	50
3-7	13	5	450	150	50

steel rollers have 250 mm maximum working width AB and a roller diameter of 120 mm. The machine can be set to work within a constant gap width dispersion mode or a constant force mode. Gap width can be adjusted between 5 µm and 200 µm. Tracking of occurring line forces and set gap width or rotational speed is possible via an external measuring box, which accesses the machine data from an additional computer. The system is an experimental set-up as a prototype for in-line measurements implemented in later TRM models.

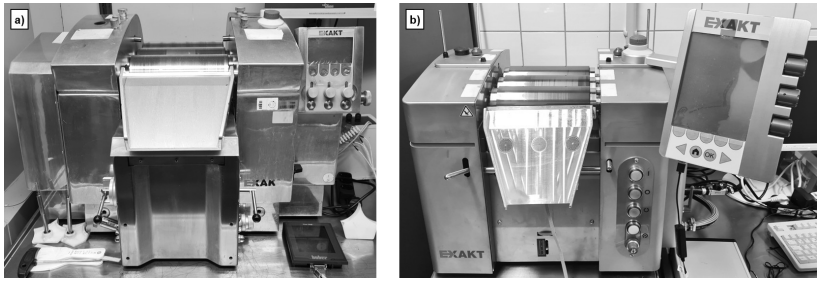

Figure 3.3: Photographs of used machines a) TRM 120E-250 with stainless steel rollers and b) TRM 80E *Plus*$^+$ with SiC rollers

The TRM 80E *Plus*$^+$ is a newer model with smaller roller diameter of 80 mm and with a stiffer set of silicon carbide (SiC) rollers (compare Fig. 3.3 b)). These have been developed to provide better surface quality, abrasive behavior and higher heat dissipation ability. The construction of the TRM has been improved in this later generation as well since a higher machine stiffness was achieved to secure capability of processing highly viscous materials in a constant gap width dispersion mode. The TRM *Plus*$^+$-series has an integrated monitoring for temperatures, rotational speed, gap width and occurring line forces in both gaps. A display provides visual live data, an USB-link can be used to write data to an external storage for further analysis.

3.3.2 Review of Previous Monitoring Methods for Production Application

Based on the thesis of Voormann [2] several monitoring methods have been reviewed in a series of pre-experiments. The UPT75 masterbatch was chosen to rate and select the different characterization methods for a high filler content, high-viscosity material, that has not been considered before.

In-Line Monitoring

On both TRMs the tracking of temperature in different locations, chosen gap settings, rotational speed and resulting line forces is possible. After calibration of the zero gap, the processing gap width h is set between all rollers by the machine controller and thus can be saved for data export. The same goes for settings of rotational speed of all rollers. The occurring force is measured in Newton between each pair of rollers so that gap 1 and gap 2 can be distinguished. With the working gap width AB between the side guards, the force signal is normalized to a *line force* with unit N/mm. This line force is the focus of intensive studies for dispersion processes of various materials within this thesis.

In Figure 3.4 the line forces in both gaps are plotted over the dispersion process time. As can be seen, the line force is zero for an empty gap, whereas material between rollers leads to a sudden rise of measured line force. Step 1 is the homogenization step with largest gap spacing, resulting in a short signal with lowest overall values. With decreasing gap spacing in steps 2 and 3 the line force signals increase significantly showing maximum value peaks towards the end. With continued lowest gap spacing of 13/5 µm the maximum measured value decreases again and the peaks disappear. Smaller gap spacing shows longer dispersion time necessary to process a batch of material. Additionally, the temperature measured within the three rollers of the TRM is shown, a constant rising can be observed due to heat dissipation from the machine's motor and process friction in various places.

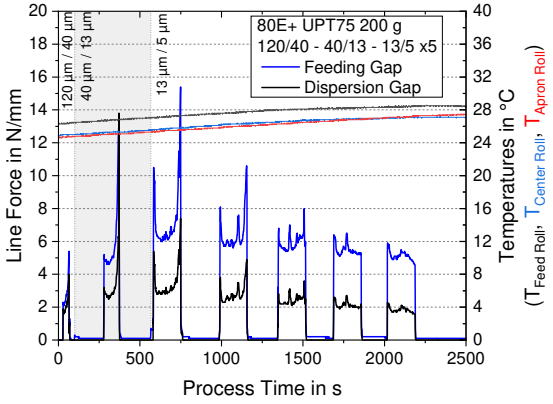

Figure 3.4: In-line monitoring of a 1 wt% UPT75 masterbatch dispersed in 7 steps on a TRM 80E *Plus*$^+$

A major aim of the research project SCALE - Nano2Industry was to further investigate influences on the line force signal and add another in-line monitoring method to be implemented on the TRM. Chapter 4 presents the progress made on this topic.

Off-Line Monitoring

For characterizing the processed material the possibility to take small samples from within different dispersion steps was used to choose from a catalog of optical or electrical characterization methods.

For example, light microscopy can be used to analyze the size and number of agglomerates in a sample. Since masterbatches with higher filler loading are of high absorbance, thin samples have to be prepared on glass slides by scraping a 30 µm film for transmission light microscopy. Decreasing agglomerate size can be observed throughout the dispersion steps until the particle network is optically non-distinguishable anymore due to the maximum possible resolution of the used microscope at 5 µm. In Figure 3.5 the dispersion progress can be observed from pre-mixed resin with SWCNT agglomerates in step 0 to an optically fully dispersed batch from step 5 to step 7.

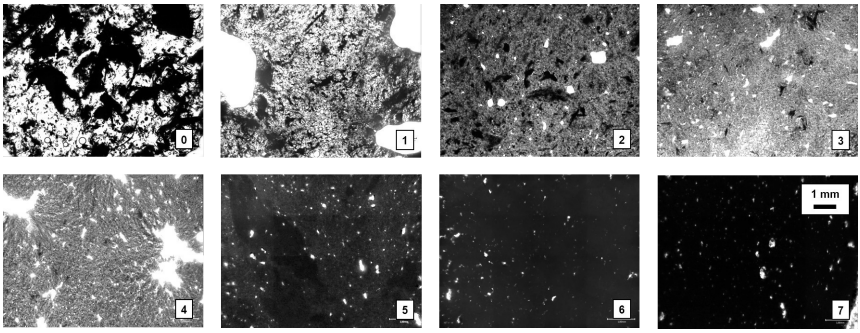

Figure 3.5: Characterization of a 1 wt% UPT75 masterbatch from pre-mixed material (0) to fully dispersed batch after step 7 via transmission light microscopy

Another visual offline characterization method is grindometry as shown in Figure 3.6, which probes the size of agglomerates of a dispersion by scraping a sample in a groove of defined width and decreasing depth. Contained agglomerates are pushed forward by the application blade from the depth of the groove that undergoes the particle size resulting in scratches in the material film. This way the largest agglomerate size of a sample and a quantitative impression of contained particle sizes can be determined. In Figure 3.6 selected grindometry images from pre-mixed material (0) with large agglomerates up to fully dispersed material (7) are depicted. After the first homogenization step, the structure of the material film already changes drastically. The grindometric scale goes from 100 µm on the left to 0 µm on the right. In dispersion step 1 scratches can be seen over the whole scale due to a large initial dispersion gap spacing of 120/40 µm. The scratches from larger agglomerates vanish with progressing dispersion steps until the last 13 µm scratches from step 5 are completely gone in the final step 7. Grindometry is thus a fast tool to characterize samples from a dispersion process regarding their remaining agglomerate size.

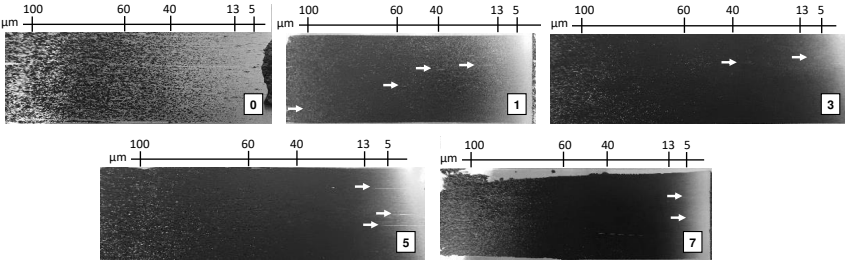

Figure 3.6: Characterization of a 1 wt% UPT75 masterbatch from pre-mixed material (0) to fully dispersed batch (7) via grindometry

Oscillating rheology is utilized to determine the complex viscosity of the material throughout processing steps. The particle network build-up could be observed and linked to the state of dispersion. [116] The electric conductivity of CNP allows additional electric characterization of samples via in-situ DC-measurements during rheology to determine the shear-rate influence on the particle network.

Additionally, optical coherence tomography (OCT) was tested as a monitoring method that uses light scattering in a sample to scan material structures on a micro-scale. THORLABS GmbH, Lübeck, Germany, offered to test their system Vega VEG210C1 with a central wavelength of 1300 nm, the maximum axial resolution of 16 µm in air and A-scan rate of 100 Hz. Figure 3.7 shows two cross-sections of masterbatch before dispersion and after full dispersion. A maximum penetration depth of 700 µm for the unprocessed and 220 µm for the fully dispersed material could be achieved with the 1 wt% UPT75 masterbatch. Due to high absorbance of the high filler content the script developed previously by Voormann [2] for a 0.01 wt% and 0.05 wt% masterbatch could not be applied to determine the agglomerate particle size distribution. Scans have been acquired as 3D mappings from which arbitrary 2D cross-sections can be selected for visualization. The two images in Figure 3.7 show the dispersion progress in terms of decreased grains of the visible material film for the scan from step 7 whereas step 0 shows slightly more optical heterogeneity. Also the fully dispersed material shows significantly decreased penetration depth of OCT within the sample which is linked to the full formation of the particle network shielding the measuring wavelengths.

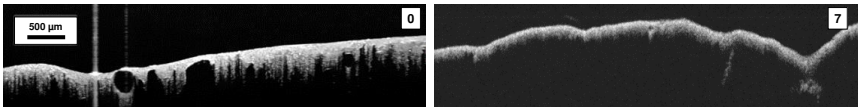

Figure 3.7: Characterization of a 1 wt% UPT75 masterbatch from pre-mixed material (0) to fully dispersed batch (7) via OCT

Active thermography has been applied to characterize the material's dispersion state using the thermally conductive properties of carbon-based dispersions as it has been proven to be suitable in literature. [204–206] Similar to the visual investigations via light microscopy the samples have to be prepared as a thin and even spread film on a glass slide, that is optically transparent to the applied measuring wavelengths (400-950 nm) [207]. The Calorsito VIS-NIR by NanoLockin GmbH, Fribourg, Switzerland, allows for quantifying the heat absorption of a sample within about 3.5 mm^2 in a measuring time of 3 min. Figure 3.8 shows the heat maps on the left side for masterbatch material from pre-mix (0) to fully dispersed masterbatch (7) as well as a diagram on the right side summarizing the quantified signal amplitude of the thermal images to show the progressing dispersion state.

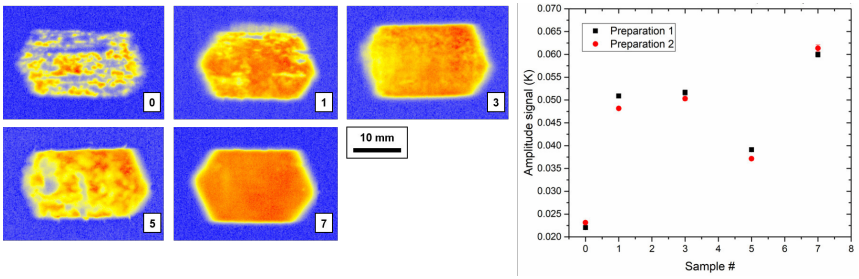

Figure 3.8: Characterization of a 1 wt% UPT75 masterbatch from pre-mixed material (0) to fully dispersed batch (7) via active thermography

As can be seen, the samples homogeneity increases with dispersion steps, the results are reproducible for two different sample preparations as well. However, in step 5 the homogeneity appears to be lower than in step 3, which can be explained by occurring material separation in the dispersion process and sampling a probe from higher-viscous concentrated material. As with all sample-based

offline methods, the limited amount of a test batch makes active thermography prone to measure inhomogeneity in a non-representative way, furthermore, the preparation has to be done rather carefully and lastly, the measurement itself takes a significant amount of time, which prevents this method from being implemented as an in-line monitoring method.

Impedance spectroscopy has been investigated in the previous work of Voormann [2] to determine the conductive particle network state within the dispersion and was recommended for further research. Material was tested with cylinder electrodes as described in section 3.8 and compared for different dispersion steps. Measurements span a frequency spectrum and give the result for complex impedance and phase angle. Different frequency regions correspond to different conductive network scales of the particles from nano-network of singular particles to macro-network of agglomerates. Over the dispersion steps the decrease of complex impedance can be observed.

Figure 3.9 shows the last step 7 of several dispersion processes. The epoxy resins EPON 826, 827 and 828LVEL have been investigated by Voormann [2, 203] as well as Tuball 75 SWCNT and NC7000 MWCNT. Filler contents from 0.01 wt% to 0.7 wt% were used. From the diagram differences of absolute complex impedance in Ohm can be seen as well as different impedance values for different frequency regions. Neat resin or low filler contents with solid lines show highest impedance. The lowest impedance has been achieved for highest filler contents. Over a full dispersion process, the complex impedance undergoes similar changes starting from high values getting lower with each dispersion step. The UPT75 masterbatch addressed within the project SCALE - Nano2Industry can be seen in the lowest impedance range (gray solid line), which challenges the monitoring method in new orders of magnitude. Ideal capacitors as the neat resins or the low filler content dispersions show a continuously decreasing complex impedance value over increasing frequency. An ideal resistor would show a constant impedance and phase angle of 0°. Most dispersions depicted in Figure 3.9 show mixed behavior since the nano-network of CNP is developed within the dielectric resin matrix on different length scales responding to different frequencies. Dispersions with lower filler content show more capacitive behavior like the neat resin. High filler content shows two resistive ohmic regions which are attributed to percolated nano-network and conductive bulk-behavior including tunneling.

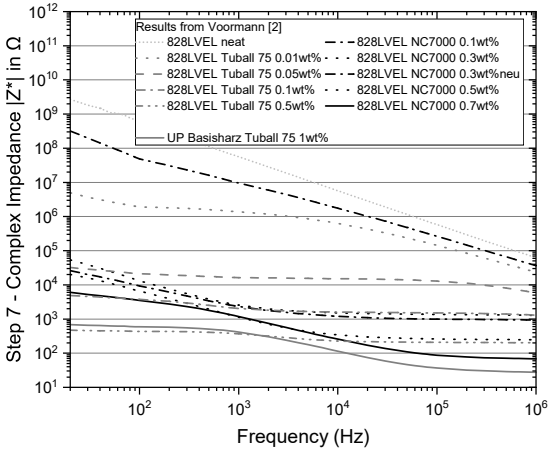

Figure 3.9: Impedance Spectroscopy of different CNP and filler content as measured in [2] in comparison to the UPT75 masterbatch investigated within this thesis (gray solid line)

3.3.3 Limitations and Optimization Potential for Monitoring the UPT75 Masterbatch Production

The UPT75 masterbatch with 1 wt% Tuball 75 SWCNT is a high-viscosity nano-intermediate that is difficult to characterize. All optical methods are challenging because the high filler content absorbs most of the light and very thin films have to be produced to shine through with light microscopy or active thermography. Within the dispersion process, those films only occur on the rollers, where the rotational speed limits the characterization via OCT or microscopy due to necessary exposure or scanning time. The viscosity of up to 10 kPas disables flowing of the product through small sampling tubes for electrical measurements. An additional sample extraction would have to be implemented, which would only enable on-line quality assessment but not in-line monitoring. Therefore, further parameter studies on line force interpretation and an in-line implementation of impedance measurements are the most promising routes for in-line monitoring. Chapter 4 presents the experiments concerning line force influences and the implementation of impedance measurement including its validation with various CNP dispersions.

3.4 Nanocomposite Manufacturing

CNP-modified resins are mixed with the curing agent by stoichiometric ratio using a dual asymmetric centrifuge Speedmixer DAC 150.1 FVZ, Hauschild GmbH & Co. KG, Hamm, Germany. Afterward, the uncured material can be cast in different molds. All molds are non-reacting with the epoxy and secure a desired sample size and shape. Closed molds are used to manufacture larger plates of nano-composites, which can be used to mill out different shapes of specimens later. In this process, a closed and sealed mold with an inlet and an outlet can be infused with the uncured polymer mix by applying vacuum to the cavity. Open molds enable quick casting of composite samples, which do not need a perfect plate shape. All samples are cured at room temperature for 24 h and tempered afterward for 15 h at 80 °C in an oven UF30plus, Memmert GmbH & Co. KG, Schwabach, Germany.

3.5 Specimen Preparation

Samples from composite plates are contour milled with a EuroMod 30, isel Germany AG, Eichenzell, Germany with a 1.8 mm single edge milling tool or cut with a precision saw Brillant 220, ATM Qness GmbH, Mammelzen, Germany with 150 µm diamond or 1 mm corundum saw blades. Surface finishing is achieved either by manual polishing up to 2500 grit sandpaper or via rotational grinding plates Saphir 360, ATM Qness GmbH, Mammelzen, Germany. Grinding steps include 320 and 600 grit depending on surface roughness in the beginning. Changes to 800, 1000 and 2500 grit are conducted after visual control and cleaning of the samples in an ultrasonic bath.

3.6 Optical Microscopy

Images of agglomerates in dispersion, the microstructure of composites or other micro-scale characteristic sample features are recorded with a digital microscope VHX-6000, Keyence Deutschland GmbH, Neu-Isenburg, Germany.

3.7 Electron Microscopy

Scanning electron microscopy is performed at the TUHH electron microscopy unit (BeEM) on a Zeiss Supra VP 55, Zeiss, Oberkochen, Germany, with an acceleration voltage between 2 kV and 15 kV to analyze the morphologies of CNP

and to determine chemical constituents via energy dispersive X-ray spectroscopy (EDX).

A Phenom XL, Thermo Fischer Scientific Inc, Waltham, MA, USA, is used for low magnification investigations on CNP nanocomposites at an operating voltage of 5 kV and secondary electron detector.

Samples are prepared on standard aluminum SEM stubs (diameter 13 mm) with adhesive carbon pads and silver paint Acheson 1415, PLANO GmbH, Wetzlar, Germany, to improve the charge dissipation on larger specimens' edges. For composites of no or low electrical conductivity a thin layer of gold is sputtered on the surfaces using a BAL-TEC Sputter Coater SCD 050, Balzers, Liechtenstein [208] at BeEM.

Transmission electron microscopy with BeEMs FEI Talos F200X, Thermo Scientific, at an acceleration voltage of 200 kV is used to determine the number of layers or walls of the CNP. Particle powders are ultrasonicated in methanol using a UW 2200, Bandelin electronic GmbH & Co KG, Berlin, Germany, with a set amplitude of 30 %, pulse and break in between of 1 s over a duration of 30 s. The dispersion is placed drop-wise on a circled copper TEM grid with lacey carbon film (400 mesh), PLANO GmbH, Wetzlar, Germany, with a diameter of 3.05 mm.

3.8 Electrical Characterization

Impedance spectroscopy is conducted at 1 V with frequencies between 20 Hz and 1 MHz using a HP 4284a Precision LCR Meter, Hyogo, Japan, with a cylinder-electrode set-up. For that, liquid material can be filled void-less in a polypropylene tube, contacted by cylindrical aluminum electrodes from each side to create parallel electric field lines within a reproducible sample volume. For comparison a Metrohm Autolab PGSTAT204, Darmstadt, Germany, is used to perform impedance spectroscopy at even lower frequencies down to 0.01 Hz.

The electrical resistance during rheological characterization is measured with a source measure unit 2601A SYSTEM SourceMeter, Keithley Instruments Inc., Cleveland, OH, USA. Applied DC voltage is 1 V, the measurement is time continuous and coupled to the rheology test script.

The electrical resistance is measured in a four-wire set-up with a ten-channel Multimeter 2000 Keithley with a 2000-SCAN card, Keithley Instruments Inc., Cleveland, OH, USA. The set-up enables the continuous measurement of up

to five samples because the adapter card is able to switch channels at a given rate. The temperature sensing study of CNP nanocomposites in Chapter 6 is conducted with a rate of 1/3 Hz. The specific electrical resistance ρ is calculated with measured resistance R, cross-section A and sample length l by

$$\rho = R\frac{A}{l} \quad (\Omega m) \tag{3.1}$$

The specific electrical conductivity σ can be calculated by

$$\sigma = \frac{1}{\rho} = \frac{l}{R \cdot A} \quad (S/m) \tag{3.2}$$

3.9 Rheology

Rheological characterization of liquid samples is conducted using a Kinexus Ultra+ rheometer, Netzsch, Selb, Germany. Plate-plate configuration with 40 mm diameter and a gap spacing of 0.5 mm is chosen. Angular frequency, shear amplitude and test temperature are noted besides the experimental results. All measurements are conducted in oscillation, which is characterized by a time-dependent shear deformation γ of the sample [209]:

$$\gamma(t) = \hat{\gamma} \cdot \sin(\omega t) \tag{3.3}$$

The shear amplitude $\hat{\gamma}$ is defined by the angular deformation divided by gap spacing h. The shear frequency is given by the periodic oscillation with time T:

$$f = \frac{1}{T} \tag{3.4}$$

The shear stress τ is proportional to the complex shear viscosity η^* and depends on the shear rate $\dot{\gamma}$

$$\tau = \eta^* \cdot \dot{\gamma} = G^* \cdot \dot{\gamma} = G' \cdot \hat{\gamma} \cdot \sin(\omega t) + G'' \cdot \hat{\gamma} \cdot \sin(\omega t) \tag{3.5}$$

G^* is the complex shear modulus consisting of storage G' and loss modulus G''. A loss factor $\tan(\delta)$ can be defined as

$$\tan(\delta) = \frac{G''}{G'}. \tag{3.6}$$

3.10 Temperature Dependent Characterization

CNP nanocomposites are tested as temperature sensors in a wide range of temperatures from −50 °C to 170 °C. This range has been defined by the temperature range of the climate chamber TempEvent T/180/70a/3, Weiss Technik, Reiskirchen-Lindenstruth, Germany. Since the convection chamber has a volume of 190 l a slow rate has to be chosen to secure homogeneous temperature distribution in the chamber and directly at the sample surfaces. A heating ramp with equal temperature distribution over the whole range has been experimentally determined to be 1.43 K/min. The temperature minimum is limited by experimental time which prolongs significantly in the range between −50 °C and −70 °C.

Differential scanning calorimetry (DSC) is performed with a 204F1 Phoenix F1, Netzsch Gerätebau GmbH, Selb, Germany. The heating and cooling rate under nitrogen atmosphere is 10 K/min. After an initial cool down to −50 °C the same temperature range of the climate chamber is scanned to characterize material transition temperatures. After reaching 170 °C a ramp down to 20 °C and second heating and cooling is measured to secure no cross-linking reaction occurs by heat treatment of the sample material. Samples are cut from the manufactured plates with regard to having an even lower surface for ideal contact of the samples to the aluminum pans with pierced lids.

Dynamic mechanical thermal analysis (DMTA) is performed using samples of 2 mm thickness and 5 mm width on a Gabo Eplexor 500N, Netzsch GABO Instruments, Ahlden, Germany. To see glass transition and a low temperature β-transition a temperature range from −100 °C to 170 °C is chosen. The clamp distance and free test length L_0 is 30 mm.

The DMTA chamber is also used as an alternative climate chamber in later experiments by running a regular tension DMTA test while placing other samples for DC resistivity measurements in the unused empty space without interfering the mechanical characterization.

3.11 Magnetic Field Characterization

The magnetic field of different test set-ups is quantified by using the hand-held transverse Magnetometer KOSHAVA-AT, Wuntronic GmbH, Munich, Germany. A magnetic flux in Tesla is measured as a scalar with this magnetometer.

4 In-Line Monitoring of the Three-Roll Milling Process

Characterizing the dispersion state during processing is of interest because an in-line monitoring method would provide precious insights for process optimization and reduction of processing time and production costs.

Research Question

How can different characterization methods be integrated into the TRM to form a sufficient in-line monitoring tool giving insight into different materials, process stability and dispersion state?

Two routes for three-roll milling are investigated as they have shown to be most promising to provide a reliable monitoring method: Observing the line forces occurring in the two gaps between rollers and impedance measurements of the processed material.

4.1 Line Force Interpretation

The previous knowledge of occurring line force (LF) signals as described in section 3.3.2 was expanded by testing several other materials and correlating signals to certain phenomenons to answer following question:

Research Question

How do viscosity, filling height in the feeding gap, filler content and gap width influence the line force of the dispersion process?

Following schematic diagram 4.1 shows the different signal types in the dispersion process on the TRM that have been observed for carbon nanoparticle-filled systems of various kinds so far. The feeding gap 1 and the dispersion gap 2 usually show different force values, the second gap laying under gap 1. Even

if current understanding suggests that ideal material transport over the rollers would show equal signals for both gaps and thus the usually observed lower line force in gap 2 is due to lower productivity, their difference is not fully understood yet.

The empty gap shows no line force when no material is filled in the feeding gap. Feeding the material leads to a sudden rise in the line force signal. Throughout the dispersion step, the line force can show different progression. A constant value indicates a steady material transport in the gap and thus constant productivity. Depending on the viscosity, this value is higher for more viscous material and lower for low viscosity. A decrease in the signal means either decreasing productivity in terms of volume flow or a change in viscosity due to rising temperature for example. A continuous increase of the line force over processing time can be observed if the viscosity rises (e.g. polymerization reaction, evaporation of solvents) or material gets deposited on the rollers, minimizing the gap spacing. For inhomogeneous material, the signal oscillates and thus represents changes in viscosity. Towards the end of a dispersion step, a sudden rise in the shape of a force peak can be seen in filled systems. This is a typical separation behavior of resin and particles. It occurs when the resin is dragged into the dispersion gap first leaving the particles behind. At the end of a step, the highly concentrated residual resin with most of the particles is transferred by the rollers leading to high forces. High filler content, almost dry material is compressed between rollers leading to line force peaks.

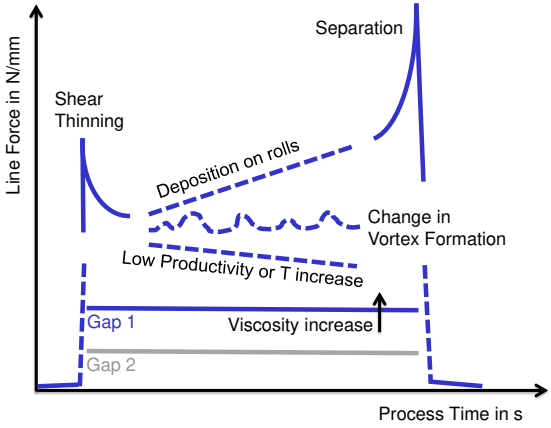

Figure 4.1: Line force signal forms

Following influence factors depicted in Figure 4.2 are affecting the dispersion of material on the three-roll mill and thus can affect the detected line forces:

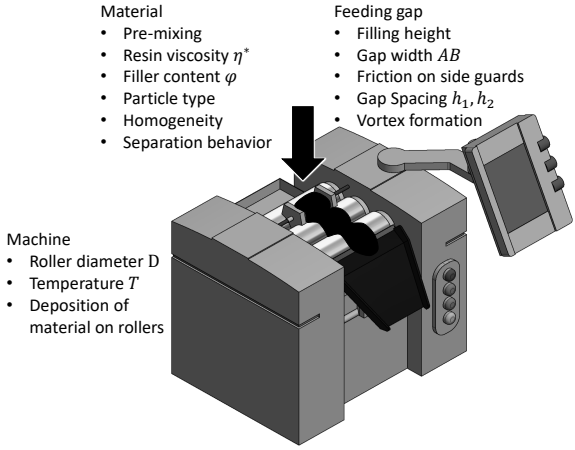

Figure 4.2: Influencing factors on the line force signal

The material has the largest influence with viscosity, filler content, filler type, homogeneity resulting from previous mixing or the general separation behavior. The machine determines the processing temperature affecting the resin viscosity, the roller diameter and deposition of material on the rollers. Lastly, the feeding gap introduces the material in each step and thus affects the line force by chosen gap width, friction on side guards or the gap spacing. Vortex formation possibly influenced by filling height of the gap has to be considered.

4.1.1 Influence of the Materials Viscosity

Following Figure 4.3 shows the dependency of viscosity of UP base resin on frequency and shear strain. It can be seen that within the tested shear strain range of 0.01–10 % strain over all tested frequencies of 0.01–10 Hz the complex shear viscosity is on a constant value of about 5 Pa s at 20 °C. No shear thinning or frequency-dependent alteration of the complex viscosity is noticeable. This is to be expected because the UP base resin is a resin formulation to secure stable processing behavior in a variety of products. For low frequency and minimal shear strain (black squares) measured values differ due to inertia effects of the rheometer which superimpose the material response.

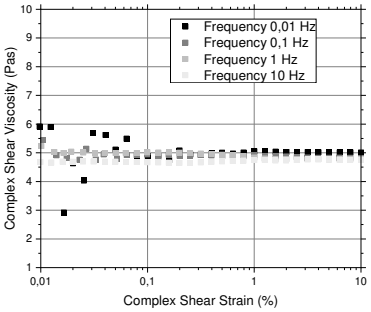

Figure 4.3: Frequency and strain-dependent complex shear viscosity at 20 °C

The temperature-dependent behavior of UP resin at 1 % strain for different frequencies is shown in Figure 4.4. Diagram 4.4a) shows all frequency sweeps for the respective temperature. It can be seen that the complex viscosity decreases with increasing temperature without showing a frequency-dependent alteration. For high temperatures with therefore low viscosity and low test frequencies the inertia effect can be seen again. At higher frequencies (T-dependent above 10 Hz) the measured curves show instabilities as well. This can be attributed to the instability of the material within the gap. The signal-to-noise ratio for those data points is high, so they can be disregarded for interpretation. A stable measuring range for temperature and frequency sweeps at 1 % strain thus can be defined for a range of 0.1–10 Hz.

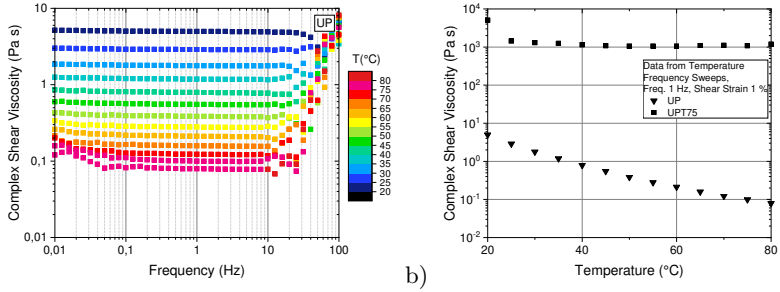

a) b)

Figure 4.4: Temperature-dependent complex viscosity of a) neat UP resin in temperature-frequency sweep at 1 % strain and b) comparison of neat UP and UPT at 1 Hz oscillation and 1 % strain

In Figure 4.4b) a summary for 1 % shear strain at 1 Hz is shown for the neat resin in comparison to the masterbatch UPT75. Whereas the exponential decrease of viscosity over temperature can be seen for the neat resin, the masterbatch shows temperature-independent behavior above 40 °C. This is attributed to the elastic particle network that increases the viscosity overall and dominates the behavior above a critical temperature, where the resin viscosity changes occur in orders of magnitude that are way below the CNT network's elastic response.

On the TRM the temperature and accordingly altered viscosity corresponds to a change in the occurring line forces. In Figure 4.5 the line force over all seven steps of the standard process with neat UP resin can be seen for an 80E *Plus*$^+$ with 85 mm working width. The processing temperature defined by the cooling fluid in the rollers is set to 20 °C. As can be observed the temperature measured within the three rollers are slightly higher due to the dissipated heat from the machine and friction occurring between roller 3 and the apron blade. Therefore, the temperature measured in the front roller 3 is always the highest. Over the seven steps a slow rise of the temperature from initial 22 °C by 1 K can be observed. The temperature rises in between steps when no product is processed because no gliding film of resin can reduce the friction of side guards or apron blade and rollers. The line forces vary according to the gap width h, increasing with decreasing gap width. Thus, a maximum line force of about 4 N/mm occurs for a minimum gap of 13/5 µm. With increasing temperature, the average line force per step drops slightly.The overall processing time for all steps is 520 s.

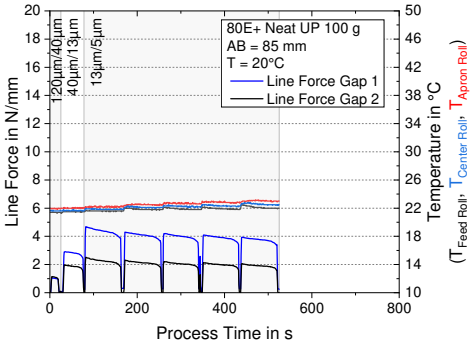

Figure 4.5: Line forces of neat UP resin for a standard 80E *Plus*$^+$ process at 20 °C

In Figure 4.6 the standard steps of processing neat UP resin are compared for gap 1 between 20–40 °C. The temperature levels are stable for each process. It should be noted that 40 °C set by the cooling fluid cannot be reached in the rollers, since the heat dissipates towards lab conditions of around 23 °C. Thus, the measured temperature is stable around 38 °C With rising temperature two phenomenons can be observed - an increase in processing time for the steps with smallest gap spacing and a decrease of the line force. For 30 °C the mean line force decreases by 25 % to a level of 3 N/mm and the total processing time is by 25 % longer than for 20 °C. For 40 °C the average line force in the last steps is 2 N/mm, so reduced by 50 %, whereas the overall processing time is prolonged to 700 s has increased by 35 %. The temperature can be set to 45 °C as a maximum before the TRM shuts down for safety reasons. Processing of material at higher temperatures is thus not possible and therefore no other change in viscosity by variation of temperature is not discussed here.

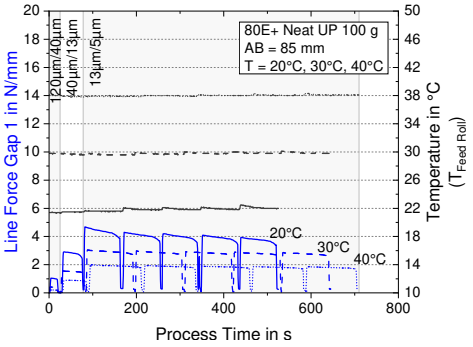

Figure 4.6: Line forces in gap 1 of neat UP resin for a standard 80E *Plus*$^+$ process at different temperatures

However, a significant increase in viscosity can be achieved by adding filler particles. The maximum filler content discussed within this thesis is the 1 wt% Tuball 75 masterbatch UPT75 shown in Figure 4.7. The viscosity increase by factor 100 at 20 °C leads to doubling in the mean line forces. A significant change in material behavior can be observed with severe separation peaks towards the end of the first three steps. The overall processing time is increased by 8 %.

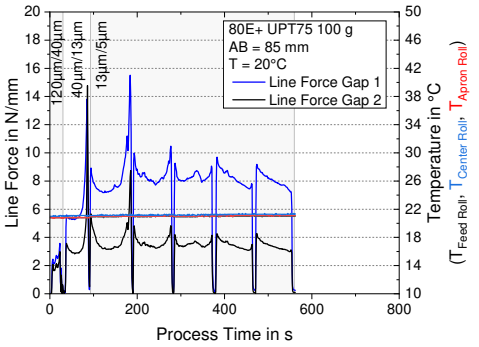

Figure 4.7: Line forces of UPT75 for a standard 80E *Plus*$^+$ process at 20 °C

4.1.2 Influence of the Dispersion Gap Width

The gap width determines the volume flow of material on the TRM and should therefore be increased to a maximum to save processing time. Figure 4.8 compares a standard process for neat resin to show the reduction in processing time. On the left, the smaller working width of 85 mm is shown, resulting in a processing time of 520 s for all steps per 100 g. The wider setting of 175 mm shows the same line force levels but reduced overall time with 260 s.

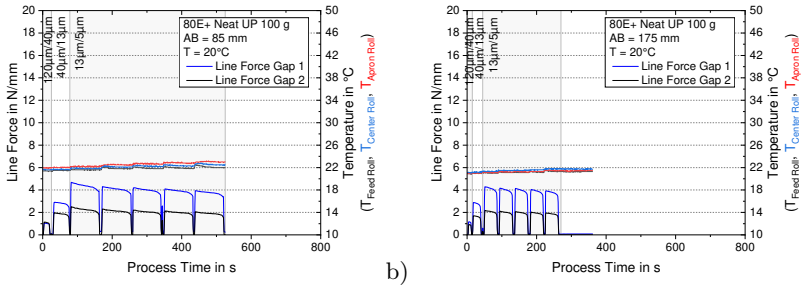

Figure 4.8: Line forces of neat UP resin for a standard 80E *Plus*$^+$ process at 20 °C for a) gap width $AB = 85$ mm and b) $AB = 175$ mm

4.1.3 Influence of the Roller Diameter

The roller diameter cannot be changed on the same machine. However, by changing from an 80E *Plus*$^+$ TRM to the larger model 120E-250 an increase of roller diameter from 80 mm by 50 % to 120 mm can be investigated with regard

to changes in measured line forces. Figure 4.9 compares the standard process for neat resin and the masterbatch with a larger roller diameter. Firstly, a reduced value of average line force per step can be observed for gap 1.

In a direct comparison of processing neat UP resin in Figure 4.8a) on the 80E *Plus*$^+$ and in Figure 4.9a) on the 120E the reduction of line forces in gap 1 to a level measured in gap 2 can be observed. For the smaller roller diameter, the line force of the feeding gap was usually twice as high. On the other hand, the overall processing time for 100 g material has increased on the 120E by 20 %.

For the masterbatch, a similar shape of the line force signal can be observed on both machines in Figure 4.9b). In the first dispersion steps a separation peak towards the end of each step can be seen which vanishes in steps 6 and 7. The measured values for gaps 1 and 2 show a difference with line forces being 50 % higher in gap 1. The total processing time for the masterbatch is shorter in comparison to neat resin by the same settings. In comparison to the smaller roller diameter a reduction of total processing time by 20 % can be observed.

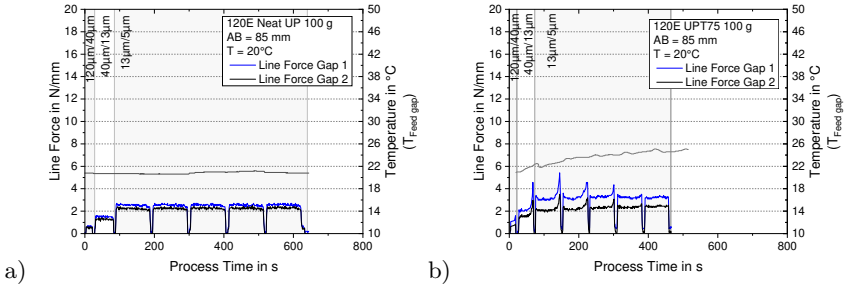

Figure 4.9: Line forces for standard processes on a 120E-250 TRM at 20 °C with working width $AB = 85$ mm for a) neat UP and b) UPT75

4.1.4 Influence of the Filling Height in the Feeding Gap

Another influence that was expected to make a difference in the process stability is the filling height in the feeding gap. The filling height influences the vortex formation in the feeding gap. In Figure 4.10 the three different levels *Low, Middle* and *High* are depicted with reference to the side-guards and as photographs for neat UP and UPT75 masterbatch. The lowest level was chosen to form the minimum possible vortex in the feeding gap. The middle level represents a state where the material height is approximately half the roller diameter and

the highest level is slightly above the roller diameter to create a round material vortex within the feeding gap.

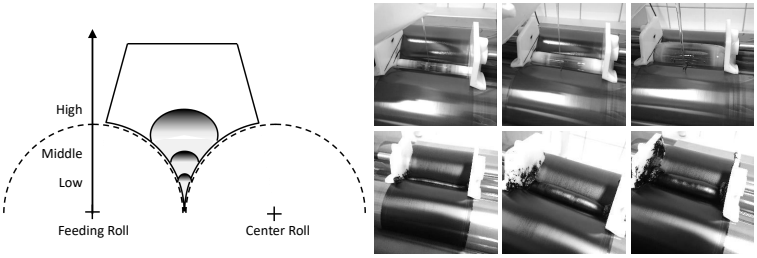

Figure 4.10: Schematic depiction and photographs of the filling height and vortex variation

Starting with neat UP resin, Figure 4.11 shows the line forces for gap 1 and gap 2 with varying filling heights. A higher line force by 20 % can be observed with low vortex height in both gaps which is attributed to a visually more turbulent flow. More air is introduced into the resin as seen on the top right in Figure 4.10. The total processing time is in the same range showing no significant dependence on the vortex height.

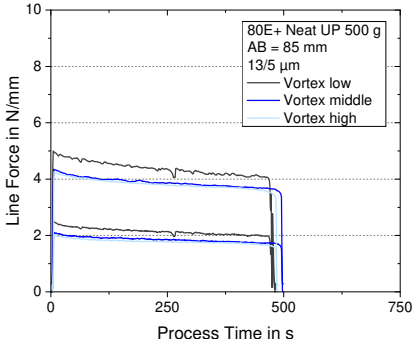

Figure 4.11: Vortex variation for neat UP resin on a 80E *Plus*$^{+}$

Processing of the masterbatch UPT75 with 1 wt% Tuball 75 is shown in Figure 4.12 with vortex variation in two different repetitions. Both time 500 g of fully dispersed material was used to observe the line force and processing time. As can be seen, the results are totally contradictory. In the first experiment in Diagram

4.12a) the highest vortex leads to the highest line forces. In diagram 4.12b) the lowest vortex causes unstable line forces on the highest level compared to the higher vortexes. The processing time is similar in both cases. Therefore, a general dependence of line force on vortex height can not be stated.

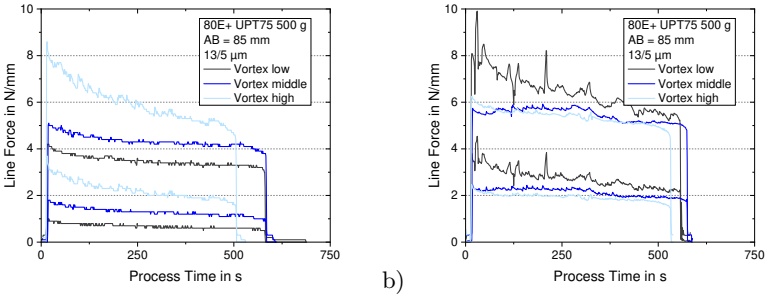

Figure 4.12: Line forces of UPT75 on the 80E *Plus*$^+$ with $AB = 85\,\text{mm}$ in a) the first vortex height variation and b) the second repetition

For a wider gap width of 175 mm Figure 4.13a) shows the decreased line forces and reduced total processing time independent of vortex height. In Figure 4.13b), the influence of vortex variation on a larger three-roll mill with 120 mm roller diameter is shown. The gap width is narrow with 85 mm. The increased roller diameter significantly decreases the processing time as well as line force. It can also be noted that the difference between gaps 1 and 2 is reduced.

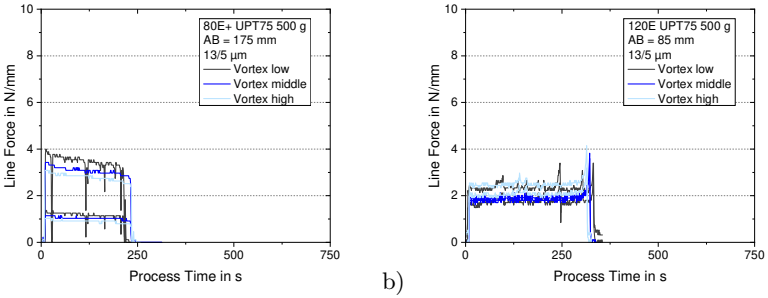

Figure 4.13: Filling height dependent line forces of UPT75 on a) the 80E *Plus*$^+$ with $AB = 175\,\text{mm}$ and b) the 120E with $AB = 85\,\text{mm}$

Overall, no clear dependence of resulting line forces or processing time on vortex height in the feeding gap can be concluded. The stability of the signal can be

influenced easily by feeding flow because the introduction of new material into the gap can change the vortex flow and thereby have an impact on the measured line force.

4.2 TRM Integrated Impedance Measurements

Research Question

Can the dispersion state be assessed by in-line impedance measurements and what are its limitations?

Within the project 'SCALE - Nano2Industry' impedance measurement was chosen to be the complementary in-line monitoring method in addition to the line forces. The start-up SYSCribe was the technology partner for this task specializing in small measuring devices tailored for on-site monitoring applications. Figure 4.14 shows a schematic overview of the measuring set-up to evaluate temperature, line forces and complex impedance over process time. Since EXAKT already provides the in-line monitoring of line forces and roller temperature, a separate measuring system was developed for getting time continuous impedance values. An Ethernet serial hub connects both systems of an interface to collect all data in measuring software on a PC. This solution was worked out including all partners. It combines all existing systems while opening the possibility to implement data processing tools within the software. The measuring PC can be placed remotely from the production line enabling flexible monitoring outside the safety precautions of a lab environment.

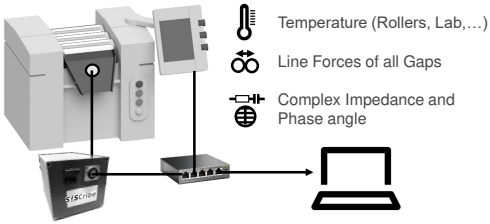

Figure 4.14: Schematic overview on the in-line monitoring tool

Figure 4.15 shows the theoretically expected in-line monitoring signals of line force and complex impedance for the batch process schematically. Over the

processing time, a characteristic line force signal can be observed for all dispersion steps (blue and grey), stabilizing towards the last steps. The complex impedance (black) will show a time shift depending on the electrode's position since the measurement cannot be conducted within the rollers' gaps. Therefore, a shift of the signal by Δt must be observed. In contrast to measuring a broad frequency range all the time, measuring only certain frequencies will reduce measuring time significantly.

Several pre-experiments concerning the frequency selection have been conducted and 20 kHz has been found to be the most suitable. Over the processing steps the conductive CNP network will form within the dispersion decreasing the overall measured impedance in later steps. A final complex impedance level of the fully formed conducting network will be reached after a certain amount of steps. In this case, the minimum impedance is shown after step 4. Between steps, a clearance of the electrode to the empty signal is assumed. In reality, this is only possible when the material flows over the electrodes without any residue, which might only be achieved by cleaning them between steps.

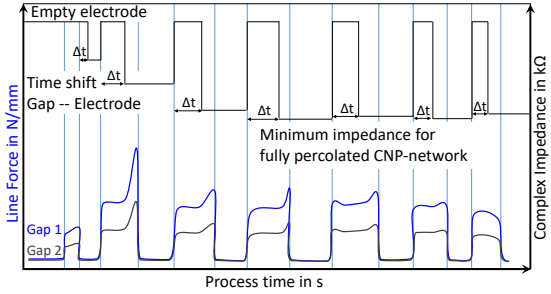

Figure 4.15: Schematic signals for in-line monitoring of line forces and complex impedance

To implement impedance measurement, an electrode had to be designed, tested and integrated on a TRM. Preliminary tests with screen-printed meander structured electrodes on 100 µm-scale, as well as large copper strip electrodes on the centimeter scale, have been proven to not be sufficient (SCALE - Nano2Industry 2020). Thus, a trade-off design regarding scale and manufacturing limits had to be found. Figure 4.16 shows the final electrode as a CAD design. The placement was chosen to be in the material stream on the TRM apron so that the dispersed material can be characterized. The position was carefully chosen to be

placed so that every apron could be modified with electrodes by a milled fitted recess (see appendix C, Figure A.3). This way the apron construction, structural integrity and functionality are not compromised and the electrodes can be contacted from the back. For a prototype, three electrodes have been mounted in the TRM apron. The detailed view of the electrodes CAD model on the right show the fitted electrode socket in green, which holds the interdigitated electrode fingers (orange and grey) as well as the temperature sensor PT100 (blue) in the center of the electrode. The interdigitated electrodes have a width of 1 mm and a distance to each other of 0.5 mm. The electrode halves and the temperature sensor are embedded in an insulating resin cotton flake mixture. All contacts in the back are connected to a flat ribbon cable that can be connected to the measuring system.

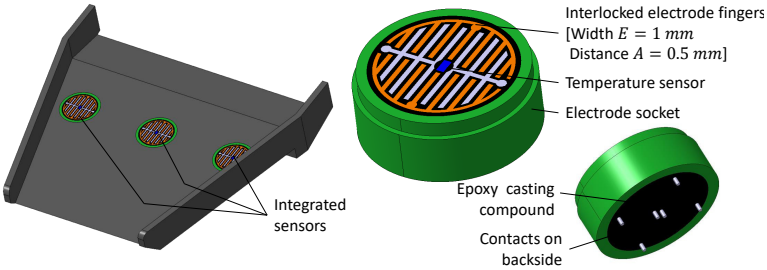

Figure 4.16: CAD model of electrode design

Figure 4.17 shows the electrodes integrated into the 80E Plus^{+} apron on the left as well as a detailed view of the electrode surface on the right without material and covered with a 0.02 wt% T75 UP dispersion. As described before, the positioning could be achieved by milled sockets for all electrodes. Since the shown set-up is a prototype, the TRM apron is not PTFE-coated as for the standard part. This might affect the running time of material down the apron, but with processed batch sizes no significant differences between the two aprons could not be measured.

Figure 4.17: Integrated electrodes on TRM

The software developed within the project SCALE - Nano2Industry allows one to create data banks for storing dispersion processes. Within a data bank, the machine set-up is defined to connect data streams from all involved three-roll mills and impedance measurement devices. Different materials can be created, depending on what is dispersed in the process. On the lowest level of the database structure, the process name or batch can be defined to save several processes of the same configuration within the same data bank. To start the measurement, the predefined devices can be coupled to the measuring computer and the measurement can be started. Statistics about the three-roll mill like roll configuration or firmware version are displayed as well as the live data from the current dispersion process. Rotational Speed, temperatures, gap spacing and line forces are plotted continuously over time. From the SYSCribe impedance measuring box the complex impedance for selected frequencies is displayed. After finishing the recording data can be exported with or without statistics as a CSV-file.

4.2.1 Off-Line Validation of the Impedance Spectroscopy Tool

To understand the impedance response of stationary material on the electrode, several off-line validations have been done to characterize the measuring system.

Firstly, the electrode coverage is investigated with masterbatch UPT75. Figure 4.18 shows the complex impedance measured at 20 kHz for different percentages of areal coverage. This is achieved by scraping a defined thickness of 3 mm onto the electrode with contact with a certain amount of electrode fingers at a time. From empty electrode to full-coverage the impedance decreases rapidly by contacting only the first electrode fingers. Redundant pathways by covering a higher areal percentage do not decrease the impedance significantly. As a dashed

reference line, the response of neat UP resin is added to the plot, showing a slightly lower impedance than the empty electrode.

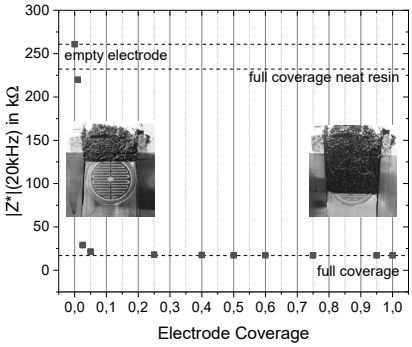

Figure 4.18: Complex Impedance in dependence of the electrode areal coverage

Especially high-viscous material tends to fold after leaving the rollers by the apron blade. Subsequently, distance between material and electrode has been quantified by measuring the complex impedance for an UPT75 material disk spaced with a certain gap to the electrode. Figure 4.19 shows that detection of material is possible up to a distance of 0.35 mm which is in good agreement with the penetration depth of interdigitated electrode designs as discussed in chapter 2.1.1. The penetration depth of the electric field above the electrode is thus limited and prevents disturbance of the in-line measurement by anything but the material running down the apron.

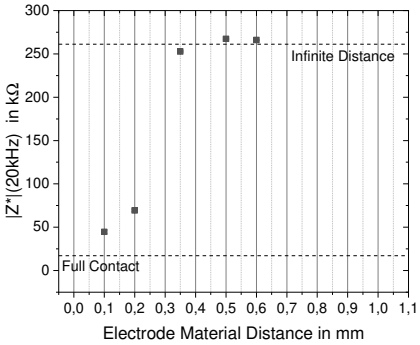

Figure 4.19: Complex Impedance in dependence of vertical distance between material and electrode

Figure 4.20 shows the dependence of measured impedance on filler content of SWCNT in the UP base resin. From neat resin to 0.3 wt% filler content the measured impedance decreases asymptotically towards the minimum impedance measured for the 1 wt% UPT75 masterbatch. Therefore, concentration differences can not be distinguished significantly.

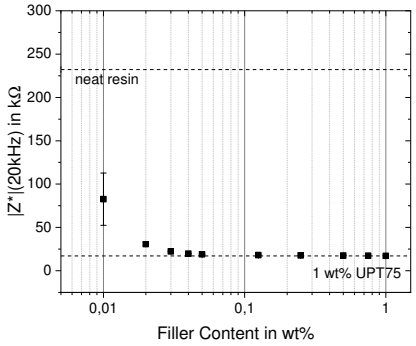

Figure 4.20: Complex Impedance in dependence of filler content

Lastly, the influence of material layer thickness on the electrode was investigated with varying filler content. The masterbatch with 1 wt% filler content shows no difference from minimum layer thickness of 10 µm to 300 µm. The filler content has to be reduced to 0.02 wt% or 0.01 wt% to show a thickness dependent behavior. For these low filler contents the impedance decays rapidly until 1 mm material thickness is reached. Therefore, a conductive pathway of SWCNT in the contacting layer closest to the electrode is enough to shield all material above. This occurs with less material thickness for higher filler loading. [22, 25, 26]

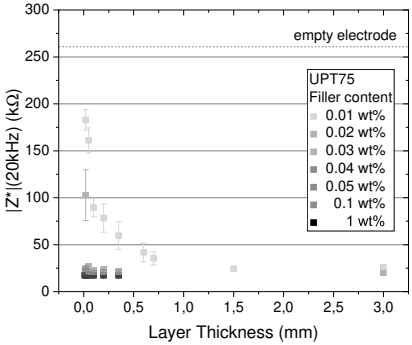

Figure 4.21: Complex impedance in dependence of layer thickness on the electrode for different filler contents

4.2.2 In-Line Monitoring Validation with Relevant Material Systems

To investigate and validate the in-line monitoring, different dispersions of CNP in 200 g UP base resin are presented. To elaborate on the influence of filler morphology, carbon black, few-layer graphene, single- and multi-walled carbon nanotubes are dispersed with varying filler content chosen around the percolation threshold according to measurements from [2]. In the following sections, the graphs of line forces and complex impedance are discussed to correlate the dispersion state to the in-line monitoring signals. The time-continuous measurement is presented with line forces and measured impedance. Additionally, statistic values per step are shown to discuss the extracted feature values.

For each dispersion step a Python script calculates the start and end time of the step and corresponding step time. For the line forces mean values LF_{mean} per step are calculated. The maximum line force LF_{max} is determined and is used to calculate a so-called separation factor SF:

$$SF = \frac{LF_{\mathrm{max}}}{LF_{\mathrm{mean}}} \tag{4.1}$$

This factor was defined to quantify the relative peak height of a separation peak compared to the average line force value of the respective step. For the measured impedance it has been found that the minimum measured value per step is a representative measure to assess the dispersion state. Thus, the impedance minimum $|Z^*|_{\mathrm{min}}$ is shown per step as well.

Since a larger set of filler content and particle type has been investigated, not all are presented in this chapter. Only important comparisons are discussed to deduct answers to the research question. The full set of experiments can be found in Appendix A.2.

In-Line Monitoring of Carbon Black Dispersions

Starting with globular particles, three different filler contents of carbon Black Printex L have been dispersed and monitored. Figure 4.22 shows monitoring signals and statistics for 4 wt% Printex L. The line forces (blue and dark grey) are low, showing stable behavior without any separations over all dispersion steps. This is in accordance with the observations during processing, whereby the particles are uniformly mixed into the resin after the first step already. In Figure 4.22b) this is reflected by an almost constant level of the mean line forces on a low level and separation factors close to 1. The time per step increases with each decrease of the gap spacing until it is constant for steps 3 to 7 as well. The complex impedance (black) decreases from first to second dispersion step and is stable for all following steps. The complex impedance decreases continuously within every step and stays at a minimum value over time, the development over the steps in the right diagram represents that as well. The phase shift is depicted in light grey as well showing similar behavior to the complex impedance. The phase angle values have no realistic value in the expected range of −90–0°. Calibration of the measuring system to depict absolute values could not be done within thesis time but would be a good addition for future works. Since values and relative changes have not been consistent, the discussion of phase shift will be excluded from this thesis.

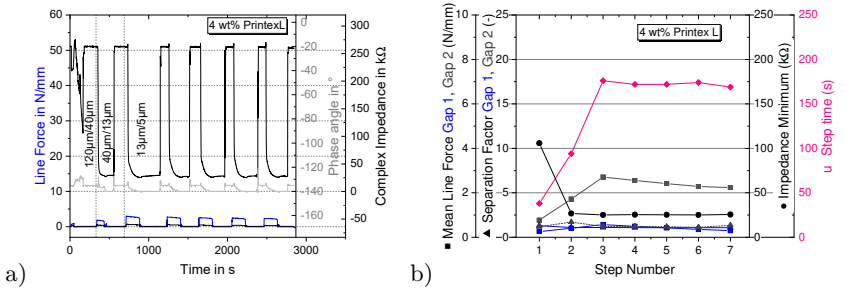

Figure 4.22: a) In-line monitoring signals and b) statistics of 4 wt% Printex L in UP

For different filler content, the statistics per step are depicted in Figure 4.23. The mean line force value increases by doubling the filler content to 8 wt% and slightly in the last dispersion steps for 12 wt%. The overall development of the mean line force and minimum impedance over steps is similar. With increased filler content the initial minimum impedance in step 1 is smaller. For 8 wt% and 12 wt% no significant differences can be detected from step 2 on. The absolute value is on the lower measurement limit of the impedance module.

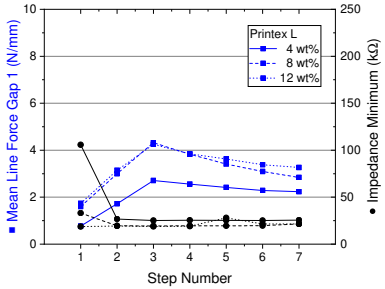

Figure 4.23: Comparison of mean line force in gap 1 and minimum measured impedance per step for all Printex L filler contents

In conclusion, the in-line monitoring works well for masterbatches with globular particles like carbon black. Line forces indicate immediate separation of agglomerates without resin-particle separation. The complex impedance measurement indicates good wetting behavior with optimal electrode contacting resulting in stable measurements over time. The conductive dispersion shows constant minimum impedance values.

In-Line Monitoring of Few-Layer Graphene Dispersions

Next, planar few-layer graphene is discussed regarding in-line signals and statistics. In comparison to globular carbon black, the measured impedance values are significantly higher indicating either lower conductivity or less ideal wetting and contacting behavior. The minimum overall value for 0.5 wt% AVAN2 in UP resin is reached in step 3, where a small separation towards the end of the step can be observed in the line force signal as well (compare Fig. A.5). This is typical for process steps wherein some particles remain on the rollers or feeding gap towards the very end. The separation peak due to the high concentration residual can be seen in Fig. 4.24a), and the drop in impedance is obvious in Fig.

4.24b). All other steps show stable dispersion behavior and a constant minimum complex impedance value.

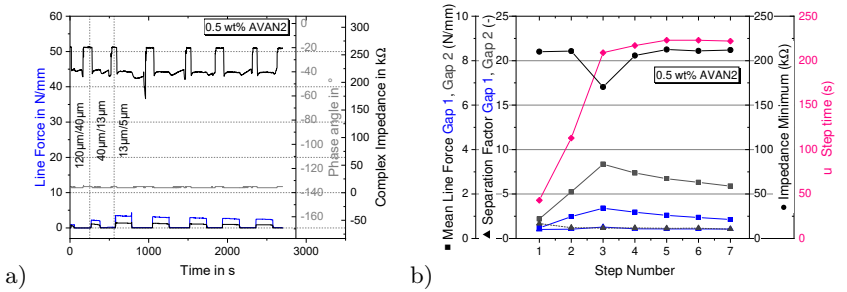

Figure 4.24: a) In-line monitoring signals and b) statistics of 0.5 wt% AVAN2 in UP

Increasing the filler content does not change the mean line force values per step significantly, as can be seen in Figure 4.25. Only in the last two dispersion steps the viscosity increase with increasing filler content results in a slight increase in the line force value. For the minimum impedance values, a differentiation between filler content is possible. The reduced value per step indicates higher electrical conductivity with higher filler content. For all processes, the lowest overall impedance is measured in step 3, when the minimum gap spacing is set for the first time and the separation towards the end of the step could be observed in Figure 4.24a).

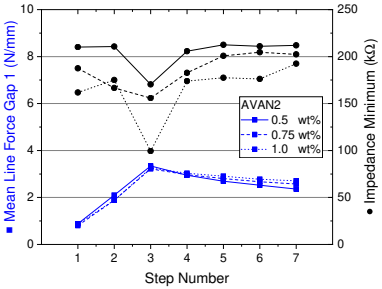

Figure 4.25: Comparison of mean line force in gap 1 and minimum measured impedance per step for all AVAN2 filler contents

Overall, the planar particles show a distinguishable different behavior compared to globular carbon black in the complex impedance measurement. Two local minima per dispersion step mark the initial coverage of the electrode and the residual material film. Also, the high impedance values of typical filler content allow to distinguish them by the absolute measured value.

In-Line Monitoring of MWCNT Dispersions

MWCNT have shown distinct dispersion behavior in previous off-line characterizations. The build-up of a particle network can be observed by the continuous decrease of the complex impedance. Firstly, Figure 4.26a) shows lowest filler content of 0.1 wt%, which is stable in dispersion and shows no separation in the line force signal. In Figure 4.26b) the development of increasing mean line force with decreasing gap spacing is visible. Over the further steps, the particles are separated more, reducing the line force again. The complex impedance starts with highest values in the first step. Within every step there are two minima again, one for the initial coverage and the second where the residual material film flow slows down until only a thin layer is left. The minimum impedance value decreases until step 5, which is in good accordance with the offline characterization, which states the final dispersion is reached in step 5.

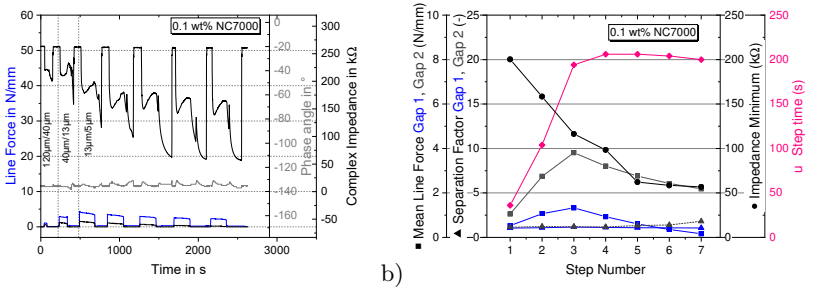

Figure 4.26: a) In-line monitoring signals and b) statistics of 0.1 wt% NC7000 in UP

The step statistics in Figure 4.27 reveal the transition of the percolation threshold for the MWCNT. Whereas 0.1 wt% show a significant decrease of minimum impedance until step 5, the higher filler content of 0.3 wt% and 0.5 wt% reach their minimum in step 3 already, since the filler loading is above the percolation

threshold. Mean line forces show similar behavior of 0.3 wt% and 0.5 wt% and an unexplained higher value for lower filler content of 0.1 wt%.

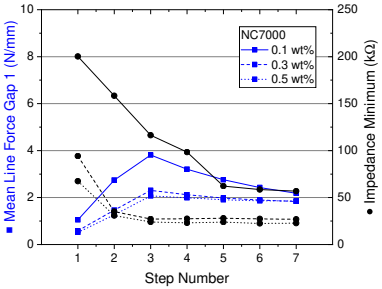

Figure 4.27: Comparison of mean line force in gap 1 and minimum measured impedance per step for all NC7000 filler contents

Summarizing, MWCNT show slight separation when the gap spacing is decreased over the first three steps, but further processing shows signals of a stable process. The minimum complex impedance values show a decrease reaching the lowest value in step 3 already. Higher viscosity of a higher filler content speed up the processing time at lowest gap spacing for steps 3 to 7.

In-Line Monitoring of SWCNT Dispersions

Finally, SWCNT shall be discussed concerning their monitoring signals. From offline measurements, a full particle network is expected to be formed first after several steps on the lowest gap spacing. On the other hand, it is expected to be possible to achieve lowest impedance values for filler contents of one order of magnitude lower than MWCNT.

Figure 4.28 shows the reduced statistics for lowest filler contents between 0.01 wt% and 0.05 wt%. The mean line force development over the steps is similar for all. The impedance measurement on the other hand varies strongly. In the first steps no clear dependence on filler content can be deducted. In the last four steps on the other hand, the measured minimum impedance decreases with increasing filler content as expected.

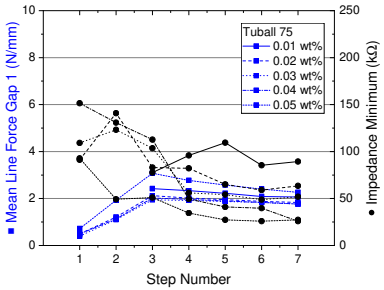

Figure 4.28: Comparison of mean line force in gap 1 and minimum measured impedance per step for low filler contents of Tuball 75

In Figure 4.29 the lowest complex impedance value is expected to be observed after fully processing the material, since 0.05 wt% Tuball 75 are processed in the resin. Two identical processes under the same lab conditions are presented in Figures 4.29a) and 4.29b) from different days. In the first process depicted in Figure 4.29a) impedance values higher than for the empty electrode occurred during steady material flow. In the repetition experiment in Figure 4.29b) this phenomenon is not visible anymore. The measured impedance rises significantly when material is flowing over the electrode, but does not overshoot the empty electrode level. It seems to be an artifact of the measuring device because an empty electrode should yield the highest impedance.

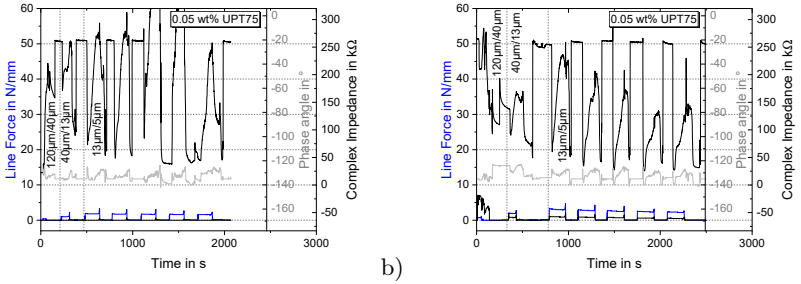

a) b)

Figure 4.29: In-line monitoring signals of two batches 0.05 wt% Tuball 75

The statistics of each of the 0.05 wt% Tuball 75 dispersion processes are summarized in Figure 4.30. The mean line forces as well as the processing time per step of the second process depicted on the right are higher overall. The final

minimum impedance measured in steps 4 to 7 is lower than in the first process. Therefore, it has to be considered that every process varies slightly concerning the in-line monitoring signals. The variety of influencing parameters can not be fixed every time.

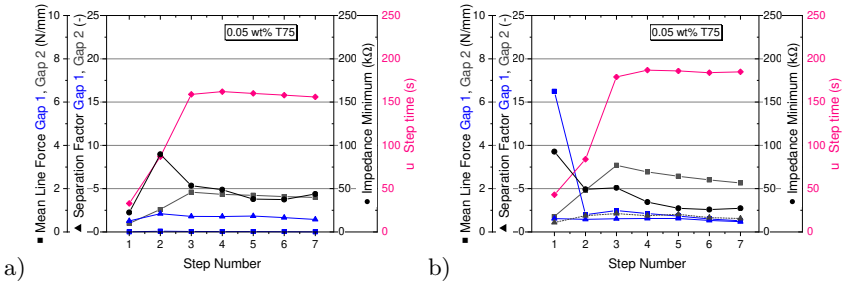

Figure 4.30: In-line monitoring statistics of two batches 0.05 wt% Tuball 75 in UP

Low filler content as discussed previously is usually achieved by diluting a masterbatch of higher concentration. Therefore, the final two filler contents to be discussed are 0.1 wt% and the 1 wt% masterbatch, which was the main goal of the research project previously described in the introduction to this chapter. Figure 4.31 shows the statistics from 0.01 wt% up to 1 wt%. A general increase in mean line force with higher filler content can be seen. For the minimum impedance, the lower boundary of the measurement system limits a distinction of filler contents above 0.05 wt%. The lowest minimum impedance can be observed for the 1 wt% masterbatch from the first step on.

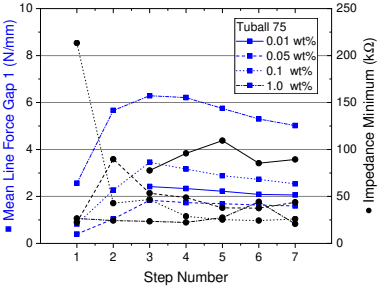

Figure 4.31: Comparison of mean line force in gap 1 and minimum measured impedance per step for filler contents of Tuball 75 up to the masterbatch

For the highest filler loading of a 1 wt% Tuball 75 masterbatch highest line forces and most severe separations in the first steps are observed. Figure 4.32 compares two processes of the masterbatch, which were run using identical material and machine settings. Nonetheless, the processes showed drastically different behavior of the material on the apron. On the left side, the material running down the apron over the electrode showed a lot of buckling and therefore unsteady flow. This results in severe fluctuation in the measured impedance signal. At the end of the process, the line forces and offline characterizations indicated a fully dispersed material identical to the second process on the right. That dispersion process showed minimum material buckling contrarily. Stronger separation in the first 3 steps is reflected in more fluctuation of the impedance between the two minima per step. But the final 4 steps show way more stable measured values for the impedance similar to carbon black dispersions. Only the last steps signal fluctuates a bit more because the viscosity increase by the dispersed SWCNT network leads to more buckling and thus less ideal contacting of the electrode.

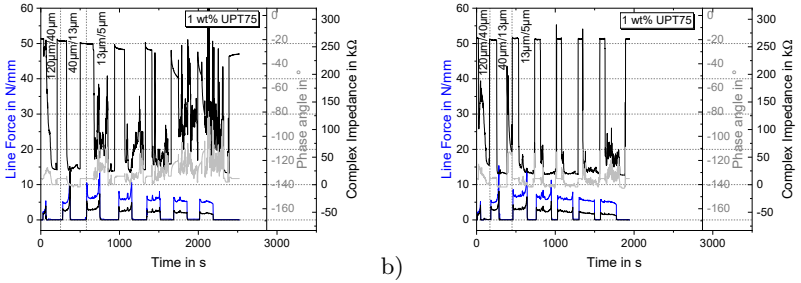

Figure 4.32: Representative in-line monitoring signals of 1 wt% Tuball 75 in UP for a) severe and b) minimum material buckling

However, extracting the feature values for each step from the in-line monitoring signals shows quite a similar behavior for the masterbatch processes. Minimum impedance values per step develop similarly as well as mean line force values. In processing time, the second more stable process takes longer in the final steps with minimum gap spacing.

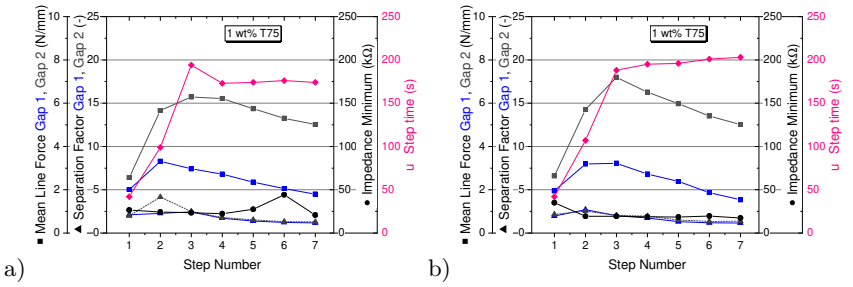

Figure 4.33: In-line monitoring statistics of two batches 1 wt% Tuball 75 in UP with a) severe and b) minimum material buckling

Overall, the in-line monitoring of SWCNT dispersions showed some anomalies compared to other CNP morphology. Especially the measurement of an impedance in the flowing state creates a variety of artifacts like unexplained high impedance values when resin-rich material flows over the electrode. Nonetheless, within each step the defined feature values seem to be a good quality measure for masterbatch processes despite different physical behavior of the material on the apron.

Summary on In-Line Monitoring Capability of Different CNP Dispersions

Similar to the graphical summary of influence factors on the line force in Figure 4.1, following Figure 4.34 shows how the measured impedance can be influenced. Starting from the empty electrode impedance the measured value is reduced as soon as the electrode is contacted by CNP dispersion. Depending on the filler content, the measured impedance can be decreased to a minimum. Over time the flow characteristics influence the measured impedance value significantly. A constant flow velocity can increase the measured value leading to a local maximum in the graph over time. Towards the end of a step, when the material flow decreases and leaves a film of steady material on the electrode, a second local minimum is observed for most processes. Buckling of high-viscosity material or included air can result in peaks of higher impedance over time. For masterbatches, this material behavior on the electrode can influence the quality of the measured signal significantly. By cleaning the electrode the empty electrode reference impedance can be reached again in the end of a step.

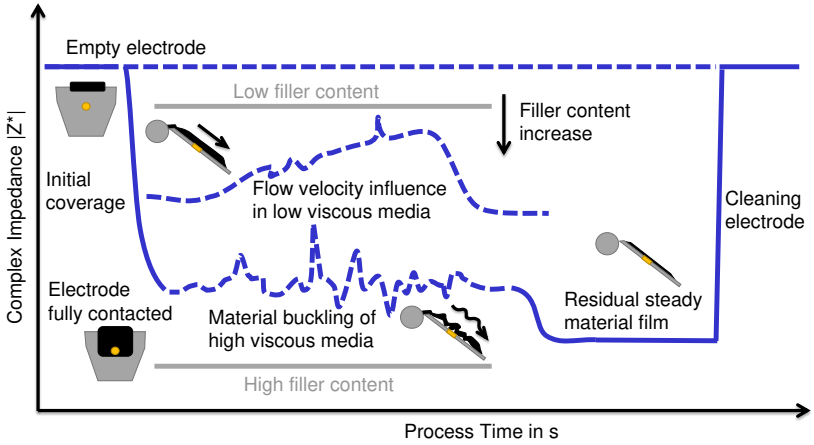

Figure 4.34: Schematic overview of influence factors for in-line impedance measurements

Figure 4.35 gives the graphical summary of impedance characteristics over time in dependence on the filler particle morphology. Highest impedance (magenta) is measured for few-layer graphene dispersions. A local minimum for the initial wetting of the electrode and the residual steady material film can be observed

separated by a local maximum of steady flow. For CNT dispersions the viscosity is defining the signal form. Low viscosity dispersions (yellow) with overall stable processing behavior show similar behavior as FLGs but with lower absolute impedance. With increasing filler content lower impedance is measured for CNT (black). However, the material is also prone to unstable behavior like buckling or separation leading to low signal-to-noise ratio. Globular carbon black (blue) shows the best wetting behavior on the electrode with lowest measured impedance and a stable value over time.

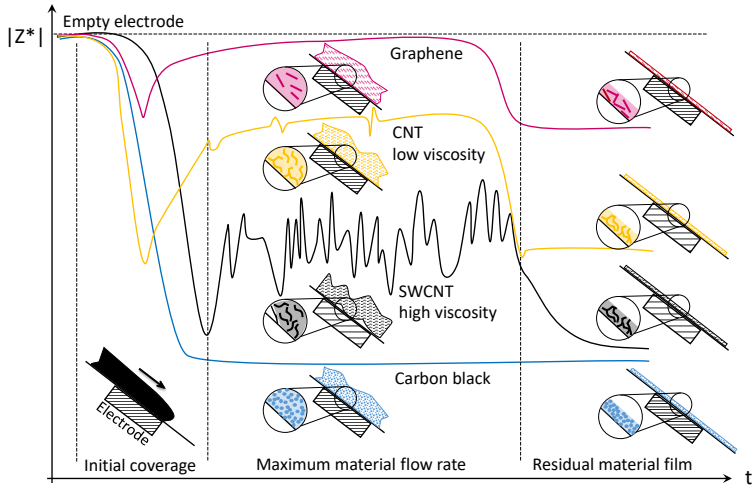

Figure 4.35: Schematic summary of signal characteristics for different filler morphology in impedance measurements

In Figure 4.36 all final dispersions from the CNP type and filler content variation are measured offline with the impedance monitoring tool and the off-line reference hp source meter to compare the complex impedance levels. Overall, the decreasing complex impedance with increasing filler content can be seen. But the limitations regarding low impedance measurements are obvious for the in-line device, the lower range of the integrated impedance module is limited compared to the off-line hp source meter. In addition to a lower measurement boundary, the change of electrode type has to be addressed. Off-line measurements are done with cylinder electrodes in a parallel plate capacitor set-up, where the electric field scans a large sample volume. For the interdigitated flat electrode of in-line monitoring shielding effects dominate the response as has been

shown in the thickness variations. Compared to the cylinder electrode a smaller sample volume is scanned. The smaller volume makes the measurement more prone to imperfect networks between each of the electrode fingers. On the other hand, multiple interdigitated electrode fingers increase the possibility that some of them are connected by a perfect CNT network with the highest possible conductivity. As the experiments for incomplete areal coverage have shown, those few connections are enough to yield the lowest measurable impedance values. Thus, the measurement boundary of the system is the limiting factor for the low-impedance range. Overall, the relative changes and development over time can be gained from in-line monitoring with the implemented system.

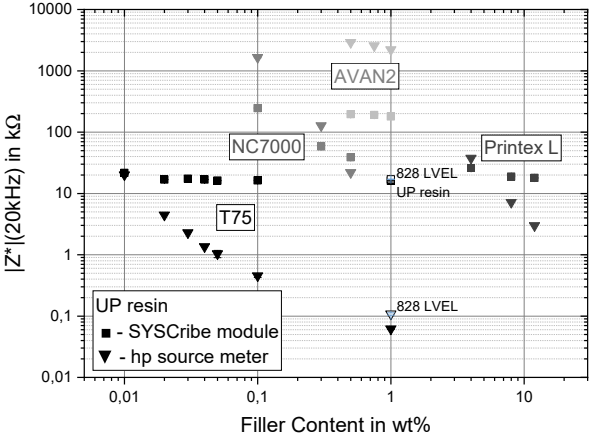

Figure 4.36: Complex impedance in dependence on filler content for different CNPs of the integrated impedance module and the offline impedance spectrometer

Figure 4.37 shows the full off-line reference impedance spectra over frequency for all measured configurations. The 20 kHz line marks the measuring frequency that was used to depict the time-dependent development of the impedance of the integrated module. It can be seen that the qualitative levels of impedance that are distinguished in relation to each other in Figure 4.35 are in good accordance with the relative differences gained from the off-line measurements.

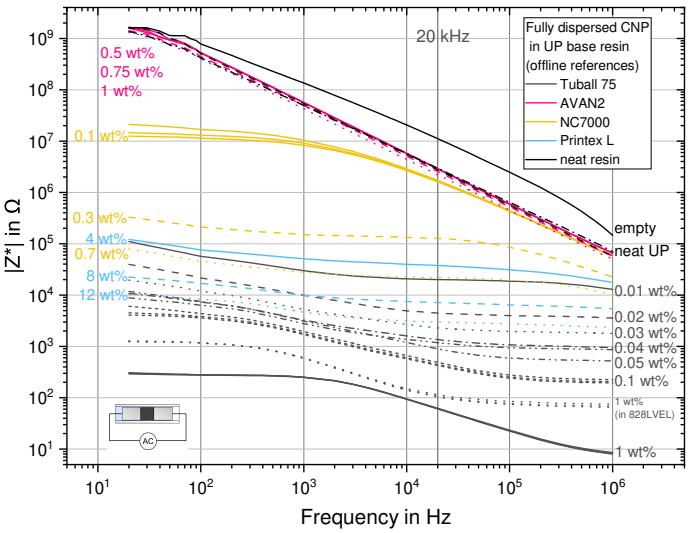

Figure 4.37: Complex impedance over frequency for all tested filler contents and particle type measured with the offline impedance spectrometer

4.3 Process Outlook and Conclusion

This final section describes the up-scaling approach of the BMBF-funded research project SCALE - Nano2Industry. The TRM dispersion process needs to be up-scaled from smaller lab batches to a ton-scale continuous production that yields an economic and time-effective output of nano-intermediates. This approach aims to incorporate the production of masterbatches in-house to cut off external suppliers and accompanying dependencies. A production line based on the previously gained knowledge in process stability and integrated monitoring methods was conceptualized. Pre-experiments have been conducted throughout the research project. However, building and testing a prototype production line was not possible within the project. Working with carbon nanoparticles is mostly unregulated on a large-scale, and approval by the respective authorities came out to be difficult in Germany. The risk assessment is ongoing, so there are no fixed official regulations considering which production lines could be set up. At the same time, supplying manufacturers are able to improve their long-running masterbatch processes resulting in lower costs. A manufacturer for coating applications keeps supplier contracts in this case and can not try to start their in-house production for economic reasons. Additionally, the de-

mands of the markets are changing, which makes building up a new production line with new technology even more time crucial and demands clear regulatory circumstances.

Figure 4.38 shows the idea for a cascade process, wherein a continuous masterbatch production in ton-quantity was planned. The initial pre-mixing of resin and particles has to be conducted in a safe closed-lab environment. The pre-mix has to properly incorporate all dry particles in resin, so they are not a risk on the following production line of TRMs.

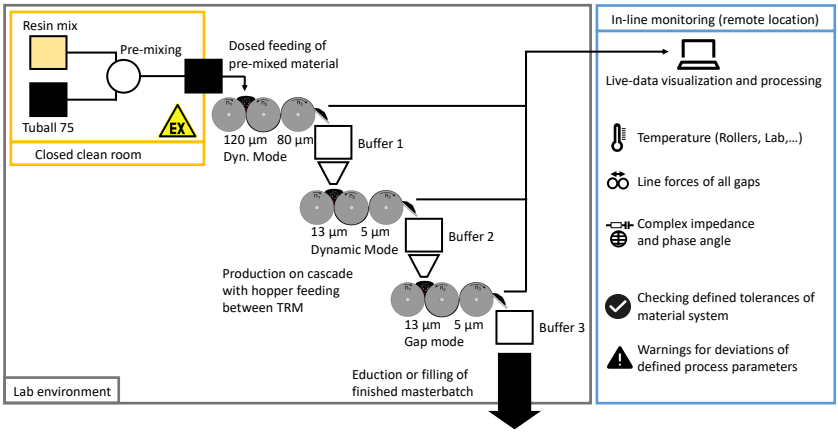

Figure 4.38: Process concept for masterbatch production

The production line is set up as a continuous cascade process with a minimum number of TRMs. Within the project SCALE - Nano2Industry no more than three machines were economically favorable, so the processing has to be tailored to the particle type and filler content accordingly. For the Tuball 75 masterbatch it was a challenge to form the dispersion within 3 steps. From the in-line monitoring signals discussed before it was obvious that within the three first steps of the standard process, no full dispersion can be achieved. Thus, the gap spacing has to be altered. In the first step, homogenization is still necessary. To stabilize the process and avoid separation of the material a 'dynamic mode' is chosen, whereby the line force is kept on a constant level by changing the gap spacing accordingly. Upcoming separation of material leads to an increase in line force due to higher viscosity. To prevent that from happening the gap spacing

is opened temporarily to increase the transport of resin. This way, a homogeneous material flow from the first apron shall be achieved. On the second TRM the agglomerates in the homogenized material have to be separated. Again, a dynamic mode is chosen to prevent separation but the second TRM is set to minimum gap spacing of 13 µm and 5 µm as the default setting. The last TRM is set to fixed smallest gap spacing to eliminate all remaining agglomerates.

From several tests with smaller experiments in the kilogram range the transportation modes of material between TRMs have been investigated. A funnel placed above the feeding gap is sufficient to feed even high-viscous masterbatches to the next machine. A buffer between the TRMs ensures that the production run can be stopped in case of problems without interrupting the whole line.

The process control and in-line monitoring can be observed remotely from the production line, as demonstrated in the previous chapters. The signals from all characterization tools can be monitored, for each process parameter windows defining the desired material properties can be set to check the quality.

A last parameter that can increase production volume besides gap spacing, working width and roller diameter is the rotational speed. The flow rate in kilogram per hour over rotational speed of the apron roller is depicted in Figure 4.39. For each of the standard gap spacing settings 500 g fully processed masterbatch UPT75 or the neat UP resin was run on the 80E *Plus*$^+$ or on the 120E-250. The total processing time is measured to calculate the mass flow rate for each rotational speed. A model for an ideal flow between two rollers is given in [117] as

$$\dot{V} = ((n_1 \cdot h) + \frac{1}{2} \cdot h \cdot (n_2 - n_1)) \cdot AB \tag{4.2}$$

with roller speed n_1, n_2 of two neighboring rollers with gap spacing h in between. In addition to the measured flow, a minimum and maximum reference line is depicted in Figure 4.39 for the minimum spacing of 5 µm and a maximum of 45 µm. Since the machine stiffness of the TRM is not ideal, the gaps can widen according to the stiffness in response to the line forces. On the other hand friction and nonlaminar flow might also influence the flow rate. For smallest gap spacing the influence of roller diameter can be seen showing higher rates for the 120E-250 TRM. Also, the higher viscosity of the masterbatch seems to be favorable to increasing flow rate. Especially for gap spacing 40 µm/13 µm the difference between neat resin and masterbatch is high. Of course, the flow rate is highest in the homogenization gap setting with 120 µm/40 µm. The lower and upper limits are in good agreement with set gap spacings since the smaller gap always determines the maximum flow rate.

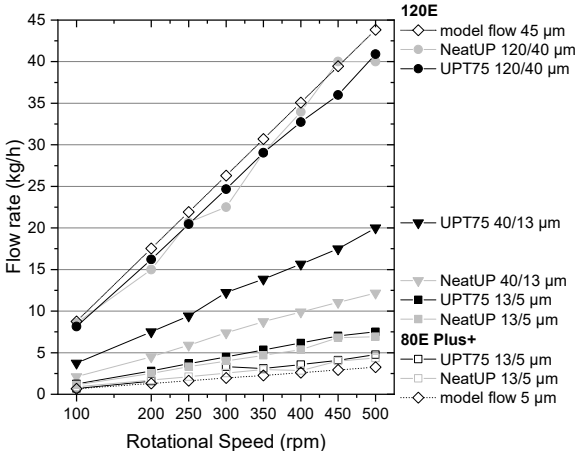

Figure 4.39: Flow rate dependence on TRM size, rotational roller speed and gap width for gap width $AB = 85\,\mu m$

Figure 4.39 shows the potential of increasing roller speed to achieve a time-efficient, economic dispersion process with maximum output. Depending on resin and filler content, the transportation properties via rollers have to be observed regarding slip-effects. Nonetheless, speeding up the process enables in-time large-scale production and thus reduces the bottleneck in nano-intermediate manufacturing.

Addressing the Research Questions

This chapter has shown that a combination of line force monitoring and impedance measurements can be integrated into the TRM. Using the tracking of line forces on the new generation of 80E $Plus^{+}$ TRM in combination with integrated electrodes on the apron and an impedance module has been combined as an in-line monitoring tool. The new software enables time-continuous visualization and recording of all signals. Different filler morphology, filler content, process stability and the overall dispersion state can be determined.

The different influence factors on the line force signals have been shown. Increasing viscosity and filler content or decreasing dispersion gap width and temperature lead to increasing line forces. The processing time is

increased for lower viscosity and smaller working width or gap spacing. Filling height and working width show no significant influence on processing time or line forces. Using larger roller diameters of a larger 120E-250 TRM or increasing the rotational speed increases productivity. For every new material, the line forces can be interpreted with regard to mentioned parameters to judge process stability and dispersion state to reduce process steps to a minimum.

The addition of a second in-line monitoring method gives insight into the changes in electrically conductive filler particle networks. In-line impedance measurement can be integrated into a TRM apron skirt by choosing a flat interdigitated electrode to assess the quality of a process without interfering with the dispersion. Choosing 20 kHz as the measuring frequency gave a time-continuous signal to monitor dispersion processes.

Different materials can be distinguished based on their in-line signals in absolute impedance value and signal form. The signal form is resulting from flow and wetting behavior of the electrode and the overall conductivity of the dispersion. The integrated impedance measurement was validated in off-line and in-line measurements for a wide set of carbon filler morphology and filler content. However, shielding effects and measurement capability of the implemented device cloud the low impedance regime in comparison to the previously employed off-line impedance measurements with a cylinder electrode. Here, in future improvement, the measuring quality can be extended.

Feature value extraction from the time-continuous signal has been proven to give reliable comparative measures. Mean line force as well as a separation factor, considering the maximum line forces, and the minimum impedance value within each step characterize the dispersion progress independent of signal-to-noise ratio, which can alter depending on process stability.

5 Magnetic Manipulation of CNP Dispersions

The second topic of this thesis explores the possibility of permanent magnetic manipulation of previously dispersed CNP resin mixtures. The intrinsic magnetic response of different CNP is hereby characterized.

In Figure 5.1 the concept idea behind this topic is outlined. For most mixing, dispersion or coating techniques a lower viscosity is more favorable to lower process forces. Therefore, the approach is to start with a low-filler content, low-viscosity system to create a homogeneous dispersion. Next, a permanent magnet is used to influence the particles within the matrix and create a gradient. Ideally, this manipulation would result in a surface with increased filler content, which is of advantage regarding anti-static properties, wetting behavior, moisture resistance or easy-to-clean applications and scratch resistance. These properties would be favorable for spray-painted coatings that need low processing viscosity.

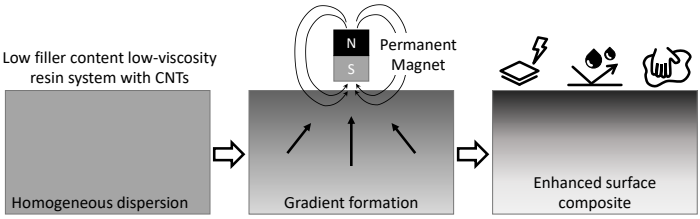

Figure 5.1: Idea concept of magnet-manipulated enhanced surface composites

Thus, the research question guiding this chapter is the following:

Research Question

Is it possible to manipulate CNP nanocomposites via permanent-magnetic field to achieve a filler content gradient?

It shall be noted that initial investigation approaches were done on nanocomposite plates and led to no network manipulation or non-reproducible results. An insight into those experiments can be found in Appendix B. Therefore, this chapter summarizes the second systematic approach to determine the limitations of permanent magnetic dispersion manipulation.

5.1 Magnetic Response of CNP in Low-viscous Media

Initially, the magnetic response of unmodified MWCNT was observed in solvents. To quantify different CNPs reactions following set-up was used to test the CNPs magnetic response. Figure 5.2 shows the closed-lid 10 mL glass bottle with a permanent magnet attached from the side. The magnetic field has been quantified regarding the field strength and is depicted as a heat map overlay showing the maximum field strength of 117 mT closest to the magnet. The field shows decreasing intensity within the bottle's volume.

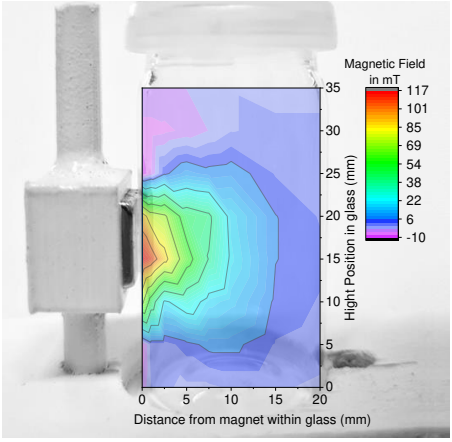

Figure 5.2: Test stand with single magnet for CNP in low-viscous media

In the beginning ethanol and water have been tested with 0.1 wt% CNP of the respective type. The particles are stirred into the solvent with a metal spatula for 1 min. The glass-bottle with moving particles is then placed in the test stand and the particles' reaction to the magnet is recorded. Figure 5.3 shows the representative response of all tested CNP types in ethanol. The first row shows the mixture state immediately after stirring at t =0 s. In all cases, the particles are randomly distributed within the liquid. For all CNP types a thin

layer of particles can be observed on the surface. These particles are either kept in stability by the surface tension because of small particle size and low weight or by low wettability of the particles and thus repulsion by the liquid.

After several seconds of observation, the overall behavior of the CNP dispersion is clear. For globular carbon black and planar few-layer graphene after 60 s no attraction to the magnet can be observed. Thus, the second two columns of images in Figure 5.3 only show increasing rising of particles towards the surface and sedimentation of particles to the bottle's ground. Full separation of CNP and ethanol is observed after several hours without movement. For Printex L and AVAN2 FLG therefore no reaction to this permanent magnetic field is noticed which is in good agreement with the literature review of section 2.2.

In the middle column, the reaction of NC7000 MWCNT shows small amounts of attracted particles close to the magnet after 60 s. With increasing time, the dispersion clears up due to rising and sedimentation, the percentage of MWCNT attracted to the magnetic field is small.

In the last two columns of Figure 5.3 the response of SWCNT Tuball 75 and Tuball 99 can be seen. An immediate response of SWCNT agglomerates can be observed. Depicted states after 5 s show the movement of particle clouds toward the magnet. For Tuball 75 a significantly larger amount of dispersed particles is attracted than for Tuball 99. After 120 s the mixture is mostly cleared up by showing a small percentile of SWCNT on the surface, most particles are sedimented on the ground and respective amounts are attached to the magnet side-wall of the bottle.

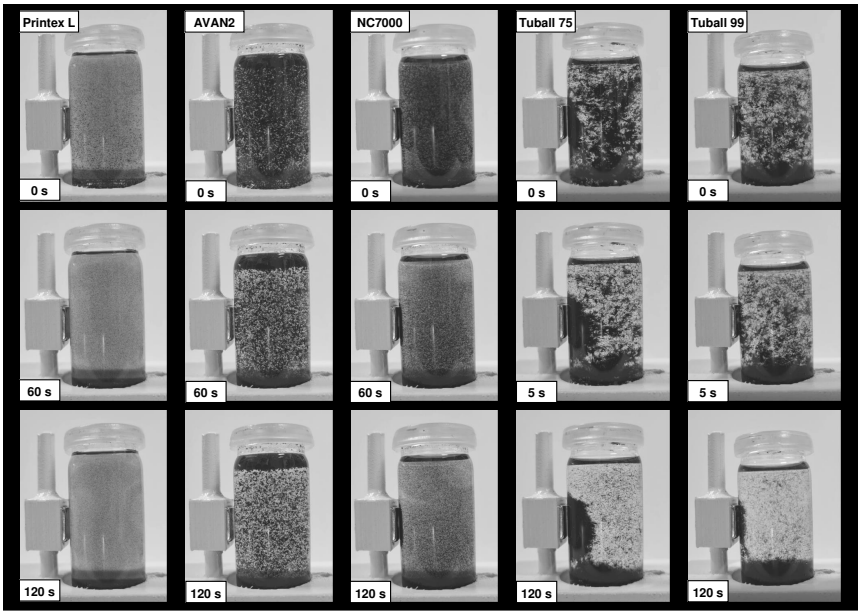

Figure 5.3: Response of CNP in ethanol to applied magnetic field

Stirring CNP by spatula into a solvent does not break down agglomerates as clearly visible in Figure 5.3. The mixture is unstable and separates quickly within minutes without stirring. Introducing a dispersion method separating agglomerates on a nano-level, ultra-sound tip-sonication is utilized to prepare water and ethanol dispersions with CNP with the same constituents as previously discussed. In Figure 5.4 the ultrasonically dispersed samples are shown. All of them show deeply black coloration from finely dispersed nanoparticles within the ethanol. For Printex L carbon black and AVAN2 FLG a separation of liquid and particles can be observed after several hours of stability. The particles sink to the ground by sedimentation. Floating on the liquid's surface is hardly observed. Agglomerate separation by sonication thus improved wetting capability. All the CNT types are stable within the dispersion for several months (observation ended 8 months after dispersion with end of this thesis and showed no changes on a macro level). No influence of the magnetic field being applied could be distinguished within the overall formed particle network. Therefore, a sufficient dispersion method for CNP like ultrasonication or three-roll milling is stabilizing CNP dispersions sufficiently. The force balance introduced by disper-

sion is stronger than applied magnetic forces, so magnetic manipulation by low permanent magnetic fields is not possible.

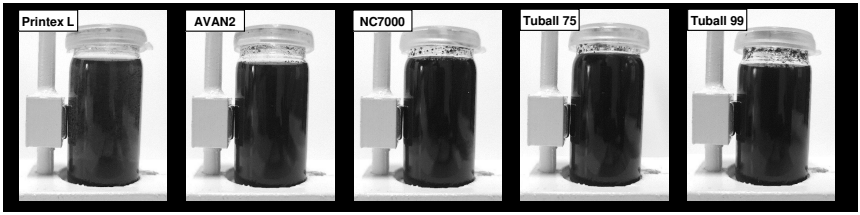

Figure 5.4: Response of CNP dispersed in ethanol via ultrasonication to applied magnetic field

In conclusion, only the tubes show a response to the permanent magnetic field when exhibited to the magnet in an agglomerated state of the CNP powder. Tuball 75 SWCNT show the strongest response by having the largest amount of CNT attached to the magnet. A slightly weaker response is achieved with Tuball 99, followed by NC7000 MWCNT. The next sub-chapter will investigate and discuss the origin of the magnetic response further to connect observations with expected behavior based on the literature review in Chapter 2.2 and 2.3.2.

5.2 CNP Characterization with Regard to their Magnetic Properties

Since Tuball 75 and 99 have the same synthesis method and differ only in post-synthesis purification, a closer look at their constitution is taken to answer the following question:

Research Question

Is the magnetic response of CNP linked to their chemical constituents?

In Figure 5.5 the weight loss by thermal degradation via TGA is shown over the respective temperature. All particle types investigated in this thesis are characterized. Thermal degradation of the carbon structures starts around 600 °C with graphene starting first at around 550 °C and carbon black being the thermally most stable with degradation starting at 600 °C. It can be seen that FLG and carbon black as well as Tuball 99 show almost no residual compounds of

2 wt%±1 wt%. NC7000 MWCNT on the other hand show a residual amount of non-degradable compounds of 10±2 wt% and Tuball 75 SWCNT have 18±2 wt% residuals for the tested temperature range.

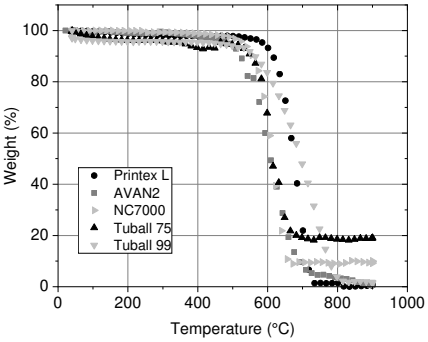

Figure 5.5: TGA curves of all evaluated CNP

A closer look at the TGA residuals by EDX analysis reveals the elemental constituents. Figure 5.6 shows analyzed weight percentages for different elements detected in the samples residuals from CNTs. Since the total amount of residuals was limited to a few milligrams, all powder was prepared on a SEM stub as shown in the miniature photograph, which also shows the difference in residual amount and coloration. The reference TEM micrographs show bundles of CNT with dark spots, which are the catalyst residues, left over from synthesis.

As can be deduced by coloration, the residuals of Tuball CNTs are red like iron-oxide (Fe_2O_3), which is also reflected in the measured elements by EDX. An iron-based catalyst is thus responsible for the paramagnetic behavior of the CNTs within the tested low-viscous media. For NC7000 the dominant metallic constituent is aluminum besides oxygen and carbon residuals. A conversation with Nanocyl S.A. confirmed an aluminum-based catalyst for their MWCNT synthesis, which is only weakly magnetically responsive in the tested set-up.

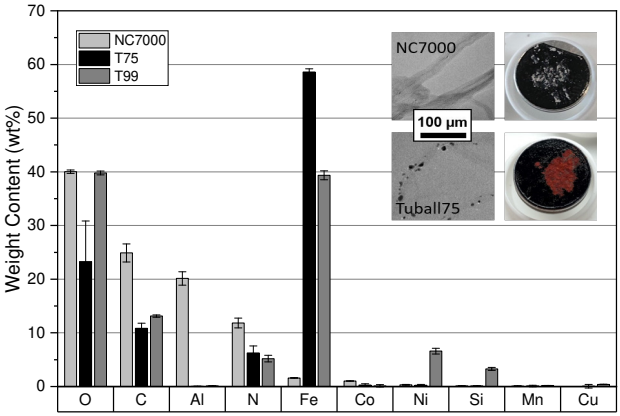

Figure 5.6: EDX analyzed element weight content of all CNP with TGA residues

In conclusion, the observed magnetic response of Tuball SWCNTs is most probably the result of iron-based catalyst residues attached to the CNTs as reported in literature [69, 82, 87, 131, 137, 139]. Depending on the position within the CNT a rotation of particles within the magnetic field is possible, but not necessary. It has been observed, that the agglomerates are magnetically responsive but the dispersion-separated tubes are too stable within the particle network, to be moved by the weak permanent-magnetic field.

For the MWCNT the aluminum-based in combination with the conductive carbon structure might cause paramagnetic response in a certain fraction of the tubes as observed in the experiments. Wildoer et al. have discussed such paramagnetic or even ferromagnetic behavior with alumina and CNTs [210].

5.3 Characterization of CNP Resin Dispersions

After the fundamental experiments to determine the CNPs general response to a low-strength permanent magnetic field the transfer into an epoxy resin-based composite was investigated to discuss the following question:

Research Question

What limits the transfer of magnetic manipulation to nanocomposites?

Because the viscosity of ethanol and water are two orders of magnitude lower than the viscosity of all resins introduced within this thesis (section 3.2) at room temperature, the possibility to decrease the viscosity by increasing the temperature of the resin is discussed.

A summary of the temperature-dependent behavior of 828LVEL, 828 and the dispersions with Tuball 75 can be found in Figure 5.7. It shows the complex viscosity at 1 Hz oscillatory frequency for 1 % strain over temperature from strain and frequency sweeps. The full diagrams of all sweeps can be found in appendix B.3. The 1 wt% T75 masterbatch in 828LVEL resin is dominated by the CNT particle network showing highest viscosity of a few kilopascal seconds. Decreasing the filler content by factor 10 decreases the complex viscosity by factor 100. A temperature dependence between 20–40 °C can be seen before the particle network dominates a temperature-independent behavior of both CNT dispersions. The neat resins 828 and 828LVEL show exponentially decreasing viscosity from the frequency sweeps. 828LVEL differs in its response for the strain sweep because a significant strain dependency below 10 % has been observed at elevated temperatures (compare Fig. B.8).

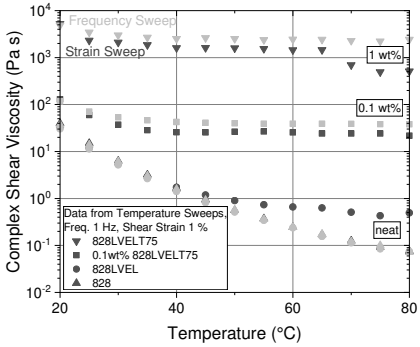

Figure 5.7: Temperature dependent resin behavior of EPON 828 and 828LVEL with Tuball 75

The response of CNP to the permanent magnetic field in epoxy resin EPON 828LVEL is shown in Figure 5.8. Samples are heated to 80 °C in an oven before setting the glass in the test-stand. The mixture was only prepared by spatula stirring because TRM dispersions are too stable as shown in ultrasonication samples. The depicted state of particles is unchanged after 60 s when the resin temperature has dropped significantly. Only for Tuball 75 a slight separation

of the agglomerate cloud next to the magnet and the rest of the mixture can be seen. In the region of highest magnetic flux, the CNTs seem to have been slightly pulled closer. Far field attraction as observed in low-viscous media can not be seen.

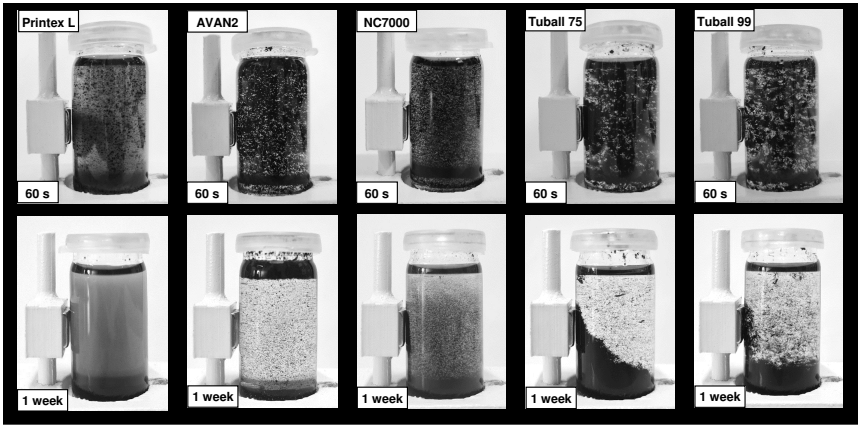

Figure 5.8: Response of CNP mixed in epoxy resin heated to 80 °C to applied magnetic field

After leaving the mixture adjacent to the magnet for a week, the particles sink down due to gravitational forces (Fig. 5.8 lower row). For Tuball 75 most particles get held up in the magnetic field so that a slope of particles forms. For Tuball 99 this effect can be seen with less agglomerated particles and even for NC7000 a thin layer of MWCNT sticks to the side wall next to the magnet. The non-magnetic AVAN2 graphene and Printex L show sedimentation or particles floating on the resin surface. The smallest particles are in a force balance within the resin remaining in the middle of the bottle.

Knowing the processing temperature of 80 °C lowers the movement resistance of particles in resin, the curing kinetics for elevated temperatures have to be considered to manufacture a composite. In Figure 5.9 the complex shear viscosity of 0.1 wt% Tuball 75 in 828LVEL over time is plotted for different temperatures from 25–80 °C. The reduced pot-life for increasing temperature is clearly visible, showing a minimum of around 1 h at 80 °C to fully cross-link. The viscosity increase to 1 kPas is already reached after 20 min, at 60 °C this viscosity is reached after half an hour, for 40 °C after about 4.5 h. It can be seen that the

full cross-linking cannot be reached for curing at room temperature, since the polymer network needs the increased molecule mobility of elevated temperatures to cross-link all functional groups of resin and curing-agent.

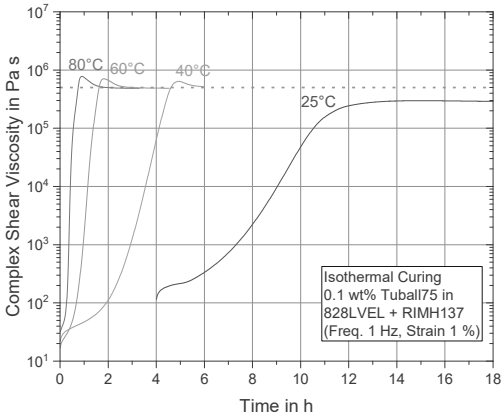

Figure 5.9: Isothermal curing curves of 828LVEL resin with RIMH137 curing agent and 0.1 wt% Tuball 75

From all deductions of rheology and magnetic-manipulation observations, it has to be concluded, that the lowest achievable resin viscosity of neat resin or a SWCNT dispersion cannot reach the range of tested low-viscosity media. Thus, a manipulation of a composite by a simple permanent-magnet set-up can not be achieved. The magnetic flux of a maximum of 120 mT is only strong enough to manipulate agglomerated CNT within water-like media. Formation of a CNT network by dispersion already stabilizes the particles against manipulation by the applied weak magnetic field.

5.4 Transfer of the Magnetic Response of CNP into a Nanocomposite

Because initial experiments with low-strength magnets positioned above open molds for nanocomposite plate manufacturing (compare appendix B) did neither show agglomeration of particles on the surface nor orientation of particles within the composite, a stronger, homogeneous field was designed. The group around Prof. T.A. Kern (TUHH, Institute for Mechatronics, M-4) designed and built the permanent magnet circuit shown in Figure 5.10. On the left side, a photograph

shows the massive steel circuit which is used to guide magnetic field lines to be most parallel and of highest magnitude in a small gap for samples in the middle. On the right side, the CAD schematic reveals two arrays of neodymium magnets which form two poles around the sample gap which is enclosed in an aluminum encasing. A tailored mold can be placed in the sample gap to manipulate a nanocomposite. All prevention has to be taken to not contaminate the magnet circuit by keeping ferromagnetic tools away from the set-up. The sample slot has to be closed when no sample is inside and all sample molds have to be properly sealed.

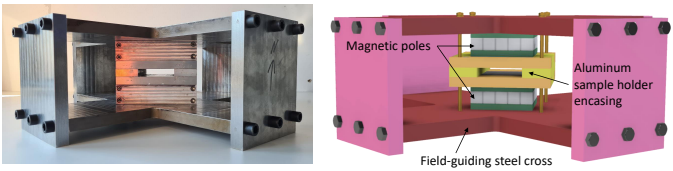

Figure 5.10: Magnet Circuit and CAD-schematic with removed covers

Figure 5.11 shows images from the Ansys Maxwell simulation (Kern, TUHH, 2021) of the magnetic field within the magnet array and steel cross for field line guidance. On the left, the vector field is shown. It can be seen that the magnet arrays below and above the sample gap show the typical circular field lines of a permanent magnet but result in an overall parallel field orientation within the sample gap. In the middle, a heat map overlay is depicted to get an impression of the field's homogeneity. On the right the view from above is shown, revealing the in-plane symmetry of the field by design.

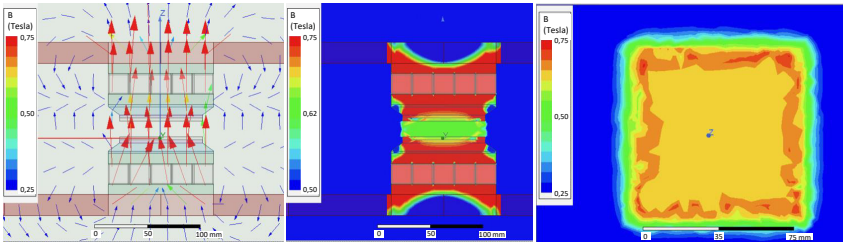

Figure 5.11: Magnetic field simulations with Ansys Maxwell (Kern, TUHH, 2021) indicating field direction (left), intensity from the side (middle) and in-plane homogeneity (right)

From the simulation a theoretical field strength of 680–700 mT should be achieved by the used set-up. Measurements within the finished magnet circuit revealed even higher values of 780 mT ± 20 mT within the sample gap. The desired uniformity of the field was achieved.

By design, the magnet circuit has a strong permanent field, which can not be switched off. Thus, for manipulation of sample material, a field gradient from the outside of the gap to the inside will be passed every time. For fillers with high ferro-magnetic response in a liquid matrix, this always means that the filler particles will move towards the gap when sliding the mold into the gap. This will always lead to an inhomogeneous particle distribution within the mold with higher concentration at the edge sliding in first.

Experiments have been conducted with varying filler content of Tuball 75 SWCNT in epoxy resin. Since the resin viscosity was proven to be too high to let the particles be moved by a magnetic field at room-temperature, all mixtures have been heated beforehand to 80 °C. Because removing the sample from the magnet circuit will lead to the same particle movement to the edge again, all samples have to be left in the circuit until fully cross-linked.

Figure 5.12 shows micrographs of cross-sections with three different filler combinations in EPON 828LVEL epoxy resin. To mimic the application case SWCNT Tuball 75 have been dispersed via TRM for homogeneous distribution in the epoxy matrix. Afterward, iron filings are mixed in via centrifugal mixing and the dispersion is pre-heated to 80 °C. Afterward, curing agent RIMH137 is mixed in and is heated again to 80 °C. The material is then poured into a mold and is immediately sealed and placed into the sample slot in the magnet circuit. It is left under the influence of the permanent magnetic field for 8 h. Iron filings are used because they show an alignment to the field lines directly and are thus perfect for visualization of the field. 0.01 wt% iron filings in epoxy resin are shown in Figure 5.12 (left), resulting in columns of iron filings parallel to the field vectors within a neat matrix. On the surface, many small bubbles are formed, since heating and mixing of the materials re-introduces air which is gassing out during cross-linking. Because no vacuum or over-pressure can be applied to the used mold, pores are formed. In the middle, the epoxy resin is modified with additional 0.01 wt% of SWCNT. The increased viscosity and introduced particle network make the air harder to gas out from the sample. The pores are distributed throughout the whole bulk here. Again, the aligned iron filing columns can be seen, but the grey-scale representative of the CNTs is not showing any orientation correlated to the magnetic field. Increased SWCNT

filler content of 0.1 wt% is depicted in Figure 5.12 (right), showing a darker coloration of the matrix material and even larger pores entrapped in the matrix. Iron filing columns are not accompanied by CNT columns either. A millimeter-sized SWCNT agglomerate is visible in the center of the micrograph, which has most probably been formed during pre-heating. It is the only one to be found in several cross-sections and can thus not be correlated to a magnetic field-induced phenomenon.

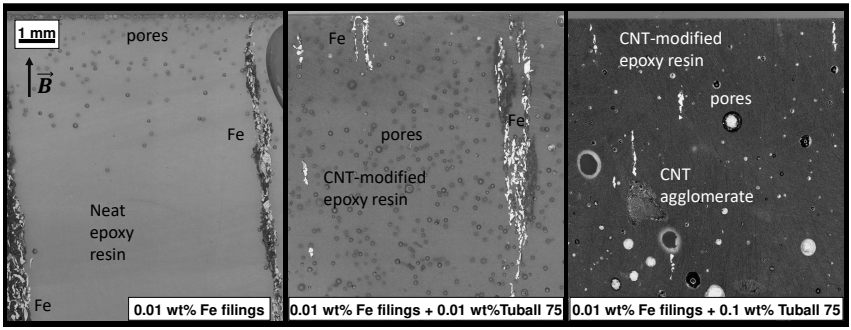

Figure 5.12: In magnet circuit cured nanocomposite cross-sections

Lower viscosity for a quick solidification or longer reaction time in the 828LVEL resin have to be achieved to result in particle manipulation. Also, the dispersion by three-roll milling or ultrasonication is stabilizing the particle network too much. Thus, only spatula-stirred samples are used in a last proof-of-concept experiment. Based on these criteria, candle wax as a low-viscosity fast hardening system has been chosen to prepare sample plates.

In Figure 5.13 (left) the upper surface of the plate can be seen. The direction in which the sample got placed into the magnet circuit can be seen - the sample was inside the magnet circuit with the right edge first, so the majority of CNT moved in that half of the plate. This is not the z-gradient direction that was aimed for but a xy-gradient. The cross-section of the sample is shown to examine the through-thickness alignment. Larger agglomerates stand parallel to the field vectors. The homogeneous magnetic field is able to align CNT agglomerates if they have a sufficient size so that the magnetic moment induced within the agglomerate is large enough to overcome the counter-forces of the matrix material. Low wax viscosity helped this re-orientation. No re-location against gravity can be seen, all agglomerates sit in the bottom of the sample.

On the right side of Figure 5.13, a latent curing agent H81b is used instead of RIMH137 to prolong the pot-life to several days for the 828LVEL epoxy resin. Similar to the wax sample, only the gradient due to the sample placement is visible. On the right side, most agglomerates are visible, also the gradient is less harsh than for the low-viscosity wax. A hurdle to manufacturing fully cured samples with H81b is the elevated temperature of 150 °C that is necessary to fully cross-link. This has to be done in a post-curing process outside the magnet circuit. Significant re-agglomeration in lateral and thickness direction of the sample could be observed after curing. The re-agglomerated state is not shown here, since all gradients disappeared.

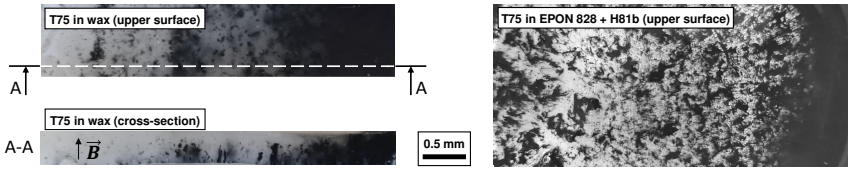

Figure 5.13: Upper surface images of in magnet circuit cured nanocomposite cross-sections of wax (left) and with a latent curing agent H81b (right)

5.5 Conclusion on the Application of Magnetically Manipulated Nanocomposites

The final aim to manufacture through-thickness gradient coatings by permanent magnetic manipulation as sketched in Figure 5.1 could not be achieved. Wang et al. [211, 212] were able to create gradient composites by adjusting two opposite magnetic fields to have the highest flux gradient plane on the composite's surface. This technique is promising to achieve the through-thickness gradient but requires time-consuming fine-tuning of the magnetic field. In contrast to the open mold experiments with only one magnet above the composite as described in appendix B, Figure B.3 the opposite field alignment might only compact CNTs in a surface layer. Because the publication reports on the manipulation of small spherical particles, the approach should possibly be started considering that. A particle functionalization has proven to be powerful by several publications [87, 89, 132, 133]. For gradient formation in thin films, the dimensions of particles have to be considered. SWCNT may exhibit lengths of up to 5 µm, in comparison to a thin coating this might influence the particle's mobility within the resin. When a percolated well-dispersed network is formed, the particle-particle interaction limits the gradient formation.

The integration of a permanent magnetic manipulated CNT network for fiber reinforced composites modification was not achieved. If future work can achieve particle alignment within a nanocomposite the transfer to FRP is challenging as well. Spatial confinement has been proven to be restricting, the homogeneous distribution of particles is necessary to avoid the particles from filtering.

Nonetheless, several important outcomes to understanding the nanocomposites under magnetic field influence can be derived from this work.

Addressing the Research Questions

It is not possible to manipulate epoxy nanocomposites from dispersed carbon nanoparticle intermediates with homogeneous permanent-magnetic fields. This chapter approached the limitations with as-received CNP in low-viscous media and epoxy resins experimentally. The initial idea to create through-thickness gradients would only be possible with a carefully tailored gradient field.

The magnetic response of CNP was linked to their chemical constituents in the form of metal catalyst residues incorporated within the tubes. From all tested as manufactured CNP only carbon nanotubes have a response to low permanent magnetic fields in their agglomerated state. Therefore, the movement of particles in magnetic field gradients is possible. The strongest reaction to magnetic manipulation has been observed for Tuball 75 SWCNT which have the highest residue content of an iron-based catalyst. Low-viscous media like water and ethanol enabled a permanent magnetic manipulation within seconds.

Interaction forces with epoxy resin limit the transfer of magnetic manipulation into a nanocomposite. The resin viscosity limits particle mobility and therefore increases the required manipulation time to several days which is not practical for gradient coating applications.

Moreover, particle dispersion by ultrasonication or TRM has been proven to be very stable over time and resistant to permanent magnetic manipulation. The particle-particle interaction of dispersed CNTs in low-viscous media is stable for over 8 months, experiments with TRM-processed material did not show manipulation under single magnets or under the influence of multiple combined magnets in the homogeneous field circuit.

An orientation of nanotubes parallel to the field vector of a homogeneous field is only possible if the magnetic catalysts are distributed inhomogeneously on or within the particles so that a magnetic moment can be created. Agglomerates might not show an alignment parallel to the field if several catalyst residues are in a force balance of magnetic field and particle-resin interaction.

Overall, future experiments have to create magnetic field gradients rather than homogeneous fields, since an alignment is not easily possible. Tailoring magnetic gradient fields to a certain sample area might achieve gradient nanocomposites. Also, a functionalization with magnetic iron oxide or nickel nanoparticles as reviewed in the literature is promising, since as received CNP never exhibit uniform magnetic residue distribution.

6 CNP Nanocomposites as Thermal Sensors using DC Resistivity

Within this last chapter, the potential of CNP composites as a resistive temperature sensor is investigated as a possible application field. Bulk samples of CNP-modified EPON 828LVEL epoxy are used to measure the DC electrical resistance in dependence on a wide temperature range below and above the glass transition of the resin. This chapter gives an overview of different CNP types and filler content including SWCNT, which have not been reported on in literature as much as CB and MWCNT (compare section 2.4). The following research questions are investigated:

Research Questions

Which CNP is most suitable to be used in a nanocomposite temperature sensor? Is the DC resistive behavior reversible over large temperature ranges spanning matrix transition temperatures?

6.1 Thermal Characterization of CNP Nanocomposites

The samples have been produced as described in Chapter 3.4 and 3.5 four years prior to the temperature-dependent characterizations discussed in this chapter. First, DSC measurements to validate curing state and aging state of the composites are analyzed. To characterize the reactive response of the material over the temperature range of the standard climate chamber experiment, Figure 6.1 shows a representative DSC curve for a 0.1 wt% Tuball 75 composite.

Initial cooling from room temperature down to −50 °C (light blue) shows large fluctuations and can thus not be analyzed further. The first heating, depicted in red, is the heat ramp during which the DC resistance is measured in the climate chamber experiments. No cross-linking reactions can be seen. Nonetheless, the glass transition is overlapped by an endothermic relaxation peak around 100 °C. After cooling down to room temperature (medium-blue) the endothermic peak

is not to be seen on the second heating ramp (light-red). A clear glass transition can be seen as an inflection. Final cool-down to room temperature (dark blue) is identical to the second cool-down. Literature confirmed that this endothermic peak results from the composite's temperature history and does not indicate an incomplete curing state [155, 156] (compare section 2.4). Since initial curing of the composite was done at 80 °C and cooling afterward was done with about 0.5 K/min, the now applied DSC heating rate differs greatly with 10 K/min. After initial cooling and heating at this new rate, the endothermic relaxation peak is apparent. In second cooling and heating the rates are identical for the last undergone thermal cycles and thus the endothermic peak does not occur.

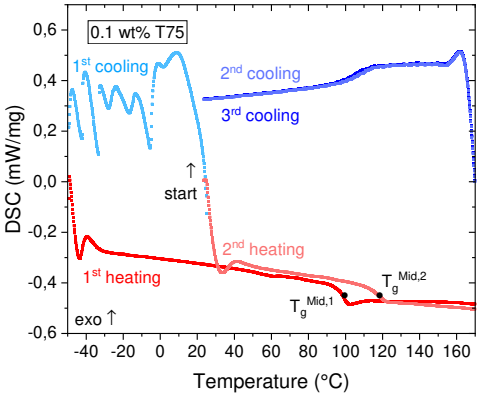

Figure 6.1: Representative DSC analysis curve for 0.1 wt% T75 composite

A summary of all measured glass transition temperatures depending on filler content for all particle types can be found in Figure 6.2. The glass-transition temperatures T_g^{Mid} of 117 °C±1 °C determined from the inflection during second heating are independent of particle type and filler content. The T_g^{Mid} determined at the inflection of overlapping relaxation peak during the first heating lay within 99 °C ± 1 °C independent of filler type or content.

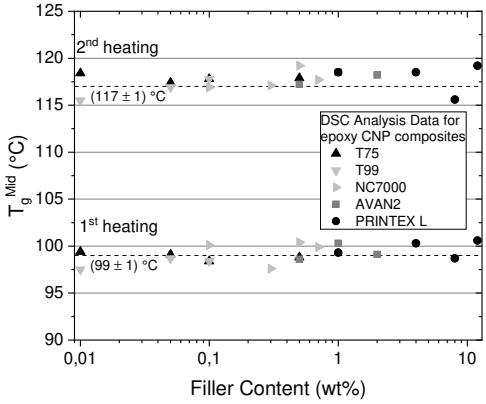

Figure 6.2: Glass Transition Temperatures T_g^{Mid} for all CNP nanocomposites over filler content

For a broader temperature range between $-100\,^{\circ}\mathrm{C}$ and $170\,^{\circ}\mathrm{C}$ the DMTA chamber was used for T-sensing experiments discussed in 6.2.2. In Figure 6.3a) the thermo-mechanical characterization of the composites elastic modulus and $\tan(\delta)$ is shown for 0.1 wt% T75 and T99, 0.3 wt% NC7000, 1 wt% AVAN2 and 1 wt% Printex L to see the transition temperatures. For each filler type a representative curve is plotted, within the measurements statistic variation they exhibit identical β-transitions at around $-40\,^{\circ}\mathrm{C}$ and glass transitions measured at the $\tan(\delta)$-peak of $110\,^{\circ}\mathrm{C} \pm 5\,^{\circ}\mathrm{C}$. In the elastic modulus, a rapid decrease can be observed from T_g^{onset} $=90\,^{\circ}\mathrm{C}$ onwards. No clear dependence of glass transition temperature on filler content can be observed, the cross-linking state seems not to be affected measurably by the particle's surface area or excluded volume. However, higher filler loading increases the stiffness at a certain temperature by adding a stiffer carbon nanoparticle network to the polymer. In Figure 6.3b) the elongation of the samples within the elastic modulus DMTA test can be seen. A significant change in behavior is apparent above $100\,^{\circ}\mathrm{C}$ above T_g.

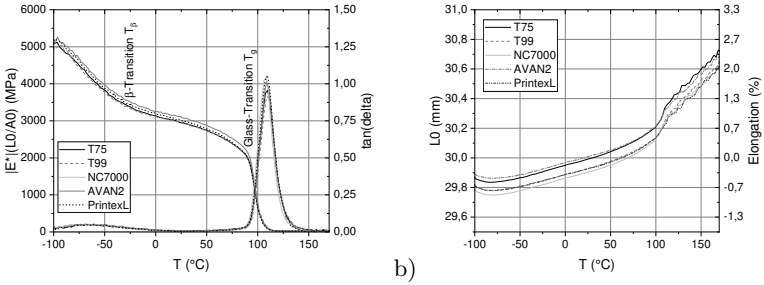

Figure 6.3: a) Representative DMTA curves and b) specimen elongation for selected CNP nanocomposites

All samples tested have been stored under lab conditions for 4 years prior to testing. Therefore, moisture uptake was also investigated. Figure 6.4 shows the water content calculated by the weight loss after 4 weeks of re-drying under vacuum at 80 °C. All samples are identical to the ones used in the T-sensing experiments since six samples have been prepared but only five are measured per configuration for DC resistivity. The moisture uptake under lab conditions for 4 years is determined to be filler type and content independent with 0.71 wt% ± 0.03 wt%. For increasing filler loading of CB Printex L a linear trend of increasing water content can be interpreted.

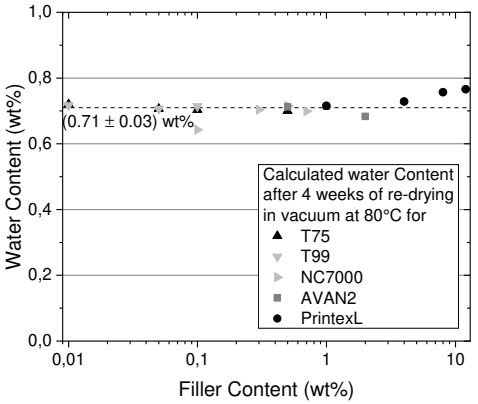

Figure 6.4: Re-dried water content for CNP composites over filler content

To conclude the thermal characterization of the CNP nanocomposites, it can be stated that all properties are in good agreement to the results of Voormann [2] after being stored under laboratory conditions for four years. No significant aging could be observed, so mechanical properties are not compromised. Moisture uptake will be considered, since a certain water content within the composite is known to bridge conductive networks within a composite [10, 29] or could show anomalies in behavior at water phase transition temperatures. Consequently, cyclic repetition of the measurements for selected material configurations will be conducted to observe the response stability.

6.2 Results and Discussion of CNP Nanocomposite Application as Temperature Sensors

The following sections discuss electrical resistance measurements of the CNP composites under the influence of temperature and compare the electro-resistive to the mechanical response. First, different filler contents of all CNP types are compared with absolute resistances to select a configuration best suited for temperature sensor applications in section 6.2.1. Specific volume conductivity for all samples and their geometry can be found in appendix C. For the most promising material cyclic and rate-dependent behavior is discussed. Section 6.2.2 further elaborates on mechanical and electrical properties at low temperatures to evaluate possible application ranges.

6.2.1 Resistive Behavior of CNP Nanocomposites under the Influence of Temperature

Starting with SWCNT, the measured resistance over temperature is shown for Tuball 75 in Figure 6.5. The four different filler loadings of the composites differ clearly in decreasing resistance with increasing filler content. For each filler content, five samples were tested and are plotted in the diagram to show the minimal deviation. For lowest filler content of 0.01 wt% the measured resistance is around 1.5 MΩ, with 0.05 wt% the resistance decreases by one order of magnitude below 100 kΩ. For 0.1 wt% it starts with 30 kΩ and with up to 0.5 wt% the resistance starts in the order of 20 kΩ. For each filler loading 5 samples are plotted, within the scales resolution their deviation is minimal. Starting at −50 °C the resistance decreases linearly on the logarithmic scale, indicating an exponential decrease over temperature until the slope changes at around 100 °C. The resistance decrease continues steeper with temperatures over the T_g region.

Measuring the resistance for samples crossing T_g for the first time reflects the phase transition of the matrix. If this is possible after cyclic thermal loading will be discussed later. Overall, SWCNT seem promising for application as a temperature due to their monotone NTC behavior.

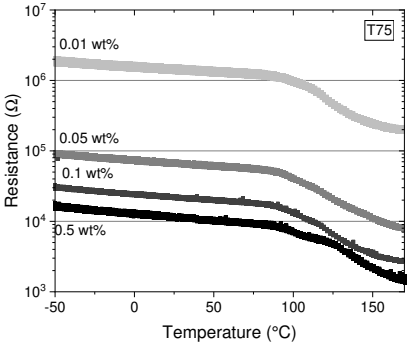

Figure 6.5: Temperature-dependent resistivity of T75 nanocomposites

Tuball 99 SWCNT with higher purity show a less pronounced change in slope above T_g and higher overall resistance for each filler content in comparison to Tuball 75. Composites with three different filler contents have been tested and are depicted in Figure 6.6. For lowest filler content of 0.01 wt% the measured resistance starts around 2 MΩ, with 0.05 wt% the resistance decreases by one order of magnitude below 200 kΩ. Highest tested filler content of 0.1 wt% decreases the resistance to 100 kΩ. Both SWCNT types show qualitatively similar temperature-dependent responses with a negative temperature coefficient of resistivity. However, the higher purity and thus reduced residual metallic catalysts show higher resistivity. For lowest filler content the resistance is around 30 % higher, for 0.05 wt% the resistance is doubled, above the percolation threshold at 0.1 wt% the resistance is five times as high. Therefore, the metal catalysts have a significant influence on SWCNT's electrical conductivity. On the other hand, decreased catalyst residuals in T99 make the resistive response above T_g less pronounced than for T75. Nonetheless, T99 could be used for temperature sensing.

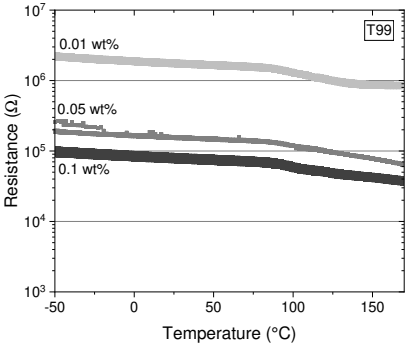

Figure 6.6: Temperature-dependent resistivity of T99 nanocomposites

MWCNT NC7000 show the influence of filler content on overall resistance as well. In Figure 6.7 the four different filler contents are compared. For 0.1 wt% NC7000 the resistance of around 7 MΩ is fairly temperature independent until the glass transition is surpassed. In comparison to the SWCNT with resistances in the same order of magnitude the MWCNT filler content has to be an order of magnitude higher. This discrepancy is reduced with higher filler loading of MWCNT reaching the percolation threshold. For 0.3 wt% 150 kΩ are the almost constant resistance between −50 °C and 125 °C, for 0.5 wt% it is 60 kΩ and for 0.7 wt% 20 kΩ. MWCNT nanocomposites thus do not exhibit NTC behavior over the full temperature range. This limits their application potential, especially for low-temperature ranges.

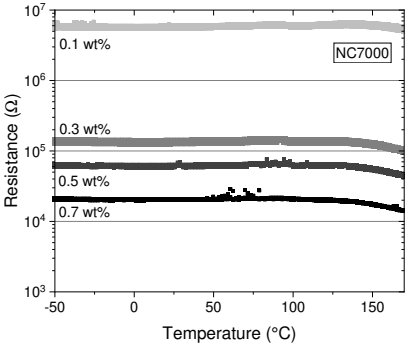

Figure 6.7: Temperature-dependent resistivity of NC7000 nanocomposites

For planar FLG AVAN2 no resistance could be measured within the given set-up. Filler content and re-agglomeration during curing are the cause for a mostly capacitive material response as observed in Figure 4.37 for the resin dispersions.

For globular CB Printex L, the results can be found in Figure 6.8. Overall resistances an order of magnitude higher than for CNTs are measured with PCT behavior, so the resistance increases with increasing temperature. This is in good accordance to the literature as presented in Chapter 2.4. In contrast to tested CNT nanocomposites, where the five samples showed fairly similar values for identical filler content, here the resistive response for 8 wt% (gray) and 12 wt% (Black) filler content are intertwined and can not be distinguished by their resistivity. During all measurements a certain temperature between −25 °C and 100 °C was reached, where the resistance exceeded the upper limit of the measuring device. Porosity of the samples, local alterations of the particle network and the temperature-induced matrix volume expansion separating conductive pathways make the sensor application of these nanocomposites not favorable. This material system is excluded from further experiments, all further evaluations regard the different CNT types.

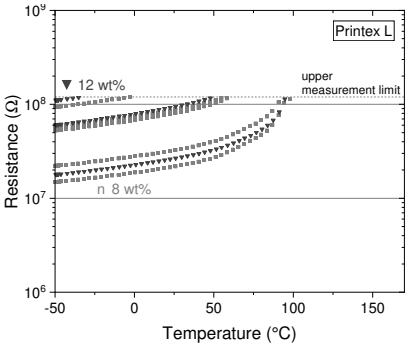

Figure 6.8: Temperature-dependent resistivity of Printex L nanocomposites

Since literature is sparse in low-temperature behavior the measurement range was extended to −100 °C by building a second miniaturized sample holder to fit within the DMTA test chamber. In Figure 6.9 the two set-ups are shown side by side. On the left side, the five tested samples can be seen within the climate chamber. On the right side, the smaller sample holder can be seen beside the DMTA clamps with a sample.

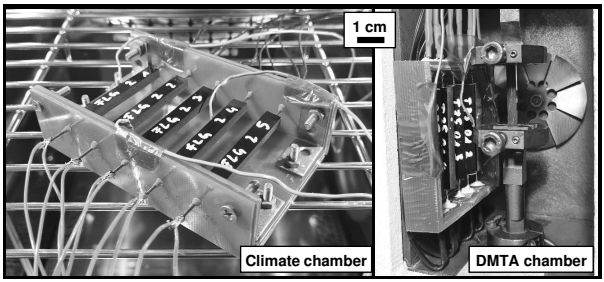

Figure 6.9: Climate chamber and DMTA chamber set-ups for temperature ssensing experiments

Figure 6.10 compares the filler content 0.1 wt% for all CNT types in both chambers for one representative sample each. The DMTA chamber experiment is the third cycle for NC7000, the second cycle for T99 and the seventh cycle for T75. For all measurements, the five samples from the climate chamber experiments have been measured again (compare appendix C). For NC7000 and T99 the resistive response up to the glass transition are similar in both test set-ups. The only exception is the temperature range between 0–20 °C for NC7000, where the resistance drops for all measured samples, this behavior is further explored in Figure 6.11(b). For T75 the difference after cyclic temperature sensing is apparent. While a pronounced change in resistance change over temperature above 100 °C is observed in the first heating, the behavior from the third cycle on is linear on the logarithmic scale. Third heating in the climate chamber and the experiments in the DMTA chamber (conducted after cycle 6) show similar behavior. This will be discussed in more detail in the next paragraph. Comparative experiments shown in this Figure 6.10 confirm the choice of material configuration to be 0.1 wt% T75 for lowest overall resistance.

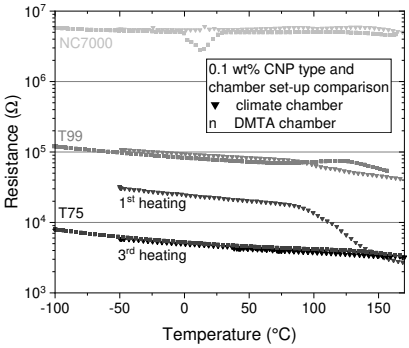

Figure 6.10: Temperature-dependent resistivity of nanocomposites with 0.1 wt% filler content for climate and DMTA chamber set-up

Cyclic thermal loading of the material has to be explored, therefore, Figure 6.11(a) shows the repeated measurements for T75 from the climate chamber. The increasing conductivity and thus decreasing overall resistance can be seen over the first three cycles. Different sequences have been tested. Initially, the thermal loading included one heating cycle from −50 °C to 170 °C. After several days, the second experiment included a second heating, a cooling and a third heating cycle, which are plotted over temperature in the diagram. The second heating starts at an initial resistance value lower by factor 3 compared to the first heating. In the subsequent cooling and following heating the resistance value are very similar. A repetition of the double-heating experiment after another day of no thermal load on the samples reveals stable temperature-dependent response. Further temperature cycling in the DMTA chamber confirmed that the electric properties are stable under further thermal loads spanning the low-temperature transition as well as glass transition temperature of the matrix.

In Figure 6.11(b) the cyclic thermal loading of 0.1 wt% NC7000 can be seen. One sample has been picked out to discuss characteristic features, all other samples can be found in appendix Figure C.3. First heating in light gray between −50–170 °C exhibits the drop of resistivity around 100 °C, which can be seen in Appendix C for every filler content of NC7000. After initial NTC behavior, the composite shows PTC behavior above 25 °C. This has been explained by thermal expansion of the matrix and subsequent separation of conductive pathways [166, 176, 178, 180]. The drop in resistance might be caused by the starting glass transition of the matrix, which causes the spring-loaded contact pins to be indented into the sample more. The influence of the endothermic relaxation

processes within the polymer network, which also occurs in this temperature range, is unknown. The pronounced NTC behavior with rapidly decreasing resistance for elevated temperatures above T_g can be explained by re-connection of conductive pathways due to the increased molecule mobility. The second test was conducted under identical conditions in the climate chamber and included heating from −50–170 °C, cooling down and heating the same cycle again. The drop around 100 °C and the PTC behavior are not visible anymore. For the cool-down and repeated heating an overall decrease in absolute resistance is measured, which might be the result of improved contact with the pins after one heating cycle. The third experiment (dark grey) was moved to the DMTA chamber but malfunctioned above room temperature, so only the temperature range from −100 °C to 25 °C was measured for all samples. The graph is following the initial values for all of the first heating ramps of tests 1 and 2. A fourth test was conducted immediately after the failed attempt over the whole range of −100 °C to 170 °C (black). The values are similar to the repeated heating from the climate chamber, so this could confirm the change of contact by the pins over time. A drop of resistivity is observed for all NC7000 samples in the DMTA chamber around 0–25 °C but none of the other CNP. This drop is right above the solid-liquid transition of water, which is apparent within the DMTA chamber because of the relative air humidity. It is worth noting that this drop occurred only for MWCNT but not SWCNT.

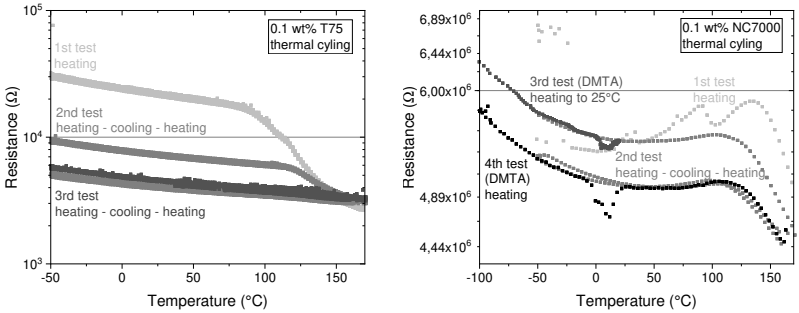

(a) 0.1 wt% Tuball 75

(b) 0.1 wt% NC7000

Figure 6.11: Temperature-dependent resistivity of 0.1 wt% T75 and NC7000 nanocomposites over several test cycles

To conclude, investigating the cyclic thermal loading of nanocomposites reveals that SWCNT epoxy nanocomposites can be used in repeated sensing applications

spanning both matrix transition temperatures. The temperature-dependent behavior stabilizes with increasing cycles and initial change of resistance decrease above T_g diminishes. Therefore, a percolated SWCNT network makes a good sensor with monotone NTC behavior without being affected by the polymer matrix. For MWCNT NC7000 initial alternating NTC and PTC behavior stabilizes over cyclic thermal loading as well. However, application across the whole temperature range is not possible, since resistance in the mid-range between the matrix transition temperatures is not unique. Thus, T75 nanocomposites are further analyzed in terms of their sensing ability.

The rate-dependent response of the sensor has been considered. In the DMTA chamber rates up to 10 K/min can be considered and are shown in Figure 6.12. For comparison, a segment of a climate chamber experiment is plotted as a line with the determined stable heating rate of 1.43 K/min. This heating rate was also used in the first DMTA chamber experiment, plotted as solid black triangles. A change in curvature and thus a steeper decrease of resistance over temperature can be seen above 130 °C. The DMTA chamber experiment shown has been conducted after seven runs in the climate chamber under identical conditions over several days. But still, the change in resistive response at elevated temperatures is only apparent in the first DMTA chamber experiment. One possible explanation could be the softening of the matrix material above T_g, which can lead to slight indentation of the spring contact pins into the materials and thus possibly reduce the contact resistance. For the difference in resistance between climate and DMTA chamber, the sample contacting via spring contact pins might be considered as well. All rate alterations marked with the gray-scale squares have been conducted subsequently without re-contacting the samples. For these, the overall resistance follows the same line and no change for higher temperatures can be observed. This might confirm, that contacting the sample always leads to an off-set in overall resistance and change in high-temperature behavior. For the different heating rates, no significant difference can be seen. Higher scan rates result in sparser data per temperature range since sampling is defined as time-dependent. The influence of heating rate and sample geometry on the DMTA measurement can be found in appendix C in Figure C.4. The sample geometry showed no influence, an increasing heating rate however shifts modulus curve and tan(δ)-peak to higher temperatures, since the material can not adapt to applied temperature at rates higher than 2 K/min.

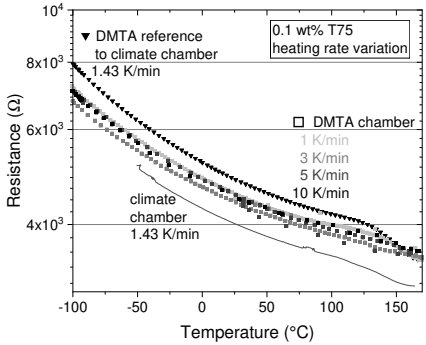

Figure 6.12: Heating rate and temperature-dependent resistivity of 0.1 wt% T75 nanocomposites

Finally, the question of whether or not one of the proposed resistivity models from Chapter 2.4 can be fitted to the acquired data has to be discussed. The fluctuation-induced tunneling model (FITM) as presented in section 2.4 equation 2.39 is the most commonly applied model for nanocomposites. However, the representation of calculated quantities has been critically discussed by Wichmann [172, 190]. Figure 6.13 shows the average volume conductivity calculated with equation 3.8 of CNT nanocomposites with varied filler content and particle type. Volume conductivity for all tested samples can be found in appendix C. For each particle (indicated by different colors) the conductivity increases with increasing filler content as discussed before. For each of the SWCNT data sets at least one linear segment in the semi-logarithmic plot can be seen. This segment between 225 K and 350 K is fitted with the FIT model to determine σ_0, T_0 and T_1 in equation 2.39 in OriginLab using an exponential function with three parameters. For the MWCNT NC7000 the model is not expected to be fitting, since PTC and non-linear behavior on semi-logarithmic scale have been observed. Consequently, the fitting algorithm does not converge due to mutual dependency of parameters. For Tuball 75 and Tuball 99, the FIT model can be applied and the parameters determined are listed in Table 6.1. The initial conductivity σ_0 increases with higher filler content, respectively. For T75 the change over cyclic loading is depicted, showing an increase from first to third thermal loading as well. Cycle seven is similar considering the standard deviation. The temperature T_1 related to activation energy-induced tunneling decreases with increasing filler content for T75 (considering that the sign must be minus according to equation 2.39, because it marks a lower temperature limit that must be exceeded for tun-

neling). For T99 this cannot be seen. T_0 as the lower characteristic temperature decreases for T75 from 0.05–0.1 wt% and over cyclic thermal loading. For T99 a negative value occurs, which is not plausible according to the model.

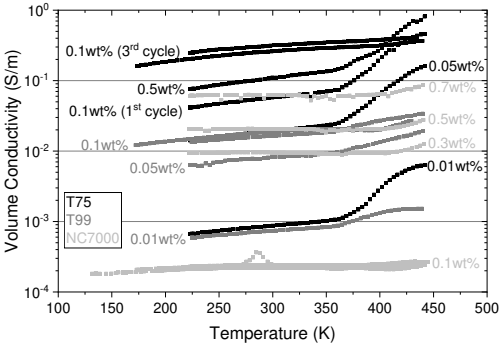

Figure 6.13: Volume conductivity over temperature for all tested CNT nanocomposites

Table 6.1: Parameters determined by fitting Eq. 2.39 $\sigma = \sigma_0 \cdot \exp(T_1/(T+T_0))$ in OriginLab

Filler Content ($wt\%$)	CNP	σ_0 (mS/m)	T_1 (K)	T_0 (K)
0.01	T75	10.98	-2057.07	512.05
0.05	T75	521.05	-2981.28	604.31
1^{st} cycle 0.1	T75	486.82	-1233.33	277.13
3^{rd} cycle 0.1	T75	682.27	-262.05	37.29
7^{th} cycle 0.1	T75	608.26	-286.68	38.44
0.5	T75	-	-	-
0.01	T99	3.07	-787.06	251.60
0.05	T99	13.20	-101.33	-90.35
0.1	T99	78.72	-1057.25	374.81
2^{nd} cycle 0.1	T99	42.91	-278.18	37.49
0.1-0.7	NC7000	-	-	-

Compared to Wichmann [172, 190] the calculated temperature values in table 6.1 are significantly higher, the initial conductivity σ_0 for these SWCNT is also one order of magnitude higher than for the MWCNT of Wichmann. Calculating the tunnel distance s and contact area A with the values calculated here leads to significantly smaller results ($s \sim 10^{-19}m^2$, $A \sim 10^{-65}m^2$), which are even less plausible for a particle network that probably consists of touching CNT. The SWCNT used in this thesis have a high aspect ratio (compare SEM images in Fig. 3.1) and are believed to form an interconnected particle network based

on observing the dispersion process in chapter 4.2.2 or the dispersion stability in chapter 5.1. Wichmanns ARKEMA Graphistrength C-100 MWCNT are more agglomerated balls of entangled CNT. These would be harder to separate by TRM and are therefore more likely to have gaps filled with resin between particles.

A fully formed CNT network as expected to be formed in this thesis could then be described by the resistance of each particle and their respective contact resistances. Therefore, the main influence of temperature-dependent resistivity would be the intrinsic semi-conducting behavior according to equation 2.32. Table 6.2 gives the parameters for initial conductivity σ_0 and band gap energy barrier E_g for all CNT types and filler contents for the temperature range from 225–350 K determined by fitting the data to equation 2.32 in OriginLab. For σ_0 the values increase with increasing filler content. The band gap energy increases for higher filler content for T75. For T99, a slight decrease can be observed. For NC7000 the sign changes to negative values for the band gap energy, which is not plausible. The change is minimal and is attributed to the PTC behavior in the mid-temperature region. However, the behavior below T_g can be described by the exponential equation.

Table 6.2: Parameters determined by fitting $\sigma = \sigma_0 \cdot \exp(-E_g/2kT)$ in OriginLab

Filler Content ($wt\%$)	CNP	σ_0 (mS/m)	E_g (meV)
0.01	T75	2.10	45.00
0.05	T75	52.42	51.24
1^{st} cycle 0.1	T75	165.40	54.35
3^{rd} cycle 0.1	T75	618.39	35.03
7^{th} cycle 0.1	T75	546.66	38.22
0.5	T75	357.76	60.82
0.01	T99	1.53	37.41
0.05	T99	17.18	38.87
0.1	T99	31.32	33.08
2^{nd} cycle 0.1	T99	38.83	37.40
1^{st} cycle 0.1	NC7000	0.22	-1.03
2^{nd} cycle 0.1	NC7000	0.26	6.24
3^{rd} cycle 0.1	NC7000	0.27	9.25
4^{th} cycle 0.1	NC7000	0.29	6.46
0.3	NC7000	9.16	-1.50
0.5	NC7000	20.18	-0.66
0.5	NC7000	51.91	-7.68

To discuss fitted parameters further, a deeper understanding of the real particle network would be necessary. Experimentally, these values can not be deter-

mined, because particle distribution, conductivity of individual CNTs and their interaction are not trivial to determine. Both models have large drawbacks in unknown parameters. Further measurement would be necessary to develop a suitable model. The comparison to Wichmann's results [172, 190] make clear that the standard tunneling mechanism can not be seen for Tuball SWCNT or NC7000 MWCNT. For the last subsection of this chapter, the focus is therefore driven back to the extended temperature range investigated within this thesis. A better understanding of the low-temperature mechanical and electrical behavior shall be discussed.

6.2.2 Comparison of Resistance Measurements and Thermo-mechanical Characterization

A comparison of elastic modulus and resistance for 0.1 wt% of the three different CNT types can be seen in Figure 6.14 as an overview. Electrical and mechanical measurements were conducted independently of each other, this section does not address structural health monitoring of nanocomposites. This chapter focuses on a comparison between resistance and elastic moduli, especially for the low-temperature range, which is reported on less in the literature.

The lowest resistance but in Figure 6.14 the highest modulus is observed for T75 SWCNT. The dominant particle network increases the stiffness of the nanocomposite and enhances the electrical conductivity, as discussed before. These effects are less pronounced for T99 SWCNT due to lower metal catalyst content within the tubes, which have positive effects on the overall conductivity. For NC7000 MWCNT the lower aspect ratio of the tubes leads to less conductive pathways at the same filler content and thus highest resistivity of the three CNTs. The MWCNT network is not yet percolated for this filler content of 0.1 wt%. Since the three resistances differ in one order of magnitude each between the different CNT types, a deeper understanding can be gained by discussing their respective resistive and mechanical response individually.

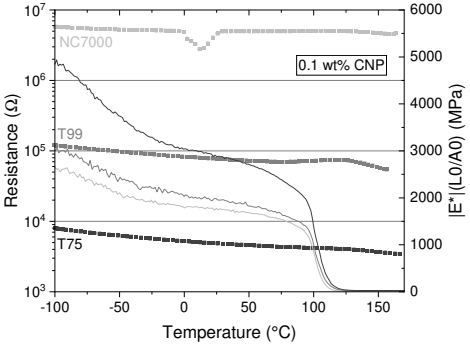

Figure 6.14: Temperature dependent resistivity for 0.1 wt% nanocomposites with DMTA overlay for complex elastic modulus

For T75 the stable response after several temperature cycles is compared to the DMTA measurement in Figure 6.15. Elastic modulus and $\tan(\delta)$ are shown. The β-transition is visible from $-50\,^{\circ}\mathrm{C}$ to $-25\,^{\circ}\mathrm{C}$ in $|E^*|$ transgressing from a more temperature-influenced behavior to be influenced less by temperature changes between $-25\,^{\circ}\mathrm{C}$ and $60\,^{\circ}\mathrm{C}$. The $\tan(\delta)$ peak for the β-transition is less pronounced than for the glass transition temperature. A smoothed out β-transition has to be expected ([144]) since the curing agent RIMH137 consists of two different amines poly(oxypropylene)diamine (50–75 wt%) and 3-aminomethyl-3,5,5-trimethylcyclohexylamine (35–50 wt%) [213]. These will show slightly different β-transitions due to their molecular structure. Moreover, the literature review suggests that for post-cured materials such as these nanocomposites, the β-transition peak in $\tan(\delta)$ is minimized [145]. The electrical resistance of the nanocomposite is not changing around the β-transition. At around $80\,^{\circ}\mathrm{C}$ the onset of T_g can be seen. The peak of $\tan(\delta)$ can be found around $110\,^{\circ}\mathrm{C}$ and coincides with the change in temperature-dependent resistive behavior. This transition temperature for the resistance is thus slightly higher than T_g determined by the inflection of elastic modulus or the change in volume approximated by the sample elongation in Figure 6.3b).

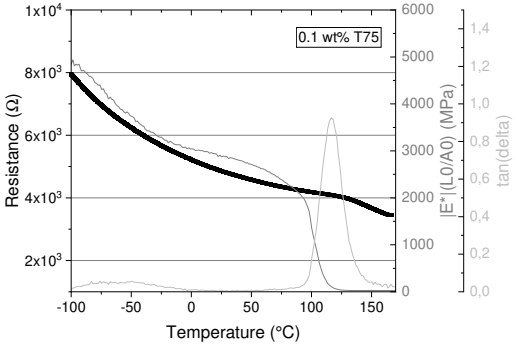

Figure 6.15: Temperature dependent resistivity for 0.1 wt% T75 nanocomposites with DMTA overlay for complex elastic modulus

For Tuball 99 the behavior is similar despite the PTC behavior at temperatures slightly below T_g as shown in Figure 6.16, which coincides with changing elongation of the sample due to thermal expansion of the epoxy matrix. The transition to a strong NTC decrease of resistance starts at temperatures, where $\tan(\delta)$ has exceeded its maximum. No direct correlation between elastic mechanical and resistive behavior can be found for T99 either.

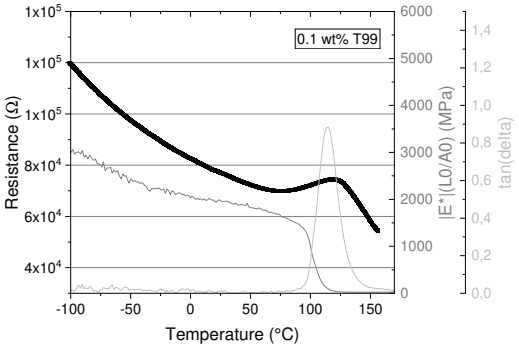

Figure 6.16: Temperature dependent resistivity for 0.1 wt% T99 nanocomposites with DMTA overlay for complex elastic modulus

For NC7000 Figure 6.14 shows the respective $|E^*|$, $tan(\delta)$ and resistance over temperature from a stable thermal loading cycle (cycle 5). The sudden drop in resistance from 0–25 °C could not be resolved. A connection to the phase

transition of humidity within the DMTA chamber would have been observed for all other nanocomposites tested, too. A measuring error cannot be excluded, since the drop is observed for all measured samples (compare Appendix C, Fig. C.3(b)). The resistive behavior changes similar to the elastic modulus for low temperature. However, the behavior transition temperatures observed in resistance are shifted by approximately 25 °C compared to the elastic modulus.

The shape of the resistance curve is similar to the temperature-dependent behavior of n-doped semiconductors [27]. At low temperatures, the defects are conducting. This could be attributed to the residual metal catalysts within the graphidic structures. In the mid-temperature range, the conduction mechanism of defects is exhausted leading to no significant change of the resistivity until glass transition. Here, the slight changes in volume and structure of the particle network induced by the temperature can be attributed to the increasing conductivity as well as the intrinsic conductivity of semiconducting CNTs. The behavior of an intrinsic conductor will show increased conductivity as described in Chapter 2.4.

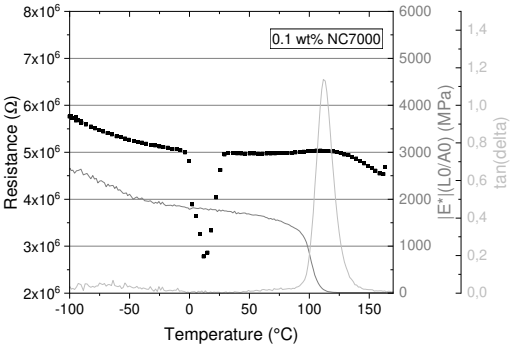

Figure 6.17: Temperature dependent resistivity for 0.1 wt% NC7000 nanocomposites with DMTA overlay for complex elastic modulus

Overall, the behavior of all CNT nanocomposites shows three different stages in elastic modulus decrease over temperature. Within the low-temperature regime between $-100\,°\mathrm{C}$ and $T_\beta \approx -40\,°\mathrm{C}$ the elastic modulus decreases stronger than in the mid-temperature regime between T_β and T_g before decreasing drastically above glass transition. For the electrical resistance, the overall semiconducting behavior decreases the measured resistance in similar stages, besides the rapid decrease above T_g being shifted higher by about 25 K.

6.3 Conclusion on CNP Nanocomposites Aptitude as Temperature Sensors

Addressing the Research Questions

Of all CNP morphologies, only the CNT showed repeatable resistive behavior over temperature. For three different CNT types, the resistivity shows a clear dependence on filler content of the nanocomposite. For SWCNT the residual metal catalyst content in T75 increases the conductivity for identical filler content by one order of magnitude in comparison to purified T99.

SWCNT composites show reversible negative temperature coefficients of resistance (NTC) temperature sensing behavior spanning both β and glass transition temperature of the matrix after more than four repeated cycles of thermal loading. Their resistance decreases exponentially with increasing temperature. Within the first three cycles in the used test-setup two different sections can be distinguished, the second segment starts around glass transition. After repeated cycling thermal loading (cycle 3 and further), this change in behavior is shifted to T_g+25 °C until reaching a stable response. This change in behavior can be attributed to decreasing contact resistance due to softening of the nanocomposites above T_g which leads to the spring loaded contacts being pressed into the nanocomposite. Once the full material contact is established the cyclic response of SWCNT nanocomposites is reversible. The response of 0.1 wt% Tuball 75 SWCNT in 828LVEL epoxy resin is heating rate independent between 1–10 K/min spanning both transition temperatures of the matrix. The application as a temperature sensor is promising since monotone NTC behavior has been observed mostly independent of the matrix behavior.

MWCNT exhibit PTC and NTC behavior in different temperature regions in initial thermal cycling up to three repetitions. The PTC behavior then diminishes with increasing cycle number until it stabilizes. The stable behavior is qualitatively similar to the three stages of a doped semiconductor after several cycles of thermal loading. A similarity to the elastic mechanical response can also be seen, with the transition temperatures of the resistive response being shifted higher by about 25 °C.

In general, a connection between mechanical and resistive behavior in the low-temperature range could not be observed. Curves of elastic modulus and resistance follow similar regions of decrease with increasing temperature. However, the glass transition is not the critical temperature for resistance decrease, since the resistive behavior changes about 25 °C above T_g.

Intrinsic semiconductor properties of the interconnected nanoparticle network dominate the electrical conductivity. Therefore, the CNT particle network is not able to sense matrix changes induced purely by temperature changes and can thus not be employed as an NDT method for thermal characterization. Therefore, the sensors found within this thesis are suitable to detect temperatures that span a temperature range of −100 °C to 170 °C.

7 Conclusion and Outlook

Following the production line of carbon nanocomposites via three-roll milling, three topics have been addressed within this thesis. Starting with nano-intermediate production, the first topic investigated process monitoring. The transfer of impedance measurement from off-line characterization to in-line monitoring tool for three-roll mill dispersion processes was achieved. Four carbon nano-particle types with different morphology could be distinguished based on their characteristic electrode-wetting behavior and absolute impedance values. In combination with line force interpretation sufficient quality monitoring was found. This can improve large-scale manufacturing quality significantly. Characteristic signals over processing time were discussed and feature values like the separation factor, mean line force and complex impedance showed the dispersion state. Resulting from that, superfluous dispersion steps could be identified to shorten passages and make nano-intermediate production more efficient. In future research, the continuous large-scale production has to be further investigated to test the in-line monitoring methods with continuous material flow. This will also show if the proposed production line of several three-roll mills is able to produce the high-concentration masterbatch within limited steps. The dynamic mode with line force-regulated gap adjustment is promising to avoid material separation which has been proven to be the most critical phenomenon in SWCNT dispersion processes. The resulting re-agglomerate and compaction of nanoparticles, as well as deposition on the rollers, has to be prevented to stabilize a large-scale dispersion process. For the impedance measuring system further adjustment, material-dependent calibration or extension of the low-impedance measuring range would give further valuable insight. The in-line monitoring can be used for other electrically conducting material systems expanding the presented carbon nano-intermediates to e.g. metal or metal-oxide filled polymeric coatings and inks. Globular particles showed the best wetting behavior of the interdigitated electrode.

Permanent magnetic manipulation has been proven to be difficult using solely as-received CNT without magnetic modification. The successful manipulation

results in the literature mostly report on a high content of magnetic catalyst residuals or additionally attached magnetic particles. This is the conclusion of conducted experiments within this thesis, too. The magnetic attraction of Tuball SWCNT with iron-containing catalyst residuals and NC7000 MWCNT in low-viscous media like water and ethanol was observed. The increased particle network stability of well-separated nanotubes in dispersions has been shown to withstand magnetic forces. The higher viscosity of resin systems hinders most particle movement within the pot-life, since manipulation takes several days and thus makes the method unfavorable for coating applications. Since strong electromagnetic fields have been reported to be more effective, that could be an approach to follow up on this idea. A movable electromagnet could be used to scan composite surfaces and locally manipulate the particle concentration. Literature and first pre-experiments make clear that precise fine-tuning of the magnetic field is necessary to influence coatings or open mold composites. A magnetic modification of carbon nano-particles is highly recommended because their intrinsic magnetic properties are weak and magnetic catalyst residuals vary in amount and position on or within the tubes. Iron oxides or nickel nanoparticles are recommended in literature due to their strong ferromagnetic response. Iron filings showed re-location and re-orientation in a manner that was hoped to be achieved for SWCNT to reinforce polymer composites with tailored concentration gradients or specific anisotropy. Gradient fields have been proven to be most effective for re-location of particles. Homogeneous strong fields induce the necessary magnetic moment to change particle orientation and thus achieve particle alignment.

Finally, the temperature sensing experiments have shown the promising outcome of SWCNT nanocomposites as sensors spanning β-transition and glass transition temperature between $-100\,^{\circ}\mathrm{C}$ and $170\,^{\circ}\mathrm{C}$. The nanocomposites show reproducible stable sensing behavior as negative temperature coefficient thermistors, which could be integrated into polymer composites easily. The resistive behavior is dominated by the intrinsic semiconductor properties of the fully formed nanoparticle network and is only marginally impacted by the glass transition temperature of the matrix. Metal catalyst residuals within T75 SWCNT have been found to increase overall conductivity while also increasing the measurable resistance changes in comparison to purified T99. MWCNT could be used as low-temperature sensors between $-100\,^{\circ}\mathrm{C}$ and $0\,^{\circ}\mathrm{C}$. In mid- to high-temperature range, their behavior is non-monotone, making the sensor application not suitable. All measurements have been conducted without additional mechanical load on the nanocomposite. A combination of structural health monitoring and tem-

perature sensing could thus be investigated in the future to distinguish resistance changes induced by mechanical and thermal loading. In glass fiber reinforced composites this could be researched further to distinguish structural damage and temperature changes. For electrically conductive carbon fibers the interaction of matrix and fibers in the electrical measurements has to be explored. A combination of resistive and capacitive measurements seems suitable to distinguish crack formation and NTC resistive behavior due to temperature changes.

Bibliography

[1] Hauke Meeuw et al. “Carbon Nanoparticles’ Impact on Processability and Physical Properties of Epoxy Resins-A Comprehensive Study Covering Rheological, Electrical, Thermo-Mechanical, and Fracture Properties (Mode I and II)”. In: *Polymers* 11.2 (2019). DOI: 10.3390/polym11020231.

[2] Hauke Voormann. “Smart dispersion of carbon nanoparticle epoxy composites: from nano to application”. PhD thesis. TUHH Universitätsbibliothek, 2021. DOI: 10.15480/882.3483.

[3] Dieter Meschede. *Gerthsen Physik*. Berlin, Heidelberg: Springer Berlin Heidelberg, 2010. ISBN: 978-3-642-12893-6. DOI: 10.1007/978-3-642-12894-3.

[4] Günter Gottstein. *Physikalische Grundlagen der Materialkunde: Mit 28 Tabellen*. 3. Aufl. Springer-Lehrbuch. Berlin and Heidelberg: Springer, 2007. ISBN: 978-3-540-71104-9.

[5] Jürgen Eichler. *Physik: Für das Ingenieurstudium - prägnant mit knapp 300 Beispielaufgaben ; mit 48 Tabellen*. 4., aktualisierte und überarbeitet Auflage. Naturwissenschaftliche Grundlagen. Wiesbaden: Vieweg + Teubner, 2011. ISBN: 978-3-83481272-8.

[6] Yu. F. Deinega and G. V. Vinogradov. “Electric fields in the rheology of disperse systems”. In: *Rheologica Acta* 23.6 (1984), pp. 636–651. ISSN: 1435-1528. DOI: 10.1007/BF01438804.

[7] D. G. Bekas and A. S. Paipetis. “Damage monitoring in nanoenhanced composites using impedance spectroscopy”. In: *Composites Science and Technology* 134 (2016), pp. 96–105. ISSN: 0266-3538. DOI: 10.1016/j.compscitech.2016.08.013.

[8] Hamed Tanabi and Merve Erdal. “Effect of CNTs dispersion on electrical, mechanical and strain sensing properties of CNT/epoxy nanocomposites”. In: *Results in Physics* 12 (2019), pp. 486–503. ISSN: 2211-3797. DOI: 10.1016/j.rinp.2018.11.081.

[9] Christina Buggisch. “Structurally compatible embedded sensors for damage detection in glass fibre reinforced polymers”. Dissertation. Hamburg: TUHH, 2022. URL: https://doi.org/10.15480/882.4557.

[10] Olfa Kanoun, ed. *Impedance Spectroscopy*. De Gruyter, 2018. ISBN: 978-3-11-055892-0. DOI: 10.1515/9783110558920.

[11] Stephen D. Senturia. *Fabrication and Evaluation of Polymeric Early-Warning*. Ed. by Department of Electrical Engineering and Computer Science, Cambridge, Mass. 1975.

[12] S. D. Senturia, C. M. Sechen, and J. A. Wishneusky. “The charge–flow transistor: A new MOS device”. In: *Applied Physics Letters* 30.2 (1977), pp. 106–108. ISSN: 0003-6951. DOI: 10.1063/1.89306.

[13] Stephen D. Senturia et al. *The feasibility of electrical monitoring of resin cure*. Ed. by Department of Electrical Engineering and Computer Science, Cambridge, Mass. 1979.

[14] Stephen D. Senturia et al. “The feasibility of electrical monitoring of resin cure with the charge-flow transistor”. In: *Polymer Engineering and Science* 21.2 (1981), pp. 113–118. URL: https://doi.org/10.1002/pen.760210210.

[15] Norman F. Sheppard et al. “Microdielectrometry”. In: *Sensors and Actuators* 2 (1982), pp. 263–274.

[16] Matthijs W. den Otter. “Approximate expressions for the capacitance and electrostatic potential of interdigitated electrodes”. In: *Sensors and Actuators A: Physical* 96.96 (2002), pp. 140–144. ISSN: 0924-4247.

[17] Rui Igreja, J. N. Marat-Mendes, and C. J. Dias, eds. *Dielectric characterization of PEBA and PDMS for capacitive interdigital vapour sensors*. Vol. 30. Norges nasjonallitteratur. IEEE, 2002. ISBN: 0-7803-7560-2.

[18] Rui Igreja and C. J. Dias. “Analytical evaluation of the interdigital electrodes capacitance for a multi-layered structure”. In: *Sensors and Actuators A: Physical* 112.2-3 (2004), pp. 291–301. ISSN: 0924-4247. DOI: 10.1016/j.sna.2004.01.040.

[19] H.-E. Endres and S. Drost. “Optimization of the Geometry of Gas-sensitive Interdigital Capacitors”. In: *Sensors and Actuators B* 4 (1991), pp. 95–98.

[20] Philip A. von Guggenberg. “Applications of Interdigital Dielectrometry to Moisture and Double Layer Measurements in Transformer Insulation”. Dissertation. Cambridge: Massachusetts Institute of Technology, 1993.

[21] Alexander V. Mamishev. “Interdigital Dielectrometry Sensor Design and Parameter Estimation Algorithms for Non-Destructive Materials Evaluations”. Dissertation. Cambridge: Massachusetts Institute of Technology, 1999.

[22] A. V. Mamishev et al. “Interdigital sensors and transducers”. In: *Proceedings of the IEEE* 92.5 (2004), pp. 808–845. ISSN: 0018-9219. DOI: 10.1109/JPROC.2004.826603.

[23] B. C. Lesieutre et al. “Forward and inverse parameter estimation algorithms of interdigital dielectrometty sensors”. In: *IEEE Transactions on Dielectrics and Electrical Insulation* 8.4 (2001), pp. 577–588.

[24] Yanko Sheiretov. “Deep Penetration Magnetostatic Sensors”. Dissertation. Cambridge: Massachusetts Institute of Technology, 2001.

[25] Zi Ping Wu et al. “Electromagnetic interference shielding of carbon nanotube macrofilms”. In: *Scripta Materialia* 64.9 (2011), pp. 809–812. ISSN: 1359-6462. DOI: 10.1016/j.scriptamat.2011.01.002.

[26] Aidin Mehdipour et al. “Multiwall Carbon Nanotube–Epoxy Composites With High Shielding Effectiveness for Aeronautic Applications”. In: *IEEE Transactions on Electromagnetic Compatibility* 54.1 (2012), pp. 28–36. ISSN: 0018-9375. DOI: 10.1109/TEMC.2011.2174241.

[27] Rudolf Gross, Achim Marx, and Dietrich Einzel. *Festkörperphysik: Aufgaben und Lösungen*. München: Oldenbourg Verlag, 2014. ISBN: 978-3-48677134-3.

[28] Alkis Paipetis and V. Kostopoulos. *Carbon nanotube enhanced aerospace composite materials: A new generation of multifunctional hybrid structural composites*. Vol. 188. Solid mechanics and its applications. Dordrecht and New York: Springer, 2013. ISBN: 978-9-40074245-1.

[29] J. Keith Nelson. *Dielectric Polymer Nanocomposites*. Boston, MA: Springer US, 2010. ISBN: 978-1-4419-1590-0. DOI: 10.1007/978-1-4419-1591-7.

[30] Satoru Kaneko et al., eds. *Carbon Related Materials: Commemoration for Nobel Laureate Professor Suzuki Special Symposium at IUMRS-ICAM2017*. 1st ed. 2021. Singapore: Springer Singapore and Imprint Springer, 2021. ISBN: 978-9-81157610-2. DOI: 10.1007/978-981-15-7610-2.

[31] Elham Asadian, Masoumeh Ghalkhani, and Saeed Shahrokhian. “Electrochemical sensing based on carbon nanoparticles: A review”. In: *Sensors and Actuators B: Chemical* 293 (2019), pp. 183–209. ISSN: 0925-4005. DOI: 10.1016/j.snb.2019.04.075.

[32] I. Balberg et al. “Excluded volume and its relation to the onset of percolation”. In: *Physical Review B* 30.7 (1984), pp. 3933–3943. ISSN: 1098-0121. DOI: 10.1103/PhysRevB.30.3933.

[33] Muhammad Sahimi and Allen G. Hunt, eds. *Complex Media and Percolation Theory*. Springer eBook Collection. New York, NY: Springer US, 2021. ISBN: 978-1-07161457-0. DOI: 10.1007/978-1-0716-1457-0.

[34] Xiao-Yong Fang et al. “Temperature- and thickness-dependent electrical conductivity of few-layer graphene and graphene nanosheets”. In: *Physics Letters A* 379.37 (2015), pp. 2245–2251. ISSN: 0375-9601. DOI: 10.1016/j.physleta.2015.06.063.

[35] I. Balberg. “A comprehensive picture of the electrical phenomena in carbon black–polymer composites”. In: *Carbon* 40 (2002), pp. 139–143. ISSN: 0008-6223. URL: https://doi.org/10.1016/S0008-6223(01)00164-6.

[36] Miguel A.S. Matos et al. “Predictions of the electro-mechanical response of conductive CNT-polymer composites”. In: *Journal of the Mechanics and Physics of Solids* 114 (2018), pp. 84–96. ISSN: 0022-5096. DOI: 10.1016/j.jmps.2018.02.014.

[37] Yang Wang et al. “A continuum model with a percolation threshold and tunneling-assisted interfacial conductivity for carbon nanotube-based nanocomposites”. In: *JOURNAL OF APPLIED PHYSICS* 115.19 (2014), p. 193706. DOI: 10.1063/1.4878195.

[38] Yasser Zare and Kyong Yop Rhee. “A simple model for electrical conductivity of polymer carbon nanotubes nanocomposites assuming the filler properties, interphase dimension, network level, interfacial tension and tunneling distance”. In: *Composites Science and Technology* 155 (2018), pp. 252–260. ISSN: 0266-3538. DOI: 10.1016/j.compscitech.2017.10.007.

[39] J. White, S. K. De, and K. Naskar. *Rubber Technologist’s Handbook Volume 2*. Vol. 2. Shrawsbury: Smithers Rapra Techn, 2009. ISBN: 978-1-84735100-5.

[40] Jean-Baptiste Donnet, ed. *Carbon Black : Science and Technology*. 2. New York: CRC Press, Marcel Dekker Inc., 1993. ISBN: 978-0-82478975-6.

[41] M. A. Short and Walker, P. L. “Measurement of interlayer spacing and crystal sizes in turbostatic carbons”. In: *Carbon* 1.1 (1963), pp. 3–9. ISSN: 0008-6223. URL: https://doi.org/10.1016/0008-6223(63)90003-4 (visited on 06/13/2023).

[42] Walker, P. L. “Carbon - An Old But New Material”. In: *American Scientist* 50.2 (1962), pp. 259–293. URL: http://www.jstor.org/stable/27838394.

[43] Avrom I. Medalia. “Electrical Conduction in Carbon Black Composites”. In: *Rubber Chemistry and Technology* 59.3 (1958), pp. 432–454. URL: https://doi.org/10.5254/1.3538209.

[44] E. K. Sichel, J. I. Gittleman, and Ping Sheng. “Electrical properties of carbon-polymer composites”. In: *Journal of Electronic Materials* 11.4 (1982), pp. 699–747. URL: https://doi.org/10.1007/BF02672392.

[45] Tejraj M. Aminabhavi, Patrick E. Cassidy, and Corley M. Thompson. “Electrical Resistivity of Carbon Black Loaded Rubbers”. In: *Rubber Chemistry and Technology* 63 (1990), pp. 451–471. URL: https://doi.org/10.5254/1.3538265.

[46] S. Mrozowski and A. Chaberski. “Hall effect and magnetoresistivity in carbons and polycrystalline graphites”. In: *Physical Review A* 104.1 (1956), pp. 74–83. ISSN: 1050-2947. URL: https://doi.org/10.1103/PhysRev.104.74.

[47] Ramesh T. Subramaniam et al., eds. *Graphene: Fabrication, Properties and Applications*. 1st ed. 2023. Engineering Materials. Singapore: Springer Nature Singapore and Imprint Springer, 2023. ISBN: 978-9-81991206-3. DOI: 10.1007/978-981-99-1206-3.

[48] Tianrong Zhang. *Graphene: From Theory to Applications*. 1st ed. 2022. Springer eBook Collection. Singapore: Springer Singapore and Imprint Springer, 2022. ISBN: 978-9-81164589-1. DOI: 10.1007/978-981-16-4589-1.

[49] Linlin Zhang et al. “Advanced nanostructured carbon-based materials for rechargeable lithium-sulfur batteries”. In: *Carbon* 141 (2019), pp. 400–416. ISSN: 0008-6223. DOI: 10.1016/j.carbon.2018.09.067.

[50] Changgu Lee et al. “Measurement of the elastic properties and intrinsic strength of monolayer graphene”. In: *Science (New York, N.Y.)* 321.5887 (2008), pp. 385–388. DOI: 10.1126/science.1157996.

[51] Jean-Noel Fuchs and Mark Oliver Goerig. “Introduction to the Physical Properties of Graphene”. 2008. URL: https://web.physics.ucsb.edu/~phys123B/w2015/pdf_CoursGraphene2008.pdf.

[52] Tetsuya Tohei et al. “Debye temperature and stiffness of carbon and boron nitride polymorphs from first principles calculations”. In: *Physical Review B* 73.6 (2006). ISSN: 1098-0121. DOI: 10.1103/PhysRevB.73.064304.

[53] Melina K. Blees et al. “Graphene kirigami”. In: *Nature* 524.7564 (2015), pp. 204–207. DOI: 10.1038/nature14588.

[54] L. Selva Roselin et al. “Recent Advances and Perspectives of Carbon-Based Nanostructures as Anode Materials for Li-ion Batteries”. In: *Materials (Basel, Switzerland)* 12.8 (2019). ISSN: 1996-1944. DOI: 10.3390/ma12081229.

[55] Eric Pop, Vikas Varshney, and Ajit K. Roy. “Thermal properties of graphene: Fundamentals and applications”. In: *MRS Bulletin* 37.12 (2012), pp. 1273–1281. ISSN: 0883-7694. DOI: 10.1557/mrs.2012.203.

[56] Weiqing Fang, Hwi W. Jang, and Siu N. Leung. “Evaluation and modelling of electrically conductive polymer nanocomposites with carbon nanotube networks”. In: *Composites Part B: Engineering* 83 (2015), pp. 184–193. ISSN: 1359-8368. DOI: 10.1016/j.compositesb.2015.08.047.

[57] L. Pietronero et al. “Electrical conductivity of a graphite layer”. In: *Physical Review B* 22.2 (1980), pp. 904–910. ISSN: 1098-0121. DOI: 10.1103/PhysRevB.22.904.

[58] Jiahua Zhu et al. “Magnetic field induced capacitance enhancement in graphene and magnetic graphene nanocomposites”. In: *Energy Environ. Sci.* 6.1 (2013), pp. 194–204. ISSN: 1754-5692. DOI: 10.1039/C2EE23422J.

[59] Xin Sun et al. “Laminated magnetic graphene with enhanced electromagnetic wave absorption properties”. In: *J. Mater. Chem. C* 1.4 (2013), pp. 765–777. ISSN: 2050-7526. DOI: 10.1039/C2TC00159D.

[60] Nujiang Tang et al. “Magnetic properties of graphene”. In: *Spintronic 2D Materials*. Elsevier, 2020, pp. 137–161. ISBN: 978-0-08102154-5. DOI: 10.1016/B978-0-08-102154-5.00005-9.

[61] C. N. R. Rao et al. “Unusual magnetic properties of graphene and related materials”. In: *Chem. Sci.* 3.1 (2012), pp. 45–52. ISSN: 2041-6520. DOI: 10.1039/C1SC00726B.

[62] Ahmadreza Ghaffarkhah et al. “Synthesis, Applications, and Prospects of Graphene Quantum Dots: A Comprehensive Review”. In: *Small (Weinheim an der Bergstrasse, Germany)* 18.2 (2022), e2102683. DOI: 10.1002/smll.202102683.

[63] H. S. S. Ramakrishna Matte, K. S. Subrahmanyam, and C. N. R. Rao. "Novel magnetic properties of graphene: Presence of both ferromagnetic and antiferromagnetic features and other aspects". In: *The Journal of Physical Chemistry C* 133.23 (2014), pp. 9982–9985. ISSN: 1932-7447. URL: https://doi.org/10.1021/jp903397u.

[64] Yuchen Ma et al. "Magnetic properties of vacancies in graphene and single-walled carbon nanotubes". In: *New Journal of Physics* 6 (2004), p. 68. DOI: 10.1088/1367-2630/6/1/068.

[65] Ljubisa R. Radovic and Bradley Bockrath. "On the chemical nature of graphene edges: origin of stability and potential for magnetism in carbon materials". In: *Journal of the American Chemical Society* 127.16 (2005), pp. 5917–5927. ISSN: 1520-5126. DOI: 10.1021/ja050124h.

[66] Sumio Iijima. "Helical microtubules of graphitic carbon". In: *Letters to Nature* 1991.354 (), pp. 56–58. URL: https://doi.org/10.1038/354056a0.

[67] Sumio Iijima. "Helical microtubules of graphitic carbon". In: *Letters to Nature* 354 (1991), pp. 56–58. URL: https://doi.org/10.1038/354056a0.

[68] M. Endo and A. Oberlin. "Filamentous growth of carbon through benzene decomposition". In: *Journal of Crystal Growth* 32 (1976), pp. 335–349.

[69] Mildred S. Dresselhaus, Gene Dresselhaus, and Phaedon Avouris. *Carbon Nanotubes - Synthesis, Structure, Properties, and Applications*. 1st ed. Vol. 80. Topics in Applied Physics. Springer-Verlag Berlin Heidelberg, 2001. ISBN: 3-540-41086-4.

[70] Takeshi Akasaka, Fred Wudl, and Shigeru Nagase. *Chemistry of nanocarbons*. Chichester West Sussex: Wiley, 2010. ISBN: 978-0-47072195-7.

[71] Vikas Mittal, ed. *Polymer nanotube nanocomposites: Synthesis, properties, and applications*. 2nd edition. Wiley-Scrivener. Hoboken, New Jersey: John Wiley & Sons Inc, 2014. ISBN: 1118945921. DOI: 10.1002/9781118945964. URL: https://search.ebscohost.com/login.aspx?direct=true&scope=site&db=nlebk&db=nlabk&AN=838176.

[72] S. Reich, C. Thomsen, and J. Maultzsch. *Carbon Nanotubes*. 1st ed. Weinheim: WILEY-VCH Verlag GmbH & Co. KGaA, 2004. ISBN: 3-527-40386-8.

[73] Peter J.F. Harris. *Carbon Nanotubes and related structures: New Materials for the Twenty-first Century*. Cambridge: Cambridge University Press, 1999. ISBN: 0 521 55446 2.

[74] C. T. White, D. H. Robertson, and J. W. Mintmire. “Helical and rotational symmetries of nanoscale graphitic tubules”. In: *Physical Review B* 47.9 (1993), pp. 5485–5488. ISSN: 1098-0121. URL: https://doi.org/10.1103/PhysRevB.47.5485.

[75] T. W. Ebbesen et al. “Electrical conductivity of individual carbon nanotubes”. In: *Letters to Nature* 382 (1996), pp. 54–56. URL: https://doi.org/10.1038/382054a0.

[76] Lorin X. Benedict, Steven G. Louie, and Marvin L. Cohen. “Heat Capacity of Carbon Nanotubes”. In: *Solid State Communications* 100.3 (1996), pp. 177–180. URL: https://doi.org/10.1016/0038-1098(96)00386-9.

[77] J. W. Mintmire, B. I. Dunlap, and C. T. White. “Are fullerene tubules metallic?” In: *Physical review letters* 68.5 (1992), pp. 631–634. ISSN: 0031-9007. URL: https://doi.org/10.1103/PhysRevLett.68.631.

[78] Ralph Krupke et al. “Separation of metallic from semiconducting”. In: *Science (New York, N.Y.)* 301.5631 (2003), pp. 344–347. DOI: 10.1126/science.1086534.

[79] S. Reich, C. Thomsen, and P. Ordejón. “Electronic band structure of isolated and bundled carbon nanotubes”. In: *Physical Review B* 65.15 (2002). ISSN: 1098-0121. DOI: 10.1103/PhysRevB.65.155411.

[80] Dong Qian et al. “Mechanics of carbon nanotubes”. In: *Appl. Mech. Rev.* 55.336 (2002), pp. 495–533. DOI: 10.1115/1.1490129.

[81] Jian Ping Lu. “Elastic Properties of single and multilayered nanotubes”. In: *J. Phys. Chem. Solids* 58.11 (1997), pp. 1649–1652. URL: https://doi.org/10.1016/S0022-3697(97)00045-0.

[82] Satoru Suzuki. *Physical and Chemical Properties of Carbon Nanotubes*. InTech, 2013. ISBN: 978-953-51-1002-6. DOI: 10.5772/46029.

[83] Jian Ping Lu. “Novel Magnetic Properties of Carbon Nanotubes”. In: *Physical review letters* 74.7 (1995), pp. 1123–1126. ISSN: 0031-9007. DOI: 10.1103/PhysRevLett.74.1123. URL: https://link.aps.org/doi/10.1103/PhysRevLett.74.1123.

[84] Hiroshi Ajiki and Tsuneya Ando. “Magnetic Properties of Carbon Nanotubes”. In: *Journal of the Physical Society of Japan* 62.7 (1993), pp. 2470–2480. ISSN: 0031-9015. DOI: 10.1143/JPSJ.62.2470.

[85] A. Leonhardt et al. “Enhanced magnetism in Fe-filled carbon nanotubes produced by pyrolysis of ferrocene”. In: *JOURNAL OF APPLIED PHYSICS* 98 (2005). DOI: 10.1063/1.2058181. (Visited on 08/15/2019).

[86] Il Tae Kim and Rina Tannenbaum, eds. *Electronic Properties of Carbon Nanotubes*. Rijeka: IntechOpen, 2011.

[87] Frank Zoladz et al. "Enhanced magnetic properties of aluminum oxide nanopowder reinforced with carbon nanotubes". In: *Journal of Nanoparticle Research* 22.6 (2020). ISSN: 1388-0764. DOI: 10.1007/s11051-020-04896-6.

[88] Jie Ma et al. "One-pot, large-scale synthesis of magnetic activated carbon nanotubes and their applications for arsenic removal". In: *Journal of Materials Chemistry A* 1.15 (2013), pp. 4662–4666. ISSN: 2050-7488. DOI: 10.1039/C3TA10329C.

[89] G. Ariu, I. Hamerton, and D. Ivanov. "Positioning and aligning CNTs by external magnetic field to assist localised epoxy cure". In: *Open Physics* 14.1 (2016), pp. 508–516. DOI: 10.1515/phys-2016-0057. URL: https://www.degruyter.com/view/journals/phys/14/1/article-p508.xml.

[90] A. A. Ovchinnikov and V. V. Atrazhev. "Magnetic susceptibility of multilayered carbon nanotubes". In: *PHYSICS OF THE SOLID STATE* 40.10 (1998), p. 1769.

[91] P. Byszewski and M. Baran. "Magnetic Susceptibility of Carbon Nanotubes". In: *Europhysics Letters (EPL)* 31.7 (1995), pp. 363–366. ISSN: 0295-5075. DOI: 10.1209/0295-5075/31/7/004.

[92] Simone S. Alexandre, Mário S. C. Mazzoni, and Hélio Chacham. "Edge States and Magnetism in Carbon Nanotubes with Line Defects". In: *Physical review letters* 100.14 (2008), p. 146801. ISSN: 0031-9007. DOI: 10.1103/PhysRevLett.100.146801. URL: https://link.aps.org/doi/10.1103/PhysRevLett.100.146801.

[93] Belle Dumé. *Carbon nanotubes go magnetic*. 2004. URL: https://physicsworld.com/a/carbon-nanotubes-go-magnetic/ (visited on 08/15/2019).

[94] O. Céspedes et al. "Contact induced magnetism in carbon nanotubes". In: *Journal of Physics: Condensed Matter* 16.10 (2004), pp. L155–L161. ISSN: 0953-8984. DOI: 10.1088/0953-8984/16/10/L06.

[95] Bharat Bhushan. *Encyclopedia of Nanotechnology*. Dordrecht: Springer Netherlands, 2012. ISBN: 978-90-481-9750-7. DOI: 10.1007/978-90-481-9751-4.

[96] Günter Jakob Lauth and Jürgen Kowalczyk. *Einführung in die Physik und Chemie der Grenzflächen und Kolloide*. Berlin, Heidelberg: Springer Berlin Heidelberg, 2016. ISBN: 978-3-662-47017-6. DOI: 10.1007/978-3-662-47018-3.

[97] Abderrahim Boudenne. *Handbook of multiphase polymer systems*. Hoboken NJ: Wiley, 2011. ISBN: 978-0-47071420-1.

[98] Yuncheng Liang et al. "Interaction forces between colloidal particles in liquid: theory and experiment". In: *Advances in colloid and interface science* 134-135 (2007), pp. 151–166. ISSN: 0001-8686. DOI: 10.1016/j.cis.2007.04.003.

[99] João Paulo Vita Damasceno and Lauro Tatsuo Kubota. "Colloidal chemistry as a guide to design intended dispersions of carbon nanomaterials". In: *Materials Today Chemistry* 21 (2021), p. 100526. ISSN: 2468-5194. DOI: 10.1016/j.mtchem.2021.100526.

[100] Amit K. Chakraborty et al. "Carbon nanotube (CNT)–epoxy nanocomposites: a systematic investigation of CNT dispersion". In: *Journal of Nanoparticle Research* 13.12 (2011), pp. 6493–6506. ISSN: 1388-0764. DOI: 10.1007/s11051-011-0552-3.

[101] Carolin Heintz. *Über die Auswirkung von Scherbelastung auf das rheologische und elektrische Verhalten von Kohlenstoffnanorohrchen/Epoxid Suspensionen: Dissertation*. Hamburg, 2012.

[102] Carsten Schilde et al. "Effect of fluid–particle-interactions on dispersing nano-particles in epoxy resins using stirred-media-mills and three-roll-mills". In: *Composites Science and Technology* 70.4 (2010), pp. 657–663. ISSN: 0266-3538. DOI: 10.1016/j.compscitech.2009.12.021.

[103] Matthias Heimann et al. "Investigations of carbon nanotubes epoxy composites for electronics packaging". In: *2008 58th Electronic Components and Technology Conference*. IEEE, 2008, pp. 1731–1736. ISBN: 978-1-4244-2230-2. DOI: 10.1109/ECTC.2008.4550214.

[104] Mahesh Hosur et al. "Effect of processing techniques on the performance of Epoxy/MWCNT nanocomposites". In: *Journal of Applied Polymer Science* 127.6 (2013), pp. 4211–4224. ISSN: 0021-8995. DOI: 10.1002/app.37990.

[105] Young Seok Song and Jae Ryoun Youn. "Influence of dispersion states of carbon nanotubes on physical properties of epoxy nanocomposites". In: *Carbon* 43.7 (2005), pp. 1378–1385. ISSN: 0008-6223. DOI: 10.1016/j.carbon.2005.01.007.

[106] R. Kotsilkova, D. Fragiadakis, and P. Pissis. "Reinforcement effect of carbon nanofillers in an epoxy resin system: Rheology, molecular dynamics, and mechanical studies". In: *Journal of Polymer Science Part B: Polymer Physics* 43.5 (2005), pp. 522–533. ISSN: 0887-6266. DOI: 10.1002/polb.20352.

[107] Benjamin Zanghellini et al. "Solvent-Free Ultrasonic Dispersion of Nanofillers in Epoxy Matrix". In: *Polymers* 13.2 (2021). DOI: 10.3390/polym13020308.

[108] Olivier Cohu and Albert Magnin. "Rheometry of paints with regard to roll coating process". In: *Journal of Rheology* 39.4 (1995), pp. 767–785. ISSN: 0148-6055. DOI: 10.1122/1.550656.

[109] Jan Sumfleth, Samuel T. Buschhorn, and Karl Schulte. "Comparison of rheological and electrical percolation phenomena in carbon black and carbon nanotube filled epoxy polymers". In: *Journal of Materials Science* 46.3 (2011), pp. 659–669. ISSN: 0022-2461. DOI: 10.1007/s10853-010-4788-6.

[110] Ji-Hwan Ha, Sang-Eui Lee, and Sung-Hoon Park. "Effect of Dispersion by Three-Roll Milling on Electrical Properties and Filler Length of Carbon Nanotube Composites". In: *Materials (Basel, Switzerland)* 12.23 (2019). ISSN: 1996-1944. DOI: 10.3390/ma12233823.

[111] Bao Le et al. "Micro-end-milling of carbon nanotube reinforced epoxy nanocomposites manufactured using three roll mill technique". In: *Journal of Manufacturing Processes* 70 (2021), pp. 307–320. ISSN: 1526-6125. DOI: 10.1016/j.jmapro.2021.08.048.

[112] Yan Li et al. "Optimization of Three-Roll Mill Parameters for In-Situ Exfoliation of Graphene". In: *MRS Advances* 1.19 (2016), pp. 1389–1394. DOI: 10.1557/adv.2016.191.

[113] Iosif D. Rosca and Suong V. Hoa. "Highly conductive multiwall carbon nanotube and epoxy composites produced by three-roll milling". In: *Carbon* 47.8 (2009), pp. 1958–1968. ISSN: 0008-6223. DOI: 10.1016/j.carbon.2009.03.039.

[114] Peng-Cheng Ma et al. “Dispersion and functionalization of carbon nanotubes for polymer-based nanocomposites: A review”. In: *Composites Part A: Applied Science and Manufacturing* 41.10 (2010), pp. 1345–1367. ISSN: 1359-835X. DOI: 10.1016/j.compositesa.2010.07.003.

[115] Jenny Hilding et al. “Dispersion of Carbon Nanotubes in Liquids”. In: *Journal of Dispersion Science and Technology* 24.1 (2003), pp. 1–41. ISSN: 0193-2691. DOI: 10.1081/DIS-120017941. URL: http://dx.doi.org/10.1081/DIS-120017941.

[116] Hauke Meeuw et al. “Smart dispersion: Validation of OCT and impedance spectroscopy as solutions for in-situ dispersion analysis of CNP/EP-composites”. In: *Materialia* 1 (2018), pp. 185–197. ISSN: 2589-1529. DOI: 10.1016/j.mtla.2018.06.002.

[117] Hauke Meeuw et al. “Carbon Nanoparticles’ Impact on Processability and Physical Properties of Epoxy Resins-A Comprehensive Study Covering Rheological, Electrical, Thermo-Mechanical, and Fracture Properties (Mode I and II)”. In: *Polymers* 11.2 (2019). DOI: 10.3390/polym11020231.

[118] Hauke Meeuw, Valea K. Wisniewski, and Bodo Fiedler. “Frequency or Amplitude? - Rheo-Electrical Characterization of Carbon Nanoparticle Filled Epoxy Systems”. In: *Polymers* 10.9 (2018). DOI: 10.3390/polym10090999.

[119] A. Battisti, A. A. Skordos, and I. K. Partridge. “Monitoring dispersion of carbon nanotubes in a thermosetting polyester resin”. In: *Composites Science and Technology* 69.10 (2009), pp. 1516–1520. ISSN: 0266-3538. DOI: 10.1016/j.compscitech.2008.05.012.

[120] José A. Covas and Maria C. Paiva, eds. *Processing of Polymer Nanocomposites: Monitoring dispersion and reagglomeration phenomena during the manufacture of polymer nanocomposites*. Carl Hanser Verlag GmbH & Company KG, 2019. ISBN: 9781569906361. URL: http://repositorium.uminho.pt/bitstream/1822/71810/1/chapter%209.pdf.

[121] Manuel V. C. Morais et al. “Process Chain Optimization for SWCNT/Epoxy Nanocomposite Parts with Improved Electrical Properties”. In: *Journal of Composites Science* 4.3 (2020), p. 114. DOI: 10.3390/jcs4030114.

[122] Sonja Carolin Schulz, Jana Schlutter, and Wolfgang Bauhofer. "Influence of Initial High Shearing on Electrical and Rheological Properties and Formation of Percolating Agglomerates for MWCNT/Epoxy Suspensions". In: *Macromolecular Materials and Engineering* 295.7 (2010), pp. 613–617. ISSN: 1438-7492. DOI: 10.1002/mame.201000065.

[123] S. C. Schulz et al. "Combined electrical and rheological properties of shear induced multiwall carbon nanotube agglomerates in epoxy suspensions". In: *European Polymer Journal* 47.11 (2011), pp. 2069–2077. ISSN: 0014-3057. DOI: 10.1016/j.eurpolymj.2011.07.022.

[124] C. A. Martin et al. "Electric field-induced aligned multi-wall carbon nanotube networks in epoxy composites". In: *Polymer* 46.3 (2005), pp. 877–886. ISSN: 0032-3861. DOI: 10.1016/j.polymer.2004.11.081.

[125] Ali Mohammad Amani et al. "Electric Field Induced Alignment of Carbon Nanotubes: Methodology and Outcomes". In: *Carbon Nanotubes - Recent Progress*. Ed. by Mohammed Muzibur Rahman and Abdullah Mohamed Asiri. InTech, 2018. ISBN: 978-1-78923-052-9. DOI: 10.5772/intechopen.70481.

[126] Konstantin Iakoubovskii. "Techniques of aligning carbon nanotubes". In: *Open Physics* 7.4 (2009). DOI: 10.2478/s11534-009-0072-2.

[127] Marco Monti et al. "The alignment of single walled carbon nanotubes in an epoxy resin by applying a DC electric field". In: *Carbon* 50.7 (2012), pp. 2453–2464. ISSN: 0008-6223. DOI: 10.1016/j.carbon.2012.01.067.

[128] Mizuki Shoyama and Shuji Matsusaka. "Agglomeration and Dispersion Related to Particle Charging in Electric Fields". In: *KONA Powder and Particle Journal* 38.0 (2021), pp. 82–93. ISSN: 0288-4534. DOI: 10.14356/kona.2021016.

[129] C. B. W. Kerkdijk, R. P. A. R. van Kleef, and J. A. Roeterdink. "Magnetic Separation Research: A Survey of Some Activities in The Netherlands". In: *Magnetic Separation News* 1.3 (1984), pp. 123–138. ISSN: 0731-3632. DOI: 10.1155/1984/39671.

[130] Ngoc Do Quyen Chau et al. "Multifunctional carbon nanomaterial hybrids for magnetic manipulation and targeting". In: *Biochemical and biophysical research communications* 468.3 (2015), pp. 454–462. DOI: 10.1016/j.bbrc.2015.06.131.

[131] Oleksandr Buluy et al. “Magnetic sensitivity of a dispersion of aggregated ferromagnetic carbon nanotubes in liquid crystals”. In: *Soft Matter* 7.2 (2011), pp. 644–649. ISSN: 1744-683X. DOI: 10.1039/C0SM00131G.

[132] Mahdieh Yavari, Zahra Mansourpour, and Mojtaba Shariaty-Niassar. “Controlled assembly and alignment of CNTs in ferrofluid: Application in tunable heat transfer”. In: *Journal of Magnetism and Magnetic Materials* 479 (2019), pp. 170–178. ISSN: 0304-8853. DOI: 10.1016/j.jmmm.2019.01.078.

[133] Shreya Trivedi et al. “Effect of diazotization and magnetic assembly on CNT dispersion observed with hardness and modulus measurement of their epoxy composite of low CNT volume fraction”. In: *Journal of Nanoparticle Research* 21.12 (2019). ISSN: 1388-0764. DOI: 10.1007/s11051-019-4697-9.

[134] Hiroaki Yonemura et al. “Magnetic orientation of single-walled carbon nanotubes or their composites using polymer wrapping”. In: *Science and technology of advanced materials* 9.2 (2008), p. 024213. ISSN: 1468-6996. DOI: 10.1088/1468-6996/9/2/024213.

[135] B. K. Jang, Y. Sakka, and S. K. Woo. “Alignment of carbon nanotubes by magnetic fields and aqueous dispersion”. In: *Journal of Physics: Conference Series* 156 (2009), p. 012005. DOI: 10.1088/1742-6596/156/1/012005.

[136] Kaoru Tsuda and Yoshio Sakka. “Simultaneous alignment and micropatterning of carbon nanotubes using modulated magnetic field”. In: *Science and technology of advanced materials* 10.1 (2009), p. 014603. ISSN: 1468-6996. DOI: 10.1088/1468-6996/10/1/014603.

[137] Kamil Lipert et al. “Magnetic properties of carbon nanotubes with and without catalyst”. In: *Journal of Physics: Conference Series* 200.7 (2010), p. 072061. DOI: 10.1088/1742-6596/200/7/072061.

[138] Hassan Mahfuz et al. “Reinforcement of SC-15 epoxy with CNT/CNF under high magnetic field: an investigation of mechanical and thermal response”. In: *Journal of Materials Science* 44.4 (2009), pp. 1113–1120. ISSN: 0022-2461. DOI: 10.1007/s10853-008-3161-5.

[139] Chuanguo Ma et al. “Fracture resistance, thermal and electrical properties of epoxy composites containing aligned carbon nanotubes by low magnetic field”. In: *Composites Science and Technology* 114 (2015), pp. 126–135. ISSN: 0266-3538. DOI: 10.1016/j.compscitech.2015.04.007. URL: http://www.sciencedirect.com/science/article/pii/S0266353815001657.

[140] B. Ellis. *Chemistry and Technology of Epoxy Resins*. Dordrecht: Springer Science+Business Media, 1993. ISBN: 978-94-010-5302-0.

[141] Edward M. Petrie. *Epoxy adhesive formulations*. New York: McGraw-Hill, 2006. ISBN: 9780071589086.

[142] Jean-Pierre Pascault and R. J. J. Williams, eds. *Epoxy polymers: New materials and innovations*. Weinheim: Wiley-VCH, 2010. ISBN: 1282472291. DOI: 10.1002/9783527628704. URL: https://onlinelibrary.wiley.com/doi/book/10.1002/9783527628704.

[143] D. H. Kaelble. "Dynamic and tensile properties of epoxy resins". In: *Journal of Applied Polymer Science* 9.4 (1965), pp. 1213–1225. ISSN: 0021-8995. DOI: 10.1002/app.1965.070090403.

[144] C. A. May and F. E. Weir. "Dynamic mechanical properties of epoxy resins". In: *Polymer Engineering and Science* 2.3 (1962), pp. 207–212. ISSN: 0032-3888. DOI: 10.1002/pen.760020306.

[145] Donald E. Kline. "Dynamic mechanical properties of polymerized epoxy resins". In: *Journal of Polymer Science* 47.149 (1960), pp. 237–249. ISSN: 0022-3832. DOI: 10.1002/pol.1960.1204714921.

[146] T. Murayama and J. P. Bell. "Relation between the network structure and dynamic mechanical properties of a typical amine-cured epoxy polymer". In: *Journal of Polymer Science Part A-2: Polymer Physics* 8.3 (1970), pp. 437–445. ISSN: 0449-2978. DOI: 10.1002/pol.1970.160080309.

[147] John B. Enns and John K. Gillham. "Effect of the extent of cure on the modulus, glass transition, water absorptio, and density of an amine-cured epoxy". In: *Journal of Applied Polymer Science* 28.9 (1983), pp. 2831–2846. ISSN: 0021-8995. DOI: 10.1002/app.1983.070280914.

[148] Julien Michels et al. "Glass transition evaluation of commercially available epoxy resins used for civil engineering applications". In: *Composites Part B: Engineering* 77 (2015), pp. 484–493. ISSN: 1359-8368. DOI: 10.1016/j.compositesb.2015.03.053.

[149] Alan J. Lesser and Emmett Crawford. "The role of network architecture on the glass transition temperature of epoxy resins". In: *Journal of Applied Polymer Science* 66.2 (1997), pp. 387–395. ISSN: 0021-8995. DOI: 10.1002/(SICI)1097-4628(19971010)66:2<387::AID-APP19>3.0.CO;2-V.

[150] Gottfried W. Ehrenstein, Gabriela Riedel, and Pia Trawiel. *Thermal Analysis of Plastics: Theory and Practice*. München: Hanser, 2004. ISBN: 978-3-446-22673-9. URL: https://www.hanser-elibrary.com/isbn/9783446226739.

[151] Wolfgang Grellmann, ed. *Kunststoffprüfung*. 2. Aufl. München: Hanser, 2011. ISBN: 3446427228.

[152] AVK – Industrievereinigung Verstärkte Kunststoffe e. V. *Handbuch Faserverbundkunststoffe/Composites*. Wiesbaden: Springer Fachmedien Wiesbaden, 2013. ISBN: 978-3-658-02754-4. DOI: 10.1007/978-3-658-02755-1.

[153] S. Sourour and M. R. Kamal. "Differential scanning calorimetry of epoxy cure: isothermal cure kinetics". In: *Thermochimica Acta* 14.1-2 (1976), pp. 41–59. DOI: 10.1016/0040-6031(76)80056-1.

[154] Ricky Hardis et al. "Cure kinetics characterization and monitoring of an epoxy resin using DSC, Raman spectroscopy, and DEA". In: *Composites Part A: Applied Science and Manufacturing* 49 (2013), pp. 100–108. ISSN: 1359-835X. DOI: 10.1016/j.compositesa.2013.01.021.

[155] R. A. Fava. "Differential Scanning Calometry of Epoxy Resins". In: *Polymer* 9 (1968), pp. 137–151. ISSN: 0032-3861. DOI: 10.1016/0032-3861(68)90024-4.

[156] Ursula T. Kreibich and Rolf Schmid. "Inhomogeneities in epoxy resin networks". In: *Journal of Polymer Science: Polymer Symposia* 53.1 (1975), pp. 177–185. ISSN: 0360-8905. DOI: 10.1002/polc.5070530122.

[157] Sophie Barrau et al. "Glass Transition Temperature Depression at the Percolation Threshold in Carbon Nanotube-Epoxy Resin and Polypyrrole-Epoxy Resin Composites". In: *Macromolecular Rapid Communications* 26.5 (2005), pp. 390–394. ISSN: 1022-1336. DOI: 10.1002/marc.200400515.

[158] P. R. N. Childs, J. R. Greenwood, and C. A. Long. "Review of temperature measurement". In: *Review of Scientific Instruments* 71.8 (2000), pp. 2959–2978. ISSN: 0034-6748. DOI: 10.1063/1.1305516.

[159] Herbert Bernstein. *Messelektronik und Sensoren*. Wiesbaden: Springer Fachmedien Wiesbaden, 2014. ISBN: 978-3-658-00548-1. DOI: 10.1007/978-3-658-00549-8.

[160] Ekbert Hering and Gert Schönfelder. *Sensoren in Wissenschaft und Technik*. Wiesbaden: Springer Fachmedien Wiesbaden, 2018. ISBN: 978-3-658-12561-5. DOI: 10.1007/978-3-658-12562-2.

[161] X. B. Chen, J.-P. Issi, and M. Cassart. "Temperature dependence of the conductivity in conducting polymer composites". In: *Polymer* 35.24 (1994), pp. 5256–5258. ISSN: 0032-3861.

[162] A. Di Bartolomeo et al. “Multiwalled carbon nanotube films as small-sized temperature sensors”. In: *JOURNAL OF APPLIED PHYSICS* 105.6 (2009), p. 064518. DOI: 10.1063/1.3093680.

[163] Q. Li et al. “Temperature dependence of the electrical properties of the carbon nanotube/polymer composites”. In: *Express Polymer Letters* 3.12 (2009), pp. 769–777. ISSN: 1788-618X. DOI: 10.3144/expresspolymlett.2009.95.

[164] Alejandra de La Vega et al. “Time and temperature dependent piezoresistance of carbon nanofiller/polymer composites under dynamic load”. In: *Journal of Materials Science* 47.6 (2012), pp. 2648–2657. ISSN: 0022-2461. DOI: 10.1007/s10853-011-6090-7.

[165] Alejandra de La Vega Oyervides, Karl Schulte, and Wolfgang Bauhofer. “Investigation of internal stress distribution of single-walled carbon nanotube/epoxy nanocomposites at curing and under mechanical load”. PhD thesis. Hamburg: TuTech Verl. URL: http://www.gbv.de/dms/tib-ub-hannover/733779727.pdf.

[166] Michael K. Njuguna et al. “Investigation on Temperature-Dependent Electrical Conductivity of Carbon Nanotube/Epoxy Composites for Sustainable Energy Applications”. In: *Journal of nanoscience and nanotechnology* 15.9 (2015), pp. 6957–6964. DOI: 10.1166/jnn.2015.10514.

[167] Amirhossein Biabangard Oskouyi, Uttandaraman Sundararaj, and Pierre Mertiny. “Effect of Temperature on Electrical Resistivity of Carbon Nanotubes and Graphene Nanoplatelets Nanocomposites”. In: *Journal of Nanotechnology in Engineering and Medicine* 5.4 (2014). ISSN: 1949-2944. DOI: 10.1115/1.4030018.

[168] Fei Xing et al. “Temperature Dependence of Electrical Resistance in Carbon Nanotube Composite Film during Curing Process”. In: *Nanomaterials (Basel, Switzerland)* 12.20 (2022). ISSN: 2079-4991. DOI: 10.3390/nano12203552.

[169] Bangwen Zhang, Baowei Li, and Changsheng Xie. “Epoxy Resin/Nano Ni@C Composites Exhibiting NTC Effect with Tunable Resistivity”. In: *Journal of Material Science and Technology* 25.2 (2009), pp. 159–163.

[170] Yılmaz Simsek et al. “Temperature dependence of electrical conductivity in double-wall and multi-wall carbon nanotube/polyester nanocomposites”. In: *Journal of Materials Science* 42.23 (2007), pp. 9689–9695. ISSN: 0022-2461. DOI: 10.1007/s10853-007-1943-9.

[171] Zhaohui Yang et al. “Composite Films Based on Aligned Carbon Nanotube Arrays and a Poly(N-Isopropyl Acrylamide) Hydrogel”. In: *Advanced Materials* 20.11 (2008), pp. 2201–2205. ISSN: 0935-9648. DOI: 10.1002/adma.200701964.

[172] Malte Hendrik Georg Wichmann. “Electrically conductive polymer nanocomposite matrix systems with load and health monitoring capabilities”. Dissertation. Hamburg: TUHH Technische Universität Hamburg, 2009.

[173] Piero Malcovati et al. *Sensors and Microsystems*. Vol. 54. Dordrecht: Springer Netherlands, 2010. ISBN: 978-90-481-3605-6. DOI: 10.1007/978-90-481-3606-3.

[174] Heinz C. Neitzert, Luigi Vertuccio, and Andrea Sorrentino. “Epoxy/MWCNT Composite as Temperature Sensor and Electrical Heating Element”. In: *IEEE Transactions on Nanotechnology* 10.4 (2011), pp. 688–693. ISSN: 1536-125X. DOI: 10.1109/TNANO.2010.2068307.

[175] Afarin Bahrami et al. “Low temperature hall effect investigation of conducting polymer-carbon nanotubes composite network”. In: *International journal of molecular sciences* 13.11 (2012), pp. 14917–14928. DOI: 10.3390/ijms131114917.

[176] Michael K. Njuguna. “Characterisation of multi wall carbon nanotube polymer composites for strain sensing applications”. Dissertation. Queensland: Queensland University of Technology, 2012.

[177] Waris Obitayo and Tao Liu. “A Review: Carbon Nanotube-Based Piezoresistive Strain Sensors”. In: *Journal of Sensors* 2012 (2012), pp. 1–15. ISSN: 1687-725X. DOI: 10.1155/2012/652438.

[178] J. T. Shen et al. “Pressure and temperature induced electrical resistance change in nano-carbon/epoxy composites”. In: *Composites Science and Technology* 115 (2015), pp. 1–8. ISSN: 0266-3538. DOI: 10.1016/j.compscitech.2015.04.016.

[179] Bogdan Florian Monea et al. “Carbon Nanotubes and Carbon Nanotube Structures Used for Temperature Measurement”. In: *Sensors (Basel, Switzerland)* 19.11 (2019). DOI: 10.3390/s19112464.

[180] Abdulkadir Sanli. “Investigation of temperature effect on the electrical properties of MWCNTs/epoxy nanocomposites by electrochemical impedance spectroscopy”. In: *Advanced Composite Materials* 29.1 (2020), pp. 31–41. ISSN: 0924-3046. DOI: 10.1080/09243046.2019.1616409.

[181] John G. Simmons. “Low-Voltage Current-Voltage Relationship of Tunnel Junctions”. In: *JOURNAL OF APPLIED PHYSICS* 34.1 (1963), pp. 238–239. DOI: 10.1063/1.1729081.

[182] John G. Simmons. “Generalized Formula for the Electric Tunnel Effect between Similar Electrodes Separated by a Thin Insulating Film”. In: *JOURNAL OF APPLIED PHYSICS* 34.6 (1963), pp. 1793–1803. DOI: 10.1063/1.1702682.

[183] John G. Simmons. “Electric Tunnel Effect between Dissimilar Electrodes Separated by a Thin Insulating Film”. In: *JOURNAL OF APPLIED PHYSICS* 34.9 (1963), pp. 2581–2590. DOI: 10.1063/1.1729774.

[184] Ping Sheng, E. K. Sichel, and J. I. Gittleman. “Fluctuation-Induced Tunneling Conduction in Carbon-Polyvinylchloride Composites”. In: *Physical review letters* 40.18 (1978), pp. 1197–1200. ISSN: 0031-9007.

[185] Ping Sheng. “Fluctuation-induced tunneling conduction in disordered materials”. In: *Physical Review B* 21.6 (1980), pp. 2180–2195. ISSN: 1098-0121.

[186] F. Carmona and C. Mouney. “Temperature-dependent resistivity and conduction mechanism in carbon particle-filled polymers”. In: *Journal of Material Science* 27 (1992), pp. 1322–1326.

[187] Xiang-Wu Zhang et al. “Time dependence of piezoresistance for the conductor-filled polymer composites”. In: *Journal of Polymer Science Part B: Polymer Physics* 38.21 (2000), pp. 2739–2749. ISSN: 0887-6266. DOI: 10.1002/1099-0488(20001101)38:21<2739::AID-POLB40>3.0.CO;2-0.

[188] G. R. Ruschau, S. Yoshikawa, and R. E. Newnham. “Resistivities of conductive composites”. In: *JOURNAL OF APPLIED PHYSICS* 72.3 (1992), pp. 953–959. DOI: 10.1063/1.352350.

[189] J. C. Dawson and C. J. Adkins. “Conduction mechanisms in carbon-loaded composites”. In: *Journal of Physics: Condensed Matter* 8 (1996), pp. 8321–8338. URL: https://iopscience.iop.org/article/10.1088/0953-8984/8/43/024.

[190] M. H. G. Wichmann et al. “Multiwall carbon nanotube/epoxy composites produced by a masterbatch process”. In: *Mechanics of Composite Materials* 42.5 (2006), pp. 395–406. DOI: 10.1007/s11029-006-0050-3.

[191] Hang Xie and Ping Sheng. “Fluctuation-induced tunneling conduction through nanoconstrictions”. In: *Physical Review B* 79.16 (2009). ISSN: 1098-0121. DOI: 10.1103/PhysRevB.79.165419.

[192] Andries Voet. “Temperature effect of electrical resistivity of carbon Black filled polymers”. In: *Rubber Chemistry and Technology* 54 (1981), pp. 42–50. URL: https://doi.org/10.5254/1.3535796.

[193] M. S. Fuhrer et al. “Crossed Nanotube Junctions”. In: *Science Reports* 288.21 (2000), pp. 494–497. URL: 10.1126/science.288.5465.494.

[194] Philippe Gonnet. “Thermal Conductivity and Coefficients of Thermal Expansion of Swnts/Epoxy Nanocomposites”. Master Thesis. Florida State University, 2004.

[195] S. Wang et al. “Effect of Nanotube Functionalization on the Coefficient of Thermal Expansion of Nanocomposites”. In: *Advanced Functional Materials* 17.1 (2007), pp. 87–92. ISSN: 1616-301X. DOI: 10.1002/adfm.200600760.

[196] Ning Hu Alamusi et al. “Multi-scale numerical simulations of thermal expansion properties of CNT-reinforced nanocomposites”. In: *Nanoscale Research Letters* 8.15 (2013). URL: https://doi.org/10.1186/1556-276X-8-15.

[197] Orion Engineered Carbons. *OEC-3121 R1 Carbon Blacks Coatings Brochure*. 2013.

[198] Avanzare Innovacion Tecnologica S.L. *TDS_AVAN2*. URL: https://www.avanzarematerials.com/wp-content/uploads/2020/06/Graphene-Catalogue.pdf.

[199] Nanocyl SA. “NC7000 series - Product Datasheet - Thin Multi-Wall Carbon Nanotubes”. In: ().

[200] Nanocyl SA. “SDS NC7000: Multiwall Carbon Nanotubes”. In: (2016). URL: https://www.nanocyl.com/download/sds-nc7000/ (visited on 11/11/2022).

[201] OCSiAl. *TDS_TUBALL_01RW03*. URL: https://tuball.com/de/additives/tuball.

[202] OCSiAl. *SDS Tuball EU (Reach Annex II)*. URL: https://tuball.com/de/additives/tuball.

[203] Hauke Meeuw et al. “In-line monitoring of carbon nanoparticle epoxy dispersion processes”. In: *Production Engineering* 13.3-4 (2019), pp. 373–390. ISSN: 0944-6524. DOI: 10.1007/s11740-019-00884-5.

[204] Lukas Steinmetz et al. “Lock–In Thermography to Analyze Plasmonic Nanoparticle Dispersions”. In: *Particle & Particle Systems Characterization* 36.9 (2019), p. 1900224. ISSN: 0934-0866. DOI: 10.1002/ppsc.201900224.

[205] Lukas Steinmetz et al. “Rapid and sensitive quantification of cell-associated multi-walled carbon nanotubes”. In: *Nanoscale* 12.33 (2020), pp. 17362–17372. DOI: 10.1039/d0nr03330h.

[206] Lukas Steinmetz et al. “Experimental and Theoretical Validation of Plasmonic Nanoparticle Heat Generation by Using Lock-In Thermography”. In: *The Journal of Physical Chemistry C* 125.10 (2021), pp. 5890–5896. ISSN: 1932-7447. DOI: 10.1021/acs.jpcc.0c11419.

[207] Christoph Geers. *NanoLockin Application note - Dispersions*. Ed. by NanoLockin GmbH. 2022. URL: https://drive.google.com/file/d/18qlJGKZsRRX-v8EGhPE0ZkYauMmwSF5g/view.

[208] BAL-TEC Inc. “Sputter Coater SCD 050 Betriebsanleitung”. In: (1990). URL: https://www.baltic-praeparation.de/betriebsanleitungen.html?file=files/Baltic/Betriebsanleitungen/SCD%20050%20Betriebsanleitung.pdf (visited on 11/11/2022).

[209] Thomas Schröder. *Rheologie der Kunststoffe: Theorie und Praxis*. Hanser eLibrary. München: Hanser, 2018. ISBN: 978-3-44645722-5. DOI: 10.3139/9783446457225.

[210] Jeroen W. G. Wildoer et al. “Electronic structure of atomically resolved carbon nanotubes”. In: *Nature* 391 (1998), pp. 59–62. URL: https://www.nature.com/articles/34139.

[211] Zhengzhi Wang et al. “Bioinspired Wear-Resistant and Ultradurable Functional Gradient Coatings”. In: *Small (Weinheim an der Bergstrasse, Germany)* 14.41 (2018), e1802717. DOI: 10.1002/smll.201802717.

[212] Zhengzhi Wang et al. “Bioinspired Wear-Resistant and Ultradurable Functional Gradient Coatings”. In: *Small (Weinheim an der Bergstrasse, Germany)* 14.41 (2018), e1802717. DOI: 10.1002/smll.201802717.

[213] Hexion Specialty Chemicals. “Epikote Resin RIM135 Epikure Curing Agent RIM137 Technical Data Sheet”. In: (2021). URL: https://www.metyx.com/wp-content/uploads/PDF_Files/Hexion/TDS/TDS%20RIMH%20137.pdf (visited on 07/13/2023).

A Appendix - In-Line Monitoring

The strain and frequency-dependent temperature sweeps of neat UP resin and UPT masterbatch can be found in Figure A.1.

A.1 Line Force Interpretation

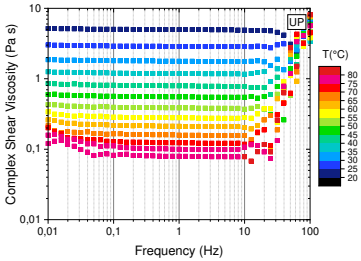

(a) Frequency Sweep over Temperature at 1 % strain

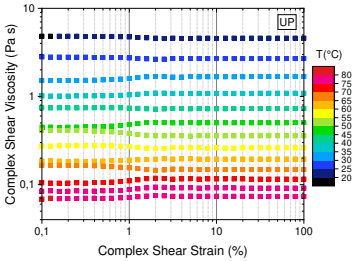

(b) Strain Sweep over Temperature at 1 Hz oscillation

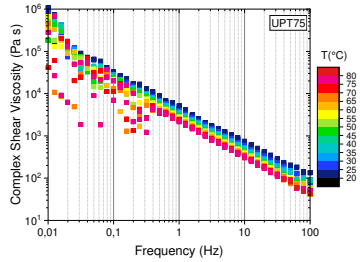

(c) Frequency Sweep over Temperature at 1 % strain

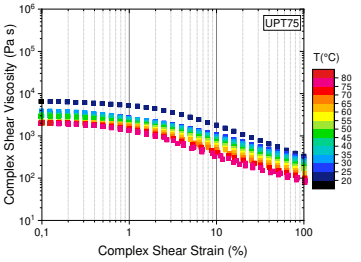

(d) Strain Sweep over Temperature at 1 Hz oscillation

Figure A.1: Temperature dependent complex viscosity of neat UP resin and UPT75 masterbatch.

In Figure A.2a) the standard steps of processing neat UP resin are repeated after changing the roller temperature to 30 °C. Within 0.5 °C the temperature stays on the same level. The dissipating heat from the machine and friction has no significant influence on the measured temperature on any roller or the line force. Thus, also the average line force of 3 N/mm shows no significant change over the five repeated steps with minimum gap spacing. The overall processing time is elongated by 25 % compared to the standard process at 20 °C up to a total of 650 s.

Lastly, a roller temperature of 40 °C is tested and depicted in Figure A.2b). The measured temperature at each of the rollers is around 38 °C - whereas the dissipated heat of machine and blade has no influence in raising the processing temperature in this case the ambient temperature of the lab of about 23 °C leads to surface cooling of the resin on the large roller surface area. Therefore, holding a temperature of 40 °C is not possible without putting the TRM in a heated enclosure. Nonetheless, a reduced line force of nearly 2 N/mm can be observed due to the elevated temperature. The total processing time of 700 s has increased by 35 % in comparison to the standard process at 20 °C.

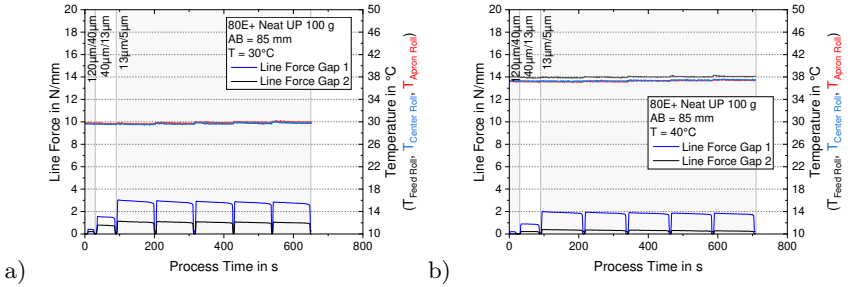

Figure A.2: Line forces of neat UP resin for a standard 80E *Plus*$^+$ process at a) 30 °C and b) 40 °C

A.2 In-Line Monitoring

A.2.1 Integration of the Electrode on the Apron

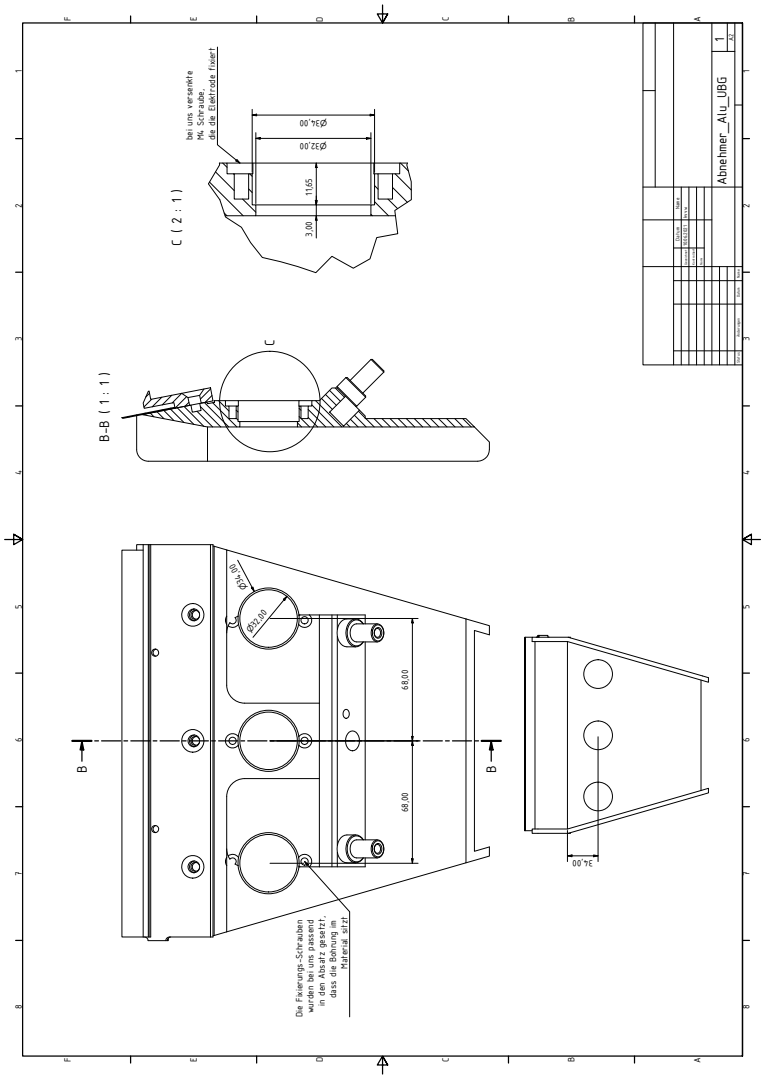

Figure A.3: Technical drawing for three integrated electrodes

A.2.2 Supplementary Graphs on In-Line Monitoring Different CNP Fillers

CB In-Line Monitoring

By doubling the carbon black filler content to 8 wt% the viscosity increases to 1000 Pas. This is reflected in the higher values of line force per step shown in Figure A.4a). In all steps, the dispersion process is stable without any separation. In contrast to the lower filler content in Fig. 4.22, a slight increase in processing time for steps 3 to 7 with smallest gap spacing can be observed in Fig. A.4b). The complex impedance shows a lower initial value after the first step in comparison to the lower filler content and reaches a lower constant level from step 2.

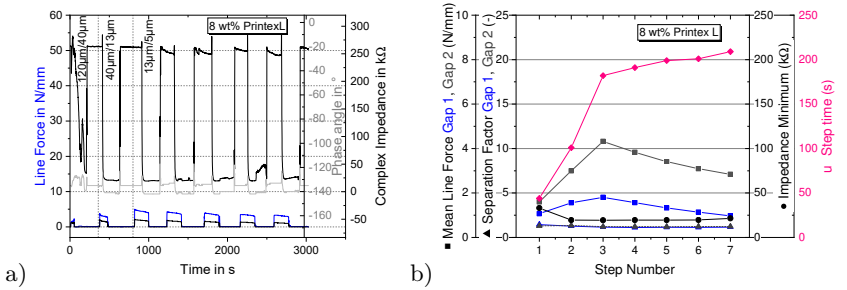

Figure A.4: a) In-line Monitoring signals and b) statistics of 8 wt% Printex L

With highest tested filler loading of 12 wt%, which is above the percolation threshold, every step shows minimum complex impedance values indicating a conductive particle network from the initial step on, compare constant values in A.5a). Since the globular particles rise the viscosity but just form easily dispersable agglomerates, the line forces show stable behavior in all steps (Fig. A.5b)).

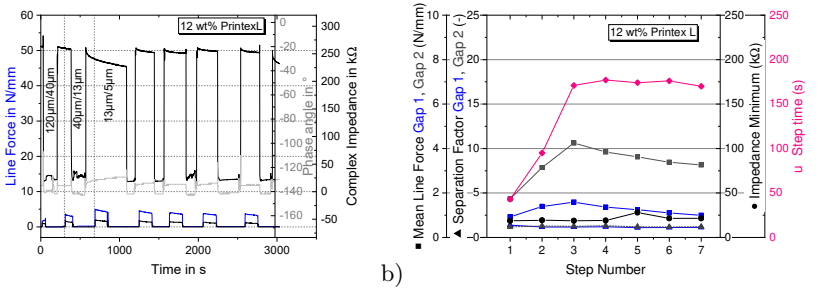

Figure A.5: a) In-line monitoring signals and b) statistics of 12 wt% Printex L

FLG In-Line Monitoring

For increased filler content of 0.75 wt% AVAN2 Figure A.6 shows a more pronounced separating behavior towards the end of all dispersion steps until step 4. The complex impedance value shows a minimum at the beginning of each step after initial coverage of the electrode but the plateaus at a slightly higher value for the static flow segment. The residual material film on the electrode at the end of each step is characterized by another minimum. The minimum of the third dispersion step is again most pronounced correlating with the small separation peak. The processing time is only influenced by the gap spacing for each step.

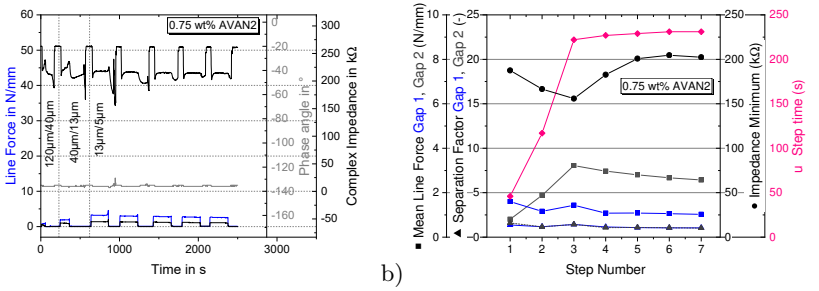

Figure A.6: a) In-line monitoring signals and b) statistics of 0.75 wt% AVAN2

Highest tested filler content of FLG is shown in Figure A.7. The separation of particles and resin is most pronounced in step 3 again leading to the lowest measured complex impedance in the end of the step.

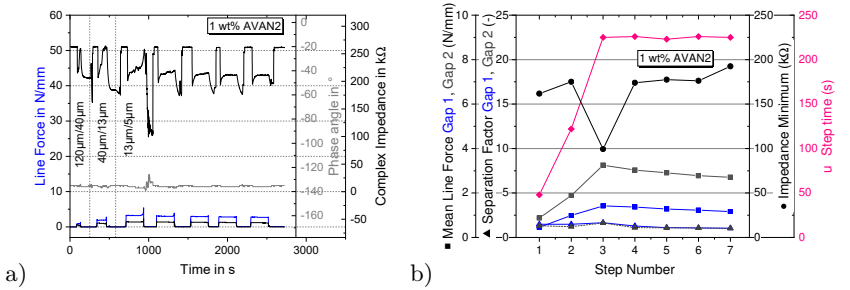

Figure A.7: a) In-line monitoring signals and b) statistics of 1 wt% AVAN2

MWCNT In-Line Monitoring

With 0.3 wt% NC7000 the percolation threshold is reached and the inline monitoring signals in Figure A.8 show a change in dispersion behavior. The viscosity has risen and the particle separation within the first three steps causes slight separation peaks in the line forces in step 1 to 3. In comparison to 0.1 wt% the complex impedance decreased. The signal form again shows a minimum in the beginning of a step and in towards the end but with lower absolute values. The minimum impedance value is already reached in step 3, but only in the second minimum of that step. Figure A.8b) shows low impedance values from step 3 on. Decreased processing time per step can be observed for the last five steps with the smallest gap spacing because the increased viscosity favors the material transport over the rollers.

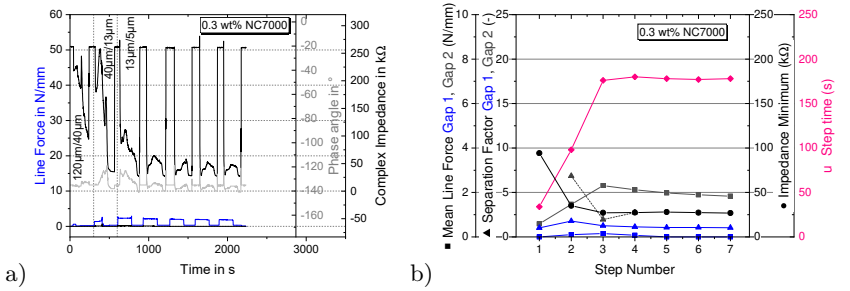

Figure A.8: a) In-line monitoring signals and b) statistics of 0.3 wt% NC7000

Forming an over-percolated particle network 0.5 wt% NC7000 are the last filler content to be discussed by Figure A.9. The behavior of all signals is similar

to the lower filler content. Slight separation within the first three steps can be observed as well as a decrease of the minima of complex impedance in each step. The processing time per step has decreased by around 10%.

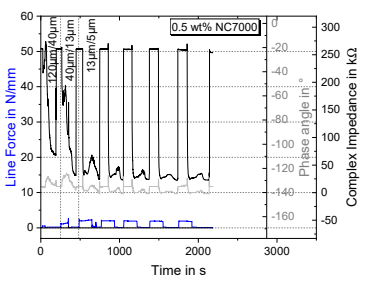

a)

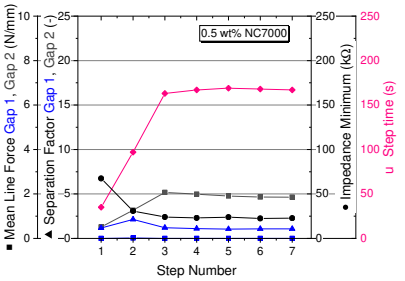

b)

Figure A.9: a) In-line monitoring signals and b) statistics of 0.5 wt% NC7000

SWCNT In-Line Monitoring

In Figure A.10 the lowest processed filler content of 0.01 wt% Tuball 75 in UP resin is shown. Due to a recording error only the last 5 steps can be shown. These steps show minimal dispersion peaks for each of the steps at smallest gap spacing. The steps take similar time and show nearly constant mean line force values. The development of the complex impedance value over time shows minima at the start and end of each step similar to MWCNT. It has to be noted that during the steady flow state in the middle of a step, the complex impedance values can rise above the empty electrode value, which is not explainable. Values close to the empty electrode can be caused by a film of neat resin on the electrodes, if the conductive particles flow too fast to properly contact the electrode.

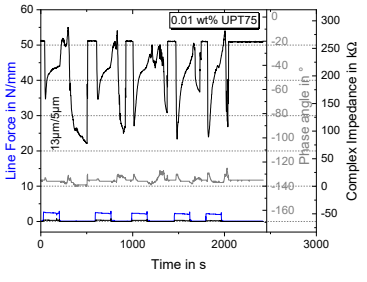

a)

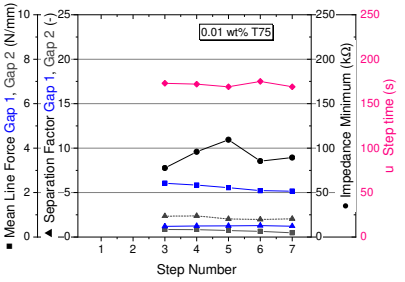

b)

Figure A.10: a) In-line monitoring signals and b) statistics of 0.01 wt% T75

Increasing the filler content to 0.02 wt% T75 (Figure A.11) reduces the impedance values of the final dispersion state further. In the first step, higher concentrated material runs over the electrode in the end reducing the measured impedance, in step 2 the material is more homogenized and thus increases the value gain. From step 3 on the impedance in the beginning and the end of each step stabilizes at a constant low level. The processing time per step has decreased in comparison to lower filler content.

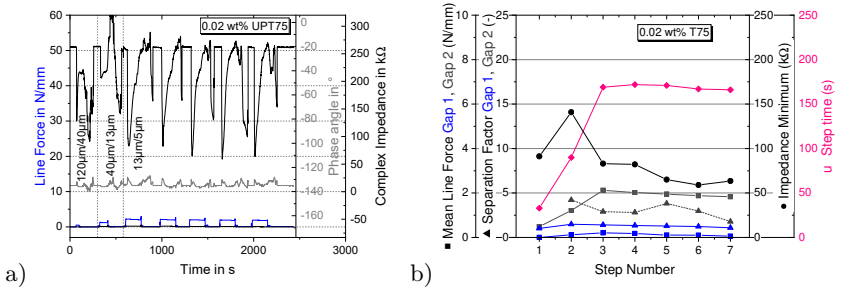

Figure A.11: a) In-line monitoring signals and b) statistics of 0.02 wt% T75

For 0.03 wt% the minimum impedance value is reached in step 4 the first time, a decrease over the first four steps can be observed in A.12. The line force signals show small separation peaks in steps 1 to 6. Because the line force is nearly zero over most of the dispersion step the separation factor is calculated to extremely high values for gap 2. Figure A.12b) thus indicates more severe separation, even though the line forces depicted in Figure A.12a) are on the lowest level. This raises the question of whether the separation factor should be calculated for every state of the dispersion or set to zero if the forces are so low anyways.

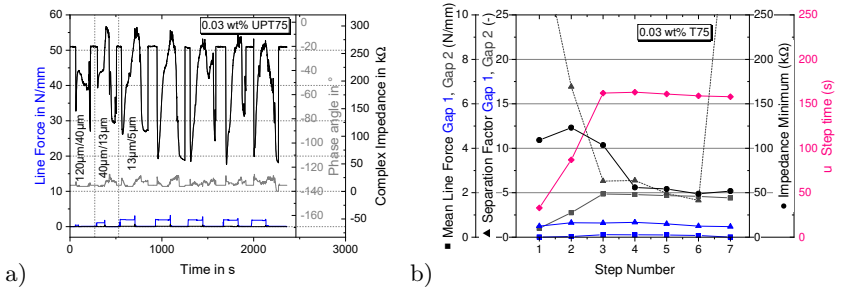

Figure A.12: a) In-line monitoring signals and b) statistics of 0.03 wt% T75

In Figure A.13 0.04 wt% of Tuball 75 show a very similar behavior to previous low filler contents. The separation peaks in the overall line forces of gap 2 cause high separation factors again, which are not representative of the state of processing. Besides that overshoots of the measured impedance is observed during the flow state in the middle of each step again. The impedance value after the whole process is lower than for lower filler content which is in good accordance to the offline measurements in Figure 4.20, wherein the complex impedance decreases up to 0.05 wt%.

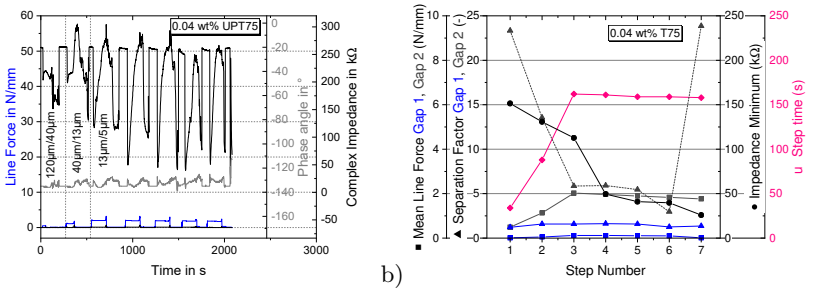

Figure A.13: a) In-line monitoring signals and b) statistics of 0.04 wt% T75

In Figure A.14 a 0.1 wt% Tuball 75 dispersion process is depicted. The line forces are overall higher since more particles have to be dispersed into the resin, at this filler content there is also separation to be observed at the end of steps 1 to 4, which is reflected in the peaks towards the end of a step in the line force. The complex impedance measurement shows lower maxima in the flow state. So after the minima of initial electrode coverage only a moderate raise way below the empty electrode level is observed.

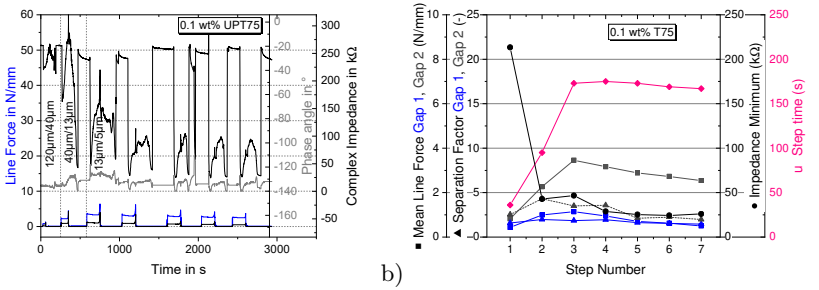

Figure A.14: a) In-line monitoring signals and b) statistics of 0.1 wt% T75

A.2.3 Machine Stiffness and Rotational Speed

Figure A.15 shows the calculated gap widening to determine the machine stiffness of the 80E *Plus*$^+$ TRM. Two 30 µm stainless steel feeler gauges are inserted into each gap between rollers. Next, a certain gap spacing is set on the TRM for both gaps. The resulting line force is noted and plotted as solid squares in Figure A.15. Next, the gap spacing is reduced and an increase in resulting line force can be seen due to the feeler gauge within the gap. This procedure is repeated down to minimum gap spacing of 5 µm, where a maximum of about 4.5 N/mm is recorded. Because the stainless steel feeler gauge can be considered as incompressible for this load range, the gap widening can be calculated by subtracting the set gap space from the 30 µm. Thus, the hollow square points in the diagram give the inverse slope of the solid squares. Considering the slope from fitting the line force per gap widening of the machine, a compliance factor C_{TRM} can be calculated. For the 80E *Plus*$^+$ it is 5.8 µm/(N/mm) in the feeding gap and 6.1 µm/(N/mm). This gap widening per occurring line force has been considered in section 4.3 to adjust the gap spacing in the dynamic mode. The real gap spacing including the widening can be calculated as:

$$h_{\mathrm{real}} = LF \cdot C_{\mathrm{TRM}} + h_0 \tag{A.1}$$

With line force LF, TRM compliance C_{TRM} and set gap spacing h_0.

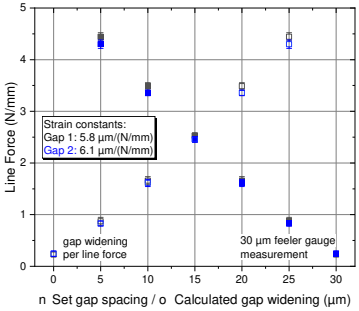

Figure A.15: Compliance of the 80E *Plus*$^+$

The time continuous data for different rotational speeds can be found in Figure A.16 and A.17. 500 g material has been processed on minimal gap spacing at different roller speeds to calculate the material flow per time as presented in Figure 4.39. Besides increased productivity for higher rotational speed, the

increased mean line forces can be seen. Additionally, it can be noted again that the line forces in feeding and dispersion gap differ less on the 120E TRM.

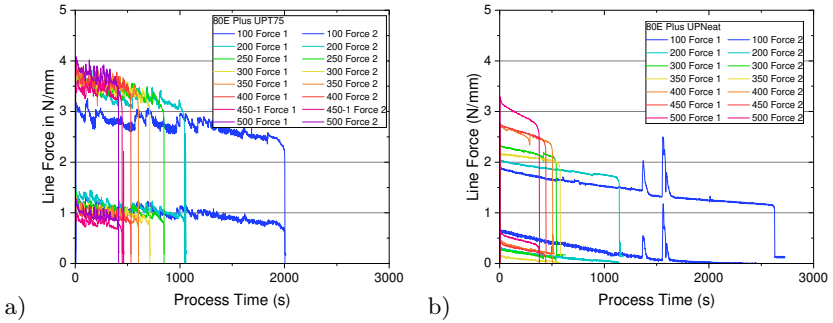

a) b)

Figure A.16: Inline monitoring signals of a) 1 wt% Tuball 75 in UP and b) neat UP for varied rotational speed on a 80E *Plus*$^+$

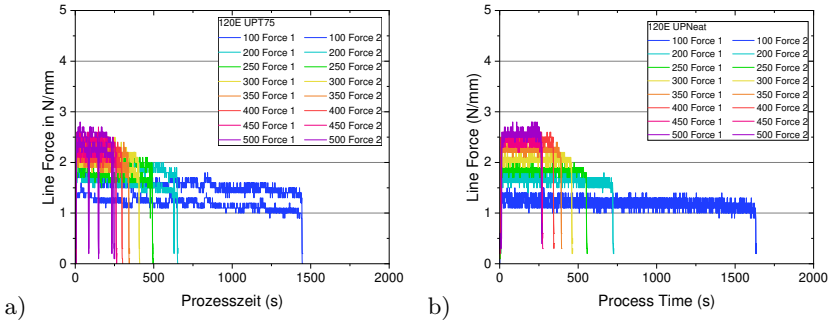

a) b)

Figure A.17: Inline monitoring signals of a) 1 wt% Tuball 75 in UP and b) neat UP for varied rotational speed on a 120E-250

B Appendix - Magnetic Manipulation

B.1 Open Mold Nanocomposites Cured under Permanent Magnets

The magnetic manipulation topic was started by trying to use Neodymium permanent magnets as shown in Figure B.1 and B.2. The magnetic field has been measured to quantify the field intensity in comparison to the magnet circuit described in Chapter 2.3.2.

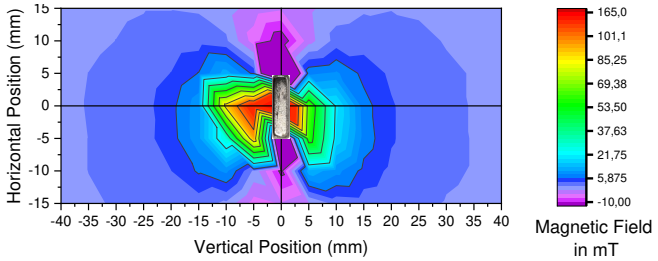

Figure B.1: Magnetic field above the center of a single magnet in side view

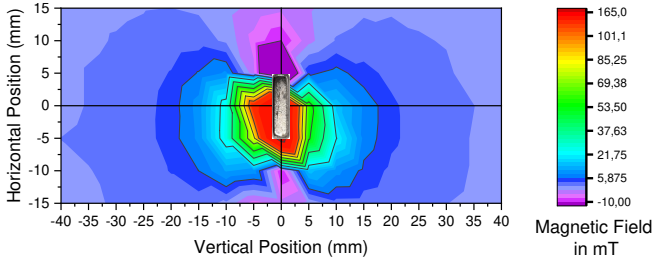

Figure B.2: Magnetic field measured at the edge of a single magnet in side view

In the beginning, a simple approach was chosen wherein 0.01 wt% of NC7000 were dispersed into a RIM 135 epoxy resin matrix via TRM, the composite was

later cured with RIMH 137 to investigate the behavior of the composite under an applied magnetic field. This low filler content composite was chosen to easily see particle concentration changes within the composite caused by magnet fields by different grey-shades. For the open mold, a polished Aluminium plate was chosen as a base plate. The frame of the open mold could be chosen to manufacture a plate of 0.5 mm, 1 mm or 2 mm thickness, respectively.

The magnet arrangement was chosen to be an array of 3 x 3 magnets at first. They were placed over the mold on a glass carrier and fixated so they were in the center of the plate.

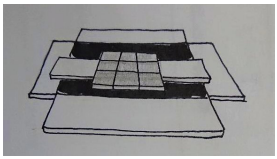

Figure B.3: Schematic view of the magnet set-up in a 3 x 3 array

Figure B.4 shows the manufactured plates, which were cured with an applied 3 x 3 array. Clearly, the plate shows a bulge of thicker material in the middle, where the magnets were placed. Reference plates of neat resin have been manufactured to exclude, that the deformation originated in the resin behavior. Although there could be seen some inhomogeneities in fine bubbles and shades within the resin, there was no rise of the plate middle without the magnet. Thus, the effect can be ascribed to the incorporated MWCNTs.

a) 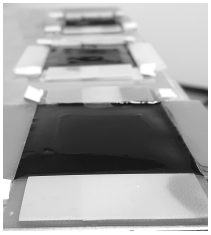 b) 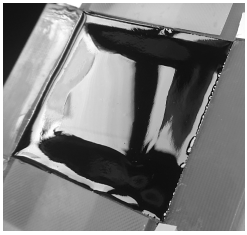

Figure B.4: Resulting plates from 3 x 3 magnet array set-up a) overview and b) detailed view of the 2 mm plate

The 3 x 3 set-up creates a magnetic gradient field within the nanocomposite, thus a movement of particles towards the strongest magnetic field is expected as in

water/ethanol mixtures shown in Chapter 5. However the systematic approach of that chapter has also shown that NC7000 has not the strongest reaction to applied magnetic fields, the resin viscosity hinders the particle movement significantly due to increased viscosity and the dispersion stability counter-acts the particle movement, too. Nonetheless, the middle of most plates cured under the magnetic field are thicker, so CNT and adherent resin molecules around the CNT must have been moved along the gradient field.

Another set-up that showed significant changes in shape by curing under magnets was the stack set-up with nine magnets on top of each other and then placing the stack laying over the plate as depicted in Figure B.5a). The resulting plate after curing shows a rough surface as can be seen in Figure B.5b), which was a phenomenon showing randomly throughout different manufacturing processes with any or no magnets applied. The elevated part in the middle of the plate was placed under the magnets and exhibits a rectangular shape larger than the magnet stack. In the center strip, (horizontal in image B.5b)) this roughness texture is coarser than below and above where the far field of the magnet stack was. Also, the coarse-grained field shows extended lines in the direction of each corner of the mold. The origin of all these surface phenomenons has no explanation yet, the effects occurred randomly although no active changes in manufacturing have been made. Most likely the curing reaction of the epoxy is causing this surface texture depending on the molecular arrangement of CNTs and epoxy makro-molecules.

a) 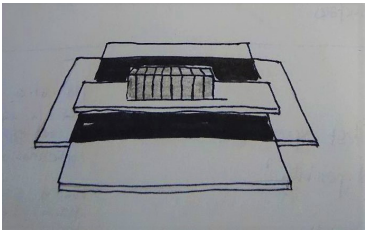 b) 

Figure B.5: a) Schematic view of the magnet set-up in a nine magnets stack and b) resulting 2 mm plate from curing under a stack of nine magnets

B.2 Visualizing the Magnetic Field with Iron Filings

Figure B.6a) shows the resulting iron filing patterns of the 10mm x 10mm x 3mm block Neodymium magnet from Figure B.1 laying flat on the ground. While the

magnetic field lines are perpendicular to the surface pointing iron filings out of the plane directly over the magnet, the influence around the magnet decreases continuously with increasing distance. Combining 3 x 3 magnets to an array introduces an inhomogeneous field as depicted in Figure B.6b) with field lines pointing out of plane above the magnets and forming bows between neighboring magnets. Especially towards the edges of the array magnetic field lines bend out directing into the far field.

a) 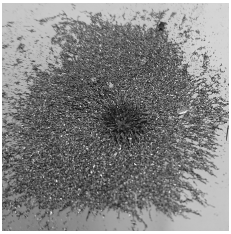 b) 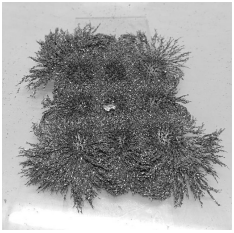

Figure B.6: Iron filing patterns of a) single block Neodymium magnet and b) the 3 x 3 array that was used for curing the plates under magnetic field

In the stack configuration, the magnetic field of several magnets superpose to a stronger field with the same direction. Figure B.7a) shows the stack configuration of 15 magnets on top of each other with a stronger field leading to a more far-reaching alignment of the iron filings away from the magnets. On top of them the iron needles are standing up significantly taller in comparison to the single magnet depicted in Figure B.6a). To achieve a homogeneous field in a defined area the configuration in Figure B.7b) could be adapted, orienting the particles in between of two magnets with the same pole direction. The magnetic field lines between them are straight, aligning the iron needles in one direction only.

a) 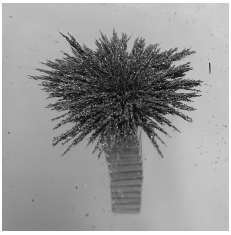 b) 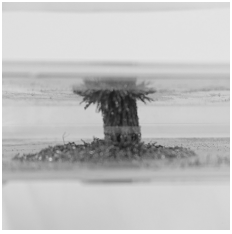

Figure B.7: Iron filing patterns of a) 15 Neodymium magnets stacked and b) a gap positioning of two magnets with iron filings in between

B.3 Temperature-Dependent Rheological Resin Behavior

The commonly used DGEBA epoxy resin EPON 828 was used at the beginning of this thesis, but the supply has been stopped within on-going research. Due to a switch to similar resin EPON 828LVEL, all results of this thesis are discussed based on the latter version. In Figure B.8 the temperature-dependent complex viscosity of neat 828LVEL resin is shown within the boundaries of its application temperature from 20–80 °C at 1 % strain.

In B.8a) the frequency sweep is depicted, showing the decrease of viscosity over temperature by coloration. From 20–40 °C the polymer's response is independent of frequency, which can be seen by the horizontal graphs. For small oscillation frequencies below 0.1 Hz an increase of measured viscosity for smaller frequencies can be observed. For high frequencies between 10–100 Hz a similar phenomenon is observed with increasing values forming a U-shaped characteristic of viscosity over frequency. This behavior is not a material response but the limitations of the measurement system. For high oscillatory frequencies, the stability of a low-viscous medium is not given, for example by material dripping out of the gap. This results in a high signal-to-noise ratio and unreliable results. For slow oscillatory movements with frequencies below 0.1 Hz an increase in viscosity seems to occur. Analyzing the rheometers test log, out-of-range phase angles and geometry-inertia-dominated behavior can be found. This means that again, the material behavior can not be determined in that region. Between 0.1–10 Hz it is frequency-independent for all measured temperatures which is the expected behavior of a neat epoxy resin.

In B.8b) the strain responsive behavior is shown. For lower temperatures the resin behavior is strain-independent. For higher temperatures of over 50 °C an increase of measured viscosity with decreasing strain amplitude can be observed, which is unusual for unfilled resins. Thus, the minimum viscosity achievable by heating the neat resin is 0.1 Pas, which is two orders of magnitude higher than water or ethanol.

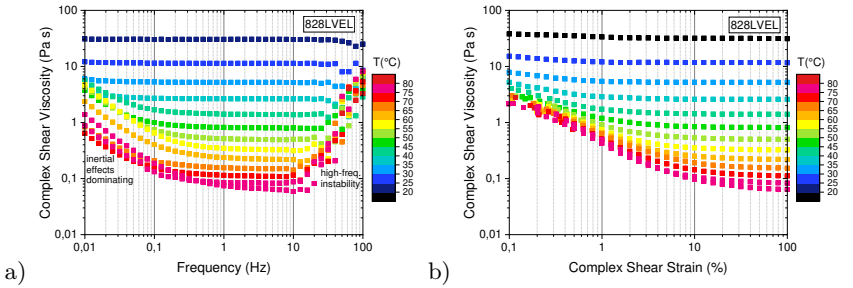

Figure B.8: Temperature-dependent complex viscosity of neat EPON 828LVEL from a) temperature-frequency sweeps at 1 % strain and b) temperature-strain sweeps at 1 Hz oscillation

Adding SWCNT Tuball 75 to the resin by three-roll milling increases the viscosity further. In Figure B.9 the frequency and strain sweeps within the temperature range 20–80 °C are depicted. In Figure B.9a) it can be seen that the dispersion shows a clear frequency dependence of decreasing viscosity for increasing oscillatory frequency. From about 2000 Pas at 0.01 Hz for all temperatures the decrease is temperature independent up to 0.2 Hz with 300 Pas. For higher frequencies, the temperature determines the lowest reachable viscosity between 90 Pas at 20 °C and 2 Pas at 80 °C. The strain sweep in Figure B.9b) reveals typical strain-thinning behavior of the dispersion for strains higher than 10 %. The lowest achievable viscosity at 80 °C is 8 Pas.

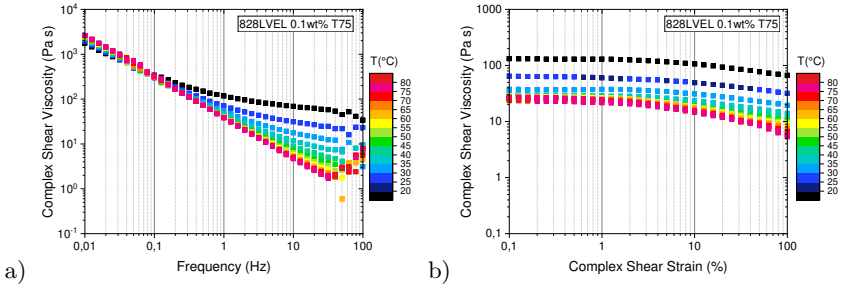

Figure B.9: Temperature-dependent complex viscosity of EPON 828LVEL with 0.1 wt% Tuball 75 from a) temperature-frequency sweeps at 1 % strain and b) temperature-strain sweeps at 1 Hz oscillation

For EPON 828 identical rheological characterization was conducted and can be found in Figure B.10.

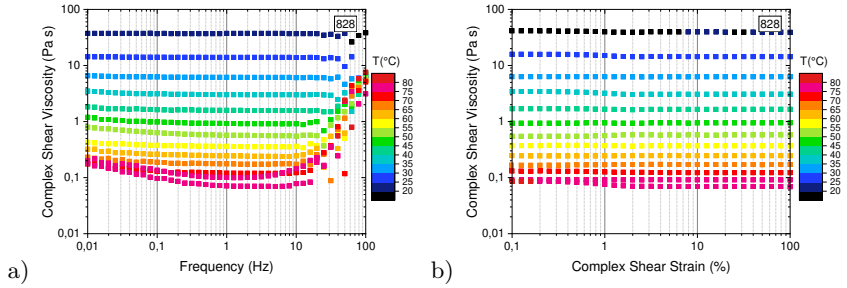

Figure B.10: Temperature-dependent complex viscosity of neat EPON 828 from a) temperature-frequency sweeps at 1 % strain and b) temperature-strain sweeps at 1 Hz oscillation

C Appendix - Temperature Sensing

C.1 Sample Geometry

Table C.1: Geometry of all prepared temperature sensing (1-5) and moisture absorption (6) samples

CNP	Filler Content ($wt\%$)	No.	W (mm)	T (mm)	L (mm)	A (mm^2)
T99	0.01	1	7.95	4.92	49.91	39.11
T99	0.01	2	7.94	4.93	49.83	39.13
T99	0.01	3	7.90	4.97	50.06	39.22
T99	0.01	4	8.01	4.96	49.82	39.69
T99	0.01	5	8.01	4.93	49.93	39.50
T99	0.01	6	7.89	4.96	49.79	39.16
T99	0.05	1	7.89	4.97	49.84	39.20
T99	0.05	2	8.00	4.96	49.73	39.66
T99	0.05	3	7.96	4.95	49.96	39.41
T99	0.05	4	7.95	4.96	49.90	39.48
T99	0.05	5	7.95	4.97	49.87	39.53
T99	0.05	6	7.89	4.96	49.62	39.15
T99	0.1	1	7.88	4.95	49.82	39.00
T99	0.1	2	7.99	4.95	49.73	39.54
T99	0.1	3	7.88	4.97	49.81	39.15
T99	0.1	4	7.98	4.94	49.85	39.38
T99	0.1	5	8.01	4.96	49.71	39.74
T99	0.1	6	7.95	4.95	49.82	39.31
T75	0.01	1	7.88	4.95	49.83	38.99
T75	0.01	2	7.88	4.95	49.85	39.03
T75	0.01	3	7.95	4.95	49.81	39.33
T75	0.01	4	7.98	4.96	49.77	39.54
T75	0.01	5	8.00	4.95	49.70	39.60
T75	0.01	6	8.01	4.94	49.79	39.60
T75	0.05	1	7.97	4.95	49.85	39.42
T75	0.05	2	7.95	4.96	49.80	39.45
T75	0.05	3	7.90	4.95	49.71	39.06
T75	0.05	4	8.89	4.94	49.71	38.96
T75	0.05	5	8.00	4.97	49.72	39.72
T75	0.05	6	7.95	4.97	49.87	39.49
T75	0.1	1	7.90	4.95	49.83	39.06
T75	0.1	2	7.98	4.96	49.72	39.59
T75	0.1	3	8.05	4.96	49.76	39.68
T75	0.1	4	7.98	4.94	49.89	39.42
T75	0.1	5	8.01	4.96	49.85	39.71

Table C.1: Geometry of all prepared temperature sensing (1-5) and moisture absorption (6) samples

CNP	Filler Content ($wt\%$)	No.	W (mm)	T (mm)	L (mm)	A (mm^2)
T75	0.1	6	7.90	4.96	49.88	39.20
T75	0.5	1	8.03	4.95	49.96	39.75
T75	0.5	2	7.93	4.96	49.81	39.32
T75	0.5	3	8.03	4.94	49.82	39.68
T75	0.5	4	7.95	4.95	49.85	39.34
T75	0.5	5	8.00	4.95	49.85	39.61
T75	0.5	6	8.02	4.96	49.93	39.82
NC7000	0.1	1	7.95	4.97	49.93	39.50
NC7000	0.1	2	8.03	4.96	49.96	39.85
NC7000	0.1	3	7.95	4.95	49.79	39.34
NC7000	0.1	4	7.88	4.97	49.94	39.12
NC7000	0.1	5	7.96	4.96	49.89	39.52
NC7000	0.1	6	8.01	4.95	49.85	39.63
NC7000	0.3	1	7.89	4.97	49.41	39.20
NC7000	0.3	2	7.90	4.96	49.79	39.18
NC7000	0.3	3	8.03	4.97	49.52	39.90
NC7000	0.3	4	7.95	4.96	49.82	39.46
NC7000	0.3	5	8.02	4.95	49.95	39.71
NC7000	0.3	6	7.96	4.95	49.95	39.38
NC7000	0.5	1	7.88	4.96	49.93	39.10
NC7000	0.5	2	7.99	4.96	49.96	39.67
NC7000	0.5	3	7.96	4.96	49.79	39.49
NC7000	0.5	4	7.98	4.93	49.94	39.32
NC7000	0.5	5	7.90	4.96	49.89	39.19
NC7000	0.5	6	8.00	4.96	49.85	39.64
NC7000	0.7	1	7.89	4.94	49.88	39.96
NC7000	0.7	2	7.95	4.91	49.92	39.06
NC7000	0.7	3	7.95	4.94	49.88	39.28
NC7000	0.7	4	7.95	4.94	49.50	39.27
NC7000	0.7	5	8.01	4.95	49.96	39.63
NC7000	0.7	6	7.95	4.95	49.95	39.35
AVAN2	0.5	1	7.89	4.97	49.86	39.24
AVAN2	0.5	2	7.96	4.97	49.80	39.53
AVAN2	0.5	3	7.97	4.96	49.84	39.56
AVAN2	0.5	4	7.96	4.97	49.89	39.58
AVAN2	0.5	5	7.89	4.97	49.79	39.24
AVAN2	0.5	6	8.00	4.97	49.90	39.79
AVAN2	1	1	8.00	4.92	49.79	39.40
AVAN2	1	2	7.89	4.96	49.79	39.11
AVAN2	1	3	7.96	4.94	49.89	39.33
AVAN2	1	4	7.95	4.96	49.79	39.41
AVAN2	1	5	7.95	4.95	49.80	39.31
AVAN2	1	6	7.95	4.96	49.88	39.42
AVAN2	2	1	7.96	4.94	49.95	39.34
AVAN2	2	2	7.96	4.95	49.84	39.38
AVAN2	2	3	7.96	4.94	49.94	39.35
AVAN2	2	4	7.90	4.93	49.85	38.99
AVAN2	2	5	7.96	4.92	49.86	39.15

Table C.1: Geometry of all prepared temperature sensing (1-5) and moisture absorption (6) samples

CNP	Filler Content ($wt\%$)	No.	W (mm)	T (mm)	L (mm)	A (mm^2)
AVAN2	2	6	7.96	4.92	49.90	39.14
Printex L	1	1	7.94	4.95	49.91	39.30
Printex L	1	2	7.95	4.92	49.85	39.13
Printex L	1	3	8.00	4.91	49.92	39.24
Printex L	1	4	7.88	4.98	49.86	38.22
Printex L	1	5	7.95	4.96	49.56	39.42
Printex L	1	6	7.96	4.96	49.74	39.49
Printex L	4	1	8.00	4.95	49.63	39.59
Printex L	4	2	7.96	4.96	49.74	39.44
Printex L	4	3	7.95	4.95	49.82	39.40
Printex L	4	4	7.96	4.95	49.89	38.39
Printex L	4	5	7.96	4.96	49.85	39.44
Printex L	4	6	7.95	4.96	49.86	39.39
Printex L	8	1	7.93	4.97	49.98	39.40
Printex L	8	2	7.96	4.96	49.99	39.51
Printex L	8	3	7.90	4.96	49.72	39.19
Printex L	8	4	7.95	4.91	49.80	39.03
Printex L	8	5	7.96	4.94	49.84	39.33
Printex L	8	6	7.96	4.96	49.93	39.49
Printex L	12	1	7.89	4.95	49.93	39.10
Printex L	12	2	7.95	4.96	49.90	39.39
Printex L	12	3	7.99	4.96	49.98	39.65
Printex L	12	4	7.95	4.95	49.95	38.40
Printex L	12	5	7.95	4.96	49.85	39.41
Printex L	12	6	7.95	4.93	49.95	39.24

C.2 Volume Conductivity

Temperature Sensing with T75

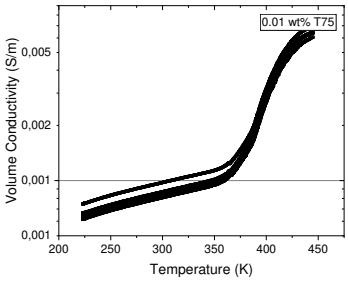

(a) 0.01 wt% T75

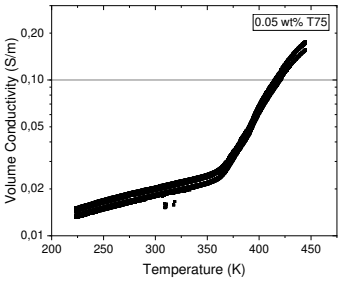

(b) 0.05 wt% T75

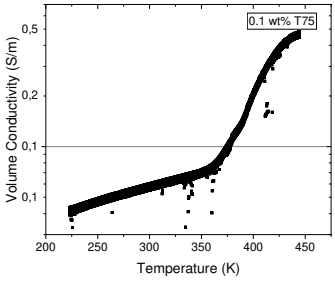

(c) 0.1 wt% T75 (1^{st} cycle)

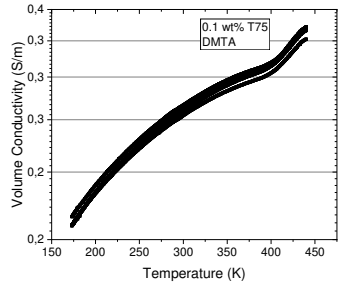

(d) 0.1 wt% T75 (7^{th} cycle)

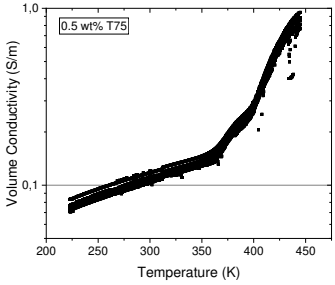

(e) 0.5 wt% T75

Figure C.1: Volume Conductivity of 0.01–0.5 wt% T75

Temperature Sensing with T99

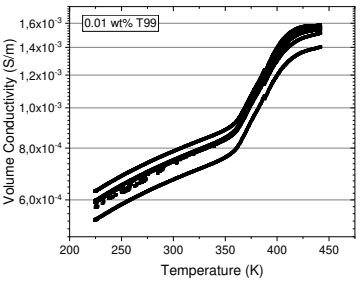

(a) 0.01 wt% T99

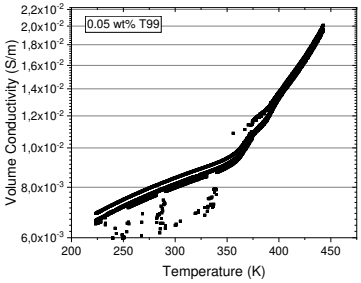

(b) 0.05 wt% T99

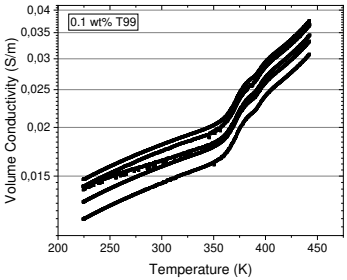

(c) 0.1 wt% T99

Figure C.2: Volume Conductivity of 0.01–0.1 wt% T99

Temperature Sensing with NC7000

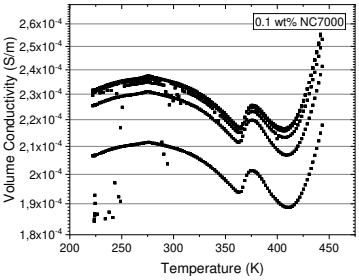

(a) 0.1 wt% NC7000 (1^{st} cycle)

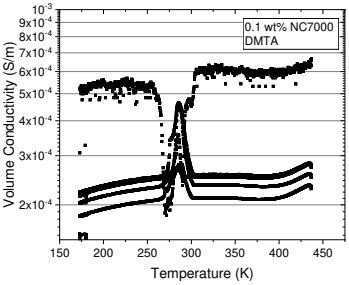

(b) 0.1 wt% NC7000 (4^{th} cycle)

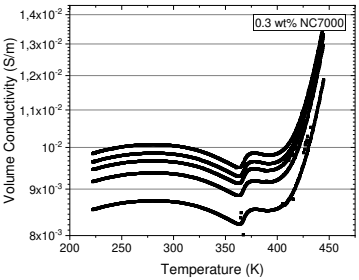

(c) 0.3 wt% NC7000

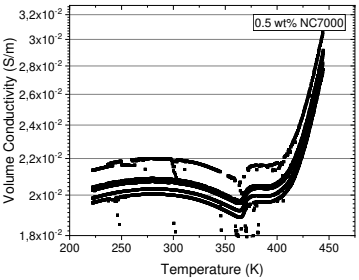

(d) 0.5 wt% NC7000

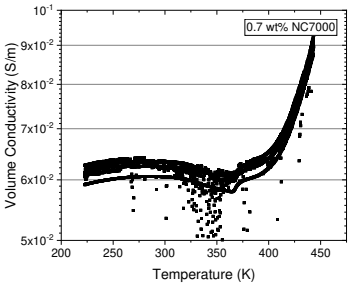

(e) 0.7 wt% NC7000

Figure C.3: Volume Conductivity of 0.1–0.7 wt% NC7000

C.3 Geometry and Heating Rate Influence on DMTA Results

Since 2 mm x 5 mm have mostly been used in experiments of the Institute of Polymers and Composites. Most of the time other sample geometries are already available (e.g. for SENB tests) in larger beam sizes, so manufacturing additional DMTA samples takes extra time. Figure C.4 confirms that the sample size is not influencing the results for elastic modulus up to T_g. Above the glass transition, the modulus decrease occurs faster since a smaller volume has to be heated and the thinner geometry is more prone to bend out when the material softens. The heating rate-dependent behavior shifts the apparent modulus decrease to higher temperature since the material does not have the time to fully reach the applied temperature.

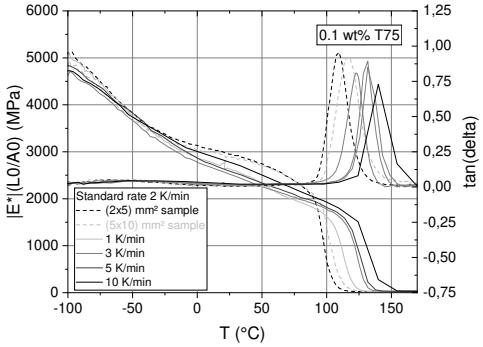

Figure C.4: Representative DMTA curves for 0.1 wt% T75 nanocomposites for variable heating rates

Supervised student theses

T. H. Schepers. Characterization of the influence of functionalized graphene in organic and water-bourne coating systems. Institute of Polymers and Composites (IPC), TUHH and Mankiewicz Gebr. & Co. Master thesis. 2020.

S. M. Selz. Failure behavior characterization of thin-ply CFRP hybrid laminates under cyclic cryogenic temperature conditions. IPC, TUHH. Research project. 2020.

L. Fitzek. Development of a stub-based preparation method for investigation of ceramic samples via nanoindentation and SEM. Institute of Advanced Ceramics, TUHH. Research project. 2020.

L. Braun. Phenomenological characterization of the influence of magnetic fields on CNT epoxy composites. IPC, TUHH. Research project. 2021.

J. Sorejevic. Process parameter optimization of the Creality Ender 5 Plus 3D printer in FDM process on various thermoplastics. IPC, TUHH. Bachelor thesis. 2021.

L. Gillner. DoE Study of Chemical Vapor Deposition Parameters on the Morphology of Vertically Aligned CNTs on Ti-Wafers for Membrane Application. IPC, TUHH. Master thesis. 2022.

J. Wanka. Characterization of CNT composites in directional magnetic fields. IPC, TUHH. Research project. 2022.

L. Christensen. Duroplast- and GFRP-toughening via partially reacted substructures (PRS). IPC, TUHH. Master thesis. 2022.

L. Fitzek. Resorbable polymeric stents for intestine stabilizing during healing. IPC, TUHH. Master Thesis. 2022.

C. Roller. Generation of hydrogen by electrolysis with globugraphite electrodes. IPC, TUHH. Master Thesis. 2023.